DOCTORAL SCHOOL
MEDITERRANEA UNIVERSITY OF REGGIO CALABRIA

DEPARTMENT OF INFORMATION ENGINEERING, INFRASTRUCTURES
AND SUSTAINABLE ENERGY (DIIES)

PHD IN
INFORMATION ENGINEERING

S.S.D. ING-INF/02
XXVIII CYCLE

QUANTITATIVE INVERSE SCATTERING VIA VIRTUAL EXPERIMENTS AND COMPRESSIVE SENSING

CANDIDATE
Martina Teresa BEVACQUA

ADVISOR
Prof. Tommaso ISERNIA

CO-ADVISOR
Dr. Lorenzo CROCCO

COORDINATOR
Prof. Claudio DE CAPUA

REGGIO CALABRIA, FEBRUARY 2016

Finito di stampare nel mese di **Febbraio 2016**

Edizione 

Collana *Quaderni del Dottorato di Ricerca in Ingegneria dell'Informazione*
Curatore *Prof. Claudio De Capua*

ISBN 978-88-99352-03-5

Università degli Studi *Mediterranea* di Reggio Calabria
Salita Melissari, Feo di Vito, Reggio Calabria

MARTINA TERESA BEVACQUA

QUANTITATIVE INVERSE SCATTERING VIA VIRTUAL EXPERIMENTS AND COMPRESSIVE SENSING

The Teaching Staff of the PhD course in
INFORMATION ENGINEERING
consists of:

Claudio DE CAPUA (coordinator)
Raffaele ALBANESE
Giovanni ANGIULLI
Giuseppe ARANITI
Francesco BUCCAFURRI
Giacomo CAPIZZI
Rosario CARBONE
Riccardo CAROTENUTO
Salvatore COCO
Mariantonia COTRONEI
Lorenzo CROCCO
Francesco DELLA CORTE
Lubomir DOBOS
Fabio FILIANOTI
Domenico GATTUSO
Sofia GIUFFRE'
Giovanna IDONE
Antonio IERA
Tommaso ISERNIA
Fabio LA FORESTA
Gianluca LAX
Aime' LAY EKUAKILLE
Giovanni LEONE
Massimiliano MATTEI
Antonella MOLINARO
Andrea MORABITO
Carlo MORABITO
Giuseppe MUSOLINO
Roberta NIPOTI
Fortunato PEZZIMENTI
Nadia POSTORINO
Ivo RENDINA
Francesco RICCIARDELLI
Domenico ROSACI
Giuseppe RUGGERI
Francesco RUSSO
Giuseppe SARNE'
Valerio SCORDAMAGLIA
Domenico URSINO
Mario VERSACI
Antonino VITETTA

Acknowledgments

A significant and valiant scientific research activity is quite a task and it is not possible without suitable support and guidance. Of course, words cannot compensate them and not even fully express my gratitude…

First and foremost, I would like to express my appreciation and thanks to my advisor Prof. Tommaso Isernia, for having showed me the world of Electromagnetism for the first time and especially for having made my PhD experience productive and stimulating. His continual guidance and dedicated involvement in every step throughout my PhD studies and related research activities have allowed me to learn a lot and to grow as a researcher.

Besides my advisor, I would like to thank my co-advisor Dr. Lorenzo Crocco for his insightful comments and hard questions which encouraged me to widen my research and to look at it from various perspectives. The possibility of interacting with him has represented an invaluable opportunity for improving my scientific knowledge.

I would like to express my gratitude to Dr. Andrea Morabito for the example he has provided me as a tireless and flawless researcher, and for his professional and non-professional advices.

Moreover, I am thankful to Dr.. Loreto Di Donato. My research activity has profited greatly from his expertise and the useful collaboration with him, starting from the beginning when he supported me as co-advisor of my Bachelor thesis.

Last, but not least, my sincere thanks also go to Drs. Rosa Scapaticci, Roberta Palmeri and Antonella Laganà for their invaluable collaboration and their company during this experience.

Contents

List of Figures

List of Tables

List of Acronyms

BA	Born Approximation
BIM	Born Iterative Method
CS	Compressive Sensing
CSI	Contrast Source Inversion
DARE	Direct Algebraic Reconstruction
DBA	Distorted Born Approximation
DBIM	Distorted Born Iterative Method
DIVE	Distorted Iterative Virtual Experiment
DOF	Degree of Freedom
EPT	Electric Properties Tomography
FFE	Far Field Equation
FM	Factorization Method
GPR	Ground Penetrating Radar
LSM	Linear Sampling Method
MNP	Magnetic Nanoparticle
MR	Multiplicative Regularization
MRI	Magnetic Resonance Imaging
MWI	Microwave Imaging
PMF	Polarizing Magnetic Field
RCSI	Regularized Contrast Source Inversion
RIP	Restricted Isometry Property
ROI	Region Of Interest
SNR	Signal to Noise Ratio
SOM	Subspace Optimization Method
SVD	Singular Value Decomposition
TSVD	Truncated Singular Value Decomposition
TV	Total Variation
VE	Virtual Experiment

Introduction

I.1 Inverse scattering problems and their relevance

An electromagnetic field which is propagating in the space in presence of obstacles goes through some perturbations depending on their nature and features. This phenomenon, which is named electromagnetic scattering [*Colton and Kress*, 1998, *Hopcraft and Smith*, 1992], implies the presence in the space of a new electromagnetic field, known as total field, given by the linear superposition of the original one, which is called incident or unperturbed field, and the perturbation field, which is referred to as scattered field. The scattered field is physically generated by the targets that interact with the incident field during its propagation. In fact, the incident field induces inside the obstacles some currents which become sources of the scattered field.

Electromagnetic scattering implies two different classes of problems: forward scattering and inverse scattering. The forward scattering problem aims at determining the scattered field when the features of the targets which have generated it and the incident field are known. On the contrary, the inverse scattering problem consists in the quantitative reconstruction of the targets' features starting from the knowledge of the incident field and the measurements of the scattered field [*Colton and Kress*, 1998, *Hopcraft and Smith*, 1992].

From a physical point of view, the difference between direct and inverse problem is linked to the concept of cause and effect. In the direct problem, starting from the knowledge of the causes (the interaction between the incident field and the objects) the aim is the computation of the scattered field, while the inverse scattering problem amounts at determining the feature of the targets which generate the perturbation of the original field, provided that the effect of the interaction (the scattered field) is known. These

problems are related by a sort of duality, that is if the role of data and unknowns is exchanged one problem is obtained from the other one [*Bertero and Boccacci*, 1998].

Although strictly coupled, the mathematical nature of the two problems is deeply different. In fact, the forward inverse scattering problem is linear and well posed, that is, according the Hadamard's definition [*Bertero*, 1989], its solution always exists, is unique and depends continuously on the data, which are represented by the knowledge of the incident fields and the features of the obstacles. This is not true for the inverse scattering problem which is both non-linear and ill-posed with respect to the nature of the obstacles [*Colton and Kress*, 1998, *Hopcraft and Smith*, 1992, *Bertero and Boccacci*, 1998]. Because of the difficulty in tackling the ill-posedness and non-linearity of the problem, significant efforts have to be pursued in the mathematical, applied physics and engineering communities to develop reliable, effective and accurate methods and strategies to solve this inverse problem. However, such a challenging task is still an open issue.

Obviously, the availability of processing techniques able to avoid the difficulties due to non-linearity, as well as to give an accurate quantitative rendering of the actual electromagnetic scenario, is essential in a number of applications. Surely, the capability of microwaves of investigating non-accessible scenarios in a non-invasive and non-destructive way has contributed to increase the strong interest in applications [*Pastorino*, 2004], such as subsurface prospections [*Daniels*, 2004, *Persico*, 2014], biomedical diagnostics [*Hassan and El-Shenawee*, 2011, *Semenov and Corfield*, 2008, *Semenov et al.*, 2007], safety and security surveying operations [*Pierri et al.*, 2013, *Jin and Yarovoy*, 2015, *Millot and Casadebaig*, 2015], and non-destructing testing of materials [*Zoughi*, 2000], only to mention some examples.

Probably, one of the most important applications of microwave is in medical imaging, wherein this technology could improve health care in terms of prevention screening programs and monitoring applications.

In fact, in the last years the evidence that human tissues exhibit different electromagnetic properties at microwaves, depending on their typology and physio-pathological status, has given rise to a huge interest in

Microwave Imaging (MWI) for medical applications, by exploring in particular the possibility of retrieving morpho-functional images of the inspected anatomical structure. The use of non-ionizing radiations and possibly cheap and portable devices represents the main advantage offered by MWI with respect to other medical imaging techniques.

In particular, MWI has gained increasing interest in breast cancer diagnostics [*Fear et al.*, 2002, *Hassan and El-Shenawee*, 2011], as it represents the first cause of death for cancer in women and its early diagnosis has a huge impact in the fight against cancer. Moreover, currently adopted diagnostic techniques in breast cancer diagnostic still suffer from some limitations and researchers are pushed to investigate to alternative techniques. For instance, the widely adopted X-ray mammography, besides being ionizing, still could give a larger rate of false negatives and false positives, so in many cases a breast biopsy is needed to verify the tumor diagnosis.

In addition, several research groups are investigating the possibility to use microwave techniques in other fields of medical imaging, such as possible diagnostic tools for brain stroke and ischemic disease [*Scapaticci et al.*, 2012a, *Semenov and Corfield*, 2008]. This is due to the fact that ischemic tissues show in the microwave band different electric properties with respect to healthy tissues and that microwaves are particularly suitable to perform a continuous monitoring, since they are not harmful for the patient, being non- ionizing. Other possible applications are bone mineralization monitoring [*Meaney et al.*, 2012, *Zhou et al.*, 2010] and soft tissues imaging [*Semenov et al.*, 2007].

Another important class of applications is use of microwave in subsurface inspection [*Daniels*, 2004, *Crocco and Soldovieri*, 2011, *Persico*, 2014, *Soldovieri and Crocco*, 2011]. A very wide range of possibilities exists, the most common being the safe and accurate location of the position of buried object (like pipes, utilities or potential hazards such as mine shafts and voids), the investigation of the reinforcement and condition of roads, bridges, and airport runways, the identification of structural integrity of buildings, the study of the environmental and geological conditions, or archaeological sites.

Demining is another important application [*Daniels*, 2006, *Persico*, 2014]. In particular, modern mines are customarily built with plastic materials with

only little or even no metallic parts. Therefore, they are often hardly visible or completely invisible to a metal detector. In this context it is fundamental for the effectiveness of the survey and the safety of the people involved in it to provide all the details possibly available, that is the position and the depth, the size, the shape and the electromagnetic properties of the buried target, in such a way to avoid the occurrence of false negative (or false positive). In this respect, microwave tomographic approaches offer different tools which are able to produce reliable and easily interpretable images of the investigated scenarios. Notably, such a kind of outcomes is much more user friendly than the ones achieved by using standard GPR data processing.

Finally, the inverse scattering problems solution are also of interest in the design of filters, radiation elements and microwave devices [*Bucci et al.*, 2005, *Roberts*, 1995, *Song and Shin*, 1985, *Hakansson*, 2007, *Di Donato et al.*, 2014a], as some synthesis problems can be formulated in terms of retrieval problems. For example in [*Di Donato et al.*, 2014a], an effective synthesis of cloaking profiles is performed via inverse scattering techniques.

I.2 Basic equations and approaches

The two fundamental equations describing the relevant scattering problem for a generic incident field $\boldsymbol{E_i}$ are the data equation and the state equation. The first one is an integral representation of the scattered field in the region exterior to the investigation domain, while the state equation is the integral representation of the total field inside the investigation domain. The mathematical expressions of these latter, in case of nonmagnetic media, are, respectively:

$$\boldsymbol{E_s} = \mathcal{A}_e[\chi \boldsymbol{E}] \tag{I.1}$$

$$\boldsymbol{E} = \boldsymbol{E_i} + \mathcal{A}_i[\chi \boldsymbol{E}] \tag{I.2}$$

where $\boldsymbol{E_s}$ and $\boldsymbol{E}$ are the scattered field outside the investigation domain and total field induced in the investigation domain, respectively, and χ is the contrast function which relates the electromagnetic features of the object and the ones of the host medium. $\mathcal{A}_e$ and $\mathcal{A}_i$ are a short notation for the bilinear integral radiation operators relating the quantity $\chi\boldsymbol{E}$ to the scattered field $\boldsymbol{E_s}$ outside and inside the investigation domain, respectively. Note in the above equations the time harmonic factor $exp\{j\omega t\}$ is assumed and dropped.

The inverse scattering problem aims at retrieving the unknown contrast χ from the scattered fields $\boldsymbol{E_s}$ measured on a generic curve of observation. As stressed in the introduction, such a problem is non-linear respect to χ and ill-posed. The former circumstance descends from the dependence of the total field $\boldsymbol{E}$ on the unknown contrast function χ expressed by the state equation, while the latter from the compactness of the radiation operator $\mathcal{A}_e$ [*Bertero and Boccacci*, 1998], as described in the following section.

According to the above considerations, if $S(\chi, \boldsymbol{E_i})$ denote the nonlinear scattering operator relating the contrast and the arbitrary incident field to the corresponding scattered field, the inverse scattering problem is generally solved by seeking the global minimum of:

$$\Phi(\chi) = \|\boldsymbol{E_s} - S(\chi, \boldsymbol{E_i})\|^2 \tag{I.3}$$

which defines the discrepancy between the measured data and the predicted scattered field, corresponding to χ and $\boldsymbol{E_i}$ [*Roger*, 1981, *Joachimowicz et al.,* 1998]. An alternative approach involves the simultaneous solution of the system of equations (I.1)-(I.2) for both the contrast function and the electric field inside the object. Obviously, the set of unknowns enlarges but the degree of non linearity [*Bucci et al.*, 2001a] reduces to that of a fourth order polynomial. In this case the problem is generally solved by seeking the global minimum of:

$$\Phi(\chi, \boldsymbol{E}) = \|\boldsymbol{E_s} - \mathcal{A}_e[\chi\boldsymbol{E}]\|^2 + \|\boldsymbol{E}(\boldsymbol{r}) - \boldsymbol{E_i}(\boldsymbol{r}) + \mathcal{A}_i[\chi\boldsymbol{E}]\|^2 \tag{I.4}$$

Finally, it is also possible to consider the currents induced inside the object as auxiliary unknowns instead of the total field $\boldsymbol{E}$. To this end, the mathematical formulation of the problem is modified by defining the contrast sources $\boldsymbol{W} = \chi \boldsymbol{E}$. Opposite to field-type approaches, in this case the inverse scattering problem is turned into an inverse source problem and one of the two fundamental equations of the electromagnetic scattering, i.e. the eq. (I.1), become linear [*van den Berg and Kleinman*, 1997, *D'Urso et al.*, 2010, *Isernia et al.*, 2004].

I.3 Two challenging difficulties: ill-posedness and non-linearity

Besides its applicative relevance, the inverse scattering problems are also challenging from a theoretical point of view. Indeed, as pointed out in the previous Sections, the inverse scattering problem is ill-posed and also non-linear in the relationship between the data and unknowns.

A. Implication of ill-posedness

A problem is said well-posed according to the Hadamard's definition [*Bertero*, 1989] if its solution always exists, it is unique, and it depends continuously on the data. If one of these three requirements is not satisfied, that is the solution might not exist at all, or it might not be unique or might not depend continuously on the data, then the problem is said to be ill-posed. This latter requirement is related to the 'physical meaning' of the solution. As a matter of fact, the key idea of Hadamard was to assume that an estimate of the unknown of the problem which considerably changes following a small variation of data is not a reliable solution. This has an immediate practical consequence, as variations on the data may occur (actually, occur) due to the unavoidable presence of measurement errors.

In inverse scattering problems the solution always exists, and theoretical uniqueness is proved in both tridimensional and bidimensional cases [*Colton*

and Paivarinta, 1992, *Nachman*, 1993]. The crucial point is represented by the continuity requirement, as described in the following.

In case of single-view (a single illuminating incident wave is used), the scattering operator which relates unknown target's properties to scattered fields is compact, i.e. it transforms any bounded set in a pre-compact one [*Kolmogorov and Fomine*, 1973, *Bertero and Boccacci*, 1998]. As the inverse of a compact operator cannot be continuous, the single view inverse scattering problem is ill-posed and small variations of the scattered field data produce unbounded variations of the corresponding 'solutions'. The data are always affected by noise, which is then amplified in the inversion process, thus rendering completely meaningless the retrieved solution. This happens also in the discrete version of the inverse scattering problem, which is referred to as *ill-conditioned* problem.

To get a better insight into the ill-posedness, it is worth recalling that another basic property of pre-compact sets is that they admit a finite-dimensional representation within any required accuracy [*Kolmogorov and Fomine*, 1973, *Bucci and Isernia*, 1997]. Any scattered field can be accurately represented with a finite number of parameters and such a number can be identified as the number of Degree Of Freedom (DOF) of the field [*Bucci and Franceschetti*, 1989]. It follows that only a finite number of independent measurements of the scattered field is available and hence only a limited number of independent parameters can be recovered from scattered field data. In fact, it is not possible to retrieve a generic function belonging to an infinite dimensional space from a finite number of parameters belonging to a finite dimensional space.

Unfortunately, also in case of multi-view cases (more illuminating incident waves are used) the problem remains ill-posed. The incident fields also belong to a compact set as non superdirective source are assumed, and, by considering the same arguments used in the single-view, the scattering operator is also compact in the multi-view case. Hence, there is no hope of extending at will the number of independent equations considering different incident fields. Only a finite number of scattering experiments can be in fact considered.

As a consequence, the problem cannot be solved in any ordinary sense, but a generalized solution has been defined in order to restore well-posedness.

B. Implication of non-linearity

As shown in Section I.2, a generalized solution of inverse scattering is usually looked for by minimizing a suitable cost functional, which takes into account the physical model and also the relationship between the measured field data and the corresponding unknown contrast function.

Due to the non-linearity of the underlying problem, this cost functional is a non-quadratic one, so that it may have many local minima which are 'false solutions' of the problem [*Isernia et al.*, 2001]. The more the problem departs from a linear one the more the occurrence of false solutions.

As a consequence, the obtained results depend on the considered initial guess. In fact, if the initial guess does not belong to the attraction region of the actual solution, the minimization scheme, if not adequately constrained, could be trapped in local minima, which could be completely different from the actual ground truth.

Moreover, the cost functional usually depends on a very large number of unknowns, especially in tridimensional geometries.

Besides the global optimization, which is often not viable in realistic case due to the elevate number of unknowns, several strategies do exist to tackle and defeat the occurrence of the false solutions and, so, to counteract the non-linearity. In the following Section, the main ones are briefly discussed.

I.4 Solution strategies

Due to the difficulty in tackling the non-linearity and ill-posedness of the inverse problem different efforts have been carried out in the literature.

A common feature for any inversion approach is the requirement to be fast, to have a low computational burden and to provide reliable

reconstructions with as minor as possible priori information on the physical or geometrical properties of the unknown scenario.

I.4.1 Regularization techniques

In order to restore well-posedness, the solution of the problem must fit the data within the experimental error but also expresses some expected physical properties of the unknown. The most simple form of enforce a priori information is to include a regularizing term in the cost functional.

The principle of the regularization methods is indeed to use the additional a priori information on the contrast function in an explicit way to construct from the beginning a solution both compatible with the data and which exhibit some specific physical features. The kind of additional information which can be exploited and/or enforced includes (but it is not limited to):

i. an upper bound on the dimensionality of the space where the unknown function is looked for. In order to avoid ill-posedness problem, a necessary (still not sufficient) condition is that its dimension is not greater than the one of the data space. Such a strategy can be defined 'regularization by projection' [*Bucci et al.*, 2001b, *Isernia et al.*, 1997, *Isernia et al.*, 2004, *Catapano et al.*, 2009a, *Scapaticci et al.*, 2012b, *Scapaticci et al.*, 2015, *Li et al.*, 2013, *Lencrerot et al.*, 2009];
ii. a requirement on the energy of the solution such as for instance a minimum ℓ_2 energy requirement. This is the case of the well known Tikhonov regularization technique [*Tikhonov et al.*, 1995, *Bertero and Boccacci*, 1998];
iii. enforcing a piecewise constant behavior on the contrast function [*Oliveri et al.*, 2014, *van den Berg and Kleinman,* 1995, *van den Berg et al.*, 2003, *Crocco and Isernia*, 2001];
iv. physics induced bounds on the values of the unknown permittivity and conductivity functions (f.i., positive conductivities);

v. the knowledge that the punctual value of the unknown function only can belong to a given finite alphabet of values [*Catapano et al.*, 2004].

Strictly speaking, when dealing with the non-discretized problem, only (i), (ii) and (v) allow to hopefully restore well-posedness, as constraints (iii) and (iv) do not avoid to deal with infinite dimensional spaces for the unknown.

When the additional information is of statistical nature the regularized method are *Bayesian*.

In order to restore the well-posedness of the problem, another interesting opportunity is offered by the Compressive Sensing theory [*Donoho*, 2006, *Baraniuk*, 2007] (for more detail see Appendix E and Chapter 3), a new paradigm in signal recovery which is based on the concept of 'sparsity' or 'compressibility' of the unknown function, i.e the possibility to represent this latter in an exact or anyway accurate fashion through a limited number of nonzero coefficients of a convenient basis.

All the above discussed regularizations act only on the actual unknown that is the contrast function χ. When exploiting 'contrast oriented' regularization schemes, one is implicitly enforcing some property of the unknown function, and the effectiveness of the different regularizations will depend on how much the unknown scenario 'fits' the regularization model.

I.4.2 Traditional methods to overcome non linearity

As a countermeasure to non-linearity, *linearized* methods seem to allow a very easy implementation and require a limited amount of computer memory and computational time, even though they suffer from several limitations induced by the adopted *approximated model*.

In fact, considering for instance the Born Approximation (BA) [*Devaney*, 1984], the unknown total field inside the object is assumed equal to the incident field. This hypothesis is fully satisfied only in absence of the object itself so that the BA is acceptable in case of weak scatterers, i.e., for objects whose internal characteristics are very close to the ones of the external

medium, and/or for objects whose dimension is very small in terms of the wavelength in the external medium, so that the scattered field due to their presence is negligible with respect to the incident field. Note, if the linearization is performed around a nominal scenario different from a homogeneous background, the underlying approximation is referred to as Distorted Born approximation (DBA) [*Devaney and Oristaglio*, 1983].

Other examples of *linearized* methods are the physical optics approximation (Kirchhoff approximation), where waves are scattered from electrically large conductors, and the Rytov approximation, where the length scale of fluctuations is large as compared to the wavelength [*Devaney*, 1981].

These methods are *quantitative*, i.e. give the full characterization of the targets, as long as the adopted approximated model holds true. As a consequence, because of their limitations, they are typically not capable of providing an accurate description of the targets' features when exploited outside of the range of validity of the underlying approximations and could give completely meaningfulness results.

As improvement with respect to the *linearized* method, the quadratic method [*Brancaccio et al.*, 1995, *Pierri et al.*, 2002] is also worth being mentioned. In this latter, a weak degree of non-linearity is introduced by adopting a second order approximation for the unknown-data mapping operator. In particular, the method is named quadratic as the unknown appears as a power of the second order. With respect to the linear methods as for instance BA, it allows to reconstruct a class of unknown profiles wider, but in any case it has a limited practical interest.

A possible extension of BA to the case of non-weak scatterer can be represented by the Born iterative method (BIM) [*Wang and Chew,* 1989] and the distorted Born iterative method (DBIM) [*Chew and Wang*, 1990]. This latter aims at solving the two coupled scattering integral equations by solving a sequence of linear problems and by updating the internal fields (also the Green function in DBIM) at each iteration through the solution of a forward scattering problem. Obviously, the final outcome and performances depend on the starting guess and the range of validity of the intermediate

linearizations, so the convergence to actual ground truth cannot be always ensured.

In order to overcome the above limits, iterative optimization procedures, which tackle the inverse scattering problem in its full non linearity and do not involve any approximations, are often proposed to determine both the morphology and the electromagnetic contrast of the targets. The main practical difficulty with the iterative optimization algorithms is the long (or extremely long) reconstruction times required in order to complete the minimization. Global optimizations, as genetic or particle swarm algorithms [*Haupt*, 1995, *Pastorino et al.*, 2000, *Donelli et al.*, 2006], are generally not viable in case of large number of unknowns (typical in realistic problems like medical imaging) due to the exponential growth of the computational complexity.

For this reason, *local* iterative optimization schemes are usually adopted. Examples of these are the modified gradient method [*Kleinman and van den Berg,* 1993, *Souriau et al.*, 1996, *Isernia et al.*, 1997, *D'Urso et al.*, 2010], the Contrast Source Inversion (CSI) method [*van den Berg and Kleinman*., 1997], the Contrast Source Extended Born model [*Isernia et al.*, 2004] and the Subspace Optimization Method (SOM) [*Chen*, 2010]. However, being the cost functional related to the underlying problem non-linear, local minimization is prone to the occurrence of false solutions [*Isernia et al.*, 2001].

Increasing as much as possible the essential dimension of data and reducing as much as possible the number of unknowns, positively affects the false solution problem. In fact each additional independent contribution will have a minimum in the actual solution, while its other minima will be widespread. The additional equations will fit the local minima as long as they are independent from the previous ones. For instance further data can be gained by multi-view scattering experiments, with the only drawback that the complexity of the image device increases. Unfortunately, at a given frequency only a finite amount of independent experiments can be performed (see Section I.3.A). An alternative possibility is offered by the frequency diversity, although it needs to model dispersive behavior of the involved media [*Bucci et al.*, 2000].

Moreover, if appropriate a *priori* information is available, optimization methods can be equipped with a good starting guess, regularization schemes or constraints (see for instance the subsection I.4.1) in order to extend their applicability and reliability.

Additionally, in order to gain preliminary understanding of shape and/or of other characteristics of the unknown objects and overcome the limitations of optimization schemes and even linearized method [*Catapano et al.,* 2007a, *Brignone et al.*, 2007], smart *pre-processing* techniques can be exploited [*Cakoni and Colton*, 2006, *Colton et al.*, 2003, *Kirsch*, 1998, *Zhong and Chen*, 2007, *Catapano et al.*, 2007b, *Zhang et al.*, 2012a, *Crocco et al.*, 2013].

Two relevant examples are the Linear Sampling Method (LSM) [*Colton et al.*, 2003, *Catapano et al.*, 2007b] and the Factorization Method (FM) [*Kirsch*, 1999], which pursue the reconstruction of the morphological features of the scatterers by solving an auxiliary linear inverse problem with a negligible computational burden. For instance in [*Catapano et al.* 2007a] the target's support estimation, obtained via LSM, is used for quantitative inversion carried out via non-linear optimization, thus improving the reliability of the inversion process and reducing its computational burden.

Finally, an interesting alternative to deal with the occurrence of the false solutions can be represented by step wise refinement techniques. Some examples include:

- frequency hopping techniques [*Haddadin and Ebbini*, 1998], in which, one starts with a low resolution reconstruction, by processing just the lower frequency data, and then uses it as a starting guess for higher frequency reconstruction. This technique plays a very important role, as low frequencies make it possible to locate the objects and to reconstruct them roughly, and then higher frequencies allow finer details to be retrieved;
- multiscale/multiresolution techniques [*Baussard*, 2005, *Scapaticci et al.*, 2012b, *Chiappinelli et al.,* 1999, *Scapaticci et al.*, 2015], in which one starts with a coarse representation of the unknown and then improve reconstruction by focusing attention on details (in this respect Wavelets transform seem be a convenient framework);

- the splitting of the problem into simpler auxiliary ones, each one devoted to determine some partial information about the scatterer (such as position of the center of the scatterer, presence of losses, possible symmetries, mean value and shape of its permittivity distribution), before the final quantitative inversion.

I.4.3 Some recent developments

As discussed in the previous subsection, a *priori* information on the unknown and *pre-processing* techniques are traditionally exploited in order to limit the occurrence of false solution. In fact, each preliminary knowledge on the unknown contrast can be used to get a good starting point for iterative inversion schemes in order to fall into the right attraction basin, or to restrict of the dimensionality of the unknown space, or choose the suitable representation basis in order to increase the data-unknown ratio (f.i. projection methods based on Fourier harmonics or Wavelets transform), or even to enforce other constraints.

On the other hand, priori information on the unknown or suitable pre-processing step could open the way to a new way of thinking about the solution of inverse scattering problems. In fact, rather than enforcing during the inversion procedure some properties, known a priori or acquired by means of a pre-processing of the data, one can take into account them from the beginning by rewriting the pertinent scattering equations [*Isernia et al.*, 2004, *Ma et al.*, 2000, *Crocco et al.*, 2012a].

For instance in [*Isernia et al.*, 2004] by taking advantage of the a priori information on the features of the Green's function, a convenient rewriting of the integral equations (I.1) and (I.2) has been exploited to introduce a new model for bidimensional electromagnetic scattering by dielectric objects in lossy media. By exploiting this latter, a new series expansion has been introduced in order to accurately and effectively solve the forward and inverse problem. This main advantage offered by this new scattering model is the lower degree of nonlinearity with respect to parameters embedding dielectric characteristics if compared to the traditional model.

A suitable rewriting of the scattering equation and a new field approximation, which rely on a proper (physics inspired) exploitation of the solution of the LSM, have been recently proposed in [*Crocco et al.*, 2012a]. The proposed field approximation takes into account the nature of the unknown scenario through the pre-processing step and allows to exploit a linear model for quantitative reconstruction. In particular, in [*Di Donato et al.,* 2015a] the range of applicability of this original inversion procedure is investigated showing that it significantly outperforms the usual BA, as it is target dependent and considers the contribution of the field scattered by the object. A generalized version of this linear inversion method has been recently introduced in [*Di Donato et al.,* 2016] in order to appraise the properties of non-weak anomalies with respect to a partially known and non-homogeneous scenario, going beyond the range of validity of the DBA.

Other recent development in the solution of inverse scattering interests a new kind of regularization, which interest the auxiliary unknown, furtherly considered in addition to the actual one, rather than the contrast function (see subsection 1.4.1). Notably, enforcing some property on the auxiliary unknown would allow to reduce the nonlinearity of the inverse scattering problem, with obvious beneficial effects with respect to the possible occurrence of false solutions.

Note the only method up to now acting on the contrast sources to regularize the problem is the subspace optimization method (SOM) [*Chen*, 2010]. The essence of the method is that part of the contrast source is determined from the spectrum analysis without using any optimization, whereas the rest is determined by optimization method.

The intrinsically different nature of these regularizations, with respect to other ones acting on the contrast, naturally suggests that these approaches could be exploited together, leading to further improved performances, as done in [*Xu et al.*, 2015].

I.5 Aim and outline of the thesis

Solutions of inverse scattering problems can be completely erroneous if non-linearity and ill-posedness are not properly tackled. The availability of processing techniques, able to avoid the possible occurrence of false solutions as well as able to give an accurate quantitative rendering of the actual electromagnetic scenario, is essential in several applications (such as demining and biomedical imaging), as discussed in the Section I.1.

In this respect, the aim of the thesis is concerned with the development of innovative and reliable solution procedure for quantitative inverse scattering problem, which have a range of applicability as wide as possible while keep low both the complexity of the solution method and the computational burden.

In this thesis the 2D problem is analyzed and discussed, as its full understanding is still an open issue and is pivotal towards the more demanding 3D case. In fact, both the optimization of the corresponding inversion approaches and the possibility of using interesting high performance hardware resources and effective solution strategies allow to foresee a simple extension at the case of 3D geometry. As a demonstration of the actual viability in 3D problems, in Chapter 5, a tridimensional geometry is also considered.

With the aim of developing new solution strategies and tools, the general idea of the thesis is the well-conditioning of the inverse scattering problem by acting from one hand on the actual variable, that is the contrast function, and from the other hand on the auxiliary unknown, that is the total field or the contrast sources induced inside the target.

In order to act on the auxiliary unknown and contemporary reduce the non-linearity, in the first part of the thesis the new paradigm of **Virtual Scattering Experiments** (VE) is introduced. VE are a new kind of experiments, which are obtained starting from the statement that scattering phenomena can be recombined in many different ways, due to the linearity of Maxwell equations with respect to the primary sources. Their peculiarity is that they can be designed in such a way to condition the scattering

phenomena and enforce some peculiar properties on the internal fields or on the corresponding currents. Note that this kind of information does not descend from some priori assumptions on the scattering model or on the contrast function. Rather, it follows from some smart pre-processing of the available data. In particular, in this thesis, such information is conveniently used in order to develop three new inversion approaches (see Chapter 2 and [*Bevacqua et al.*, 2014a, *Bevacqua et al.*, 2015a-d]).

On the contrary, in order to act on the actual unknown, the emerging and powerful tool in signal/image processing of the **Compressive Sensing** is exploited. The CS allows to improve the accuracy of existing inversion procedures, obtaining a kind of 'super- resolution', and/or driving the design of simpler and cheaper measurement set-ups. Obviously, it can be definitely attractive in the solution of inverse scattering problems. Unfortunately, this theory is well developed only for the case of phenomena described through linear models. This represents a fundamental difficulty for its application in the problem at hand. In this respect, three different approaches are developed, in which a possible linearization is considered and discussed and two possible approaches considering the problem in its full non linearity are also explored [*Di Donato et al.*, 2014b, *Bevacqua et al.*, 2015e]

The thesis consists of 5 chapters and 5 appendices (where mathematical details are deepened) and it is organized in two different parts. In the first part of the thesis (Chapters 1-3) both theoretical and numerical results reached by developing innovative solution strategies for quantitative inverse scattering are illustrated and discussed. In the second part of the thesis (Chapters 4-5) the outcomes reached in the previous Chapters are originally exploited in order to improve the imaging results by considering two different applications: biomedical diagnostics, in particular for the breast cancer, and subsurface prospections. [*Bevacqua and Scapaticci*, 2015, *Bevacqua et al.*, 2015f].

In particular, in Chapter 1, the mathematical notations and the general adopted measurement setup for 2D scalar problems are first illustrated. Then, the new paradigm of VE for the solution of inverse scattering problem is introduced and the possibility of conditioning the scattering phenomenon by means of proper designed VE is presented. To this end, the LSM is proposed

as design tool [*Crocco et al.*, 2011, *Di Donato et al.*, 2011], by taking advantage of its physical interpretation in terms of electromagnetic focusing problem. Finally, in light of the above field conditioning concept and the VE framework, two inversion methods recently introduced in literature are briefly recalled and reinterpreted. These strategies aim at counteracting the non-linearity of inverse scattering problem [*Crocco et al.*, 2012a], and overcoming the relevant information lack arising when data are gathered under aspect limited measurements configuration [*Di Donato and Crocco,* 2015].

Chapter 2 introduces, describes and discusses three different solution strategies based on suitably designed VE. In particular, in the first two of them VE are built in such a way to induce a circularly symmetric behavior of the scattered fields and contrast sources. Then, limitations associated to the linearization used in [*Crocco et al.*, 2012a] are overcome according to two different approaches.

In the first one, named Direct Algebraic Reconstruction (DARE) a new and original approximation of the contrast source induced inside the targets is introduced [*Bevacqua et al.*, 2015g]. These latter allows to reduce the solution of the inverse problem to a diagonal system of third degree algebraic equations. This method provides a very fast solution of the inverse scattering problem by means of closed form formulas. The method is introduced and discussed in Section 2.1, while some details are deferred to Appendices A, B and C.

In Section 2.2, by using the same kind of VE, a Regularized Contrast Source Inversion (RCSI) scheme is introduced [*Di Donato et al.*, 2015b], in which no approximation of the scattering model is considered. Rather, a simple regularization term acting on the induced currents rather than the contrast function is added in the standard CSI scheme. Some details about CSI scheme are reported in Appendix D.

In the same spirit of overcoming limitations due to linearizations or approximations, as well as to deal with scatterers located in a possibly non homogeneous background, in Section 2.3 a Distorted Iterated Virtual Experiments (DIVE) inversion method is discussed [*Bevacqua et al.*, 2016a]. In the same line with DBIM (but using VE), it is based on a series of

intermediate linearizations, in which the Green's function, the VE and corresponding approximations [*Crocco et al.*, 2012a] are updated on the basis of intermediate results.

While Chapter 2 is focused on VE as a way to have a conditioning of the auxiliary unknown E or W, Chapter 3 is concerned with the exploitation of possible regularizations on the contrast function. In particular, it introduces and describes new inversion methods inspired to CS theory, in which different possible kinds of sparsity of the contrast function, as well as different possible ways of exploiting them, are considered.

In particular, in Section 3.2 and 3.4 the CS theory is used in conjunction with VE based approaches [*Bevacqua et al.*, 2015h, *Bevacqua and Di Donato*, 2015], that are the linear approximation recalled in Section 1.6.1, and the DIVE method introduced in Section 2.3. As such, these two methods act contemporary on actual unknown, which is supposed to be sparse, and on the auxiliary one, which is conditioned by means of well-designed VE.

Later in Section 3.3, a first attempt of imposing sparsity regularization in non-linear framework is discussed [*Bevacqua et al.*, 2014b]. In particular, two innovative sparsity promoting methods are introduced and developed, which tackle the inverse scattering problem in its full non-linearity by adopting again a CSI scheme.

As a byproduct, an original geometrical interpretation of CS 'for dummies' is also furnished in Appendix E.

Both in Chapter 2 and 3, numerical results against simulated and experimental data are given in order to assess the validity of the proposed inversion methods.

As a proof of the actual viability of the introduced techniques in real applications, the second part of the thesis concerns with use of microwaves for the breast cancer imaging enhanced by the use of Magnetic Nanoparticles (MNP) and for the imaging of objects buried in the subsoil.

More in details, MNP enhanced MWI represents an innovative technique for breast cancer diagnosis, in which MNP have been proposed as contrast agent, in order to overcome some limitations of conventional microwave imaging techniques, thus providing reliable and specific diagnosis

of breast cancer. In particular in Chapter 4 an *ad hoc* CS inspired inversion technique is introduced for the reconstruction of the magnetic contrast induced within the tumor [*Bevacqua and Scapaticci*, 2016].

On the other hand, the Subsurface MWI represents an assessed means to process GPR and valid alternative to the standard GPR data processing. In particular in Chapter 5, an efficient inverse scattering strategy based on framework of the VE and Compressive Sensing is proposed to achieve dielectric characterization of non-weak and extended hidden targets and buried objects in lossy soil [*Bevacqua et al.*, 2016b].

Conclusions and recommendation for further developments are finally given.

Part I

NEW PARADIGM AND TOOLS FOR NON LINEAR INVERSE SCATTERING PROBLEMS

1
Conditioning scattering phenomena by Virtual Experiments

1.1 Mathematical notations and measurement configuration

In the following the mathematical formulation of inverse scattering problems is introduced in more details with respect to the canonical 2D scalar case, by considering TM polarized fields, and assuming and dropping the time harmonic factor $exp\{j\omega t\}$.

The adopted measurements configuration is the so-called multiview-multistatic one, in which the antennas are organized in such a way that for each transmitting antenna all the antennas (including the transmitting one) act as receivers, and all antennas alternately act as a transmitter. By the sake of simplicity, let us consider the case where antennas are located in the far-field with respect to the investigation domain $\Omega \subseteq \mathcal{R}^2$ and on a circumference Γ distant *R* from the origin of the reference system xOy, which is centered respect to Ω, see fig. 1.1.

Let us consider an unknown nonmagnetic object with compact, possibly not connected support Σ and denote with ε_s and σ_s its relative permittivity and the electric conductivity, respectively. The target is embedded in a nonmagnetic medium of permittivity ε_b and conductivity σ_b. The magnetic permeability is everywhere equal to that of free space μ_0.

The unknown contrast function which relates the electromagnetic features of the object and the ones of the host medium is defined in $\boldsymbol{r} = (x, y) \in \Omega$ as :

$$\chi(\boldsymbol{r}) = \frac{\varepsilon_s(\boldsymbol{r}) - j\sigma_s(\boldsymbol{r})/\omega\varepsilon_0}{\varepsilon_b(\boldsymbol{r}) - j\sigma_b(\boldsymbol{r})/\omega\varepsilon_0} - 1 \tag{1.1}$$

where $\omega = 2\pi f$ and f is the working frequency.

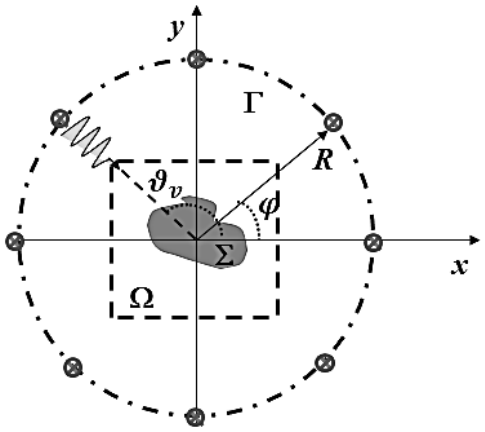

Figure 1.1 Pictorial view of the measurement configuration adopted to collect the scattering experiments.

The equations governing the scattering phenomenon for the geometry at hand for the generic v -th incident field ${E_i}^{(v)}$ can be expressed in an integral form as it follows:

$$ {E_s}^{(v)}(\boldsymbol{r}) = {k_b}^2 \int_{\Omega} G_b(\boldsymbol{r},\boldsymbol{r}')\,\chi(\boldsymbol{r}')E^{(v)}(\boldsymbol{r}')d\boldsymbol{r}' = \mathcal{A}_e\left[\chi E^{(v)}\right], \qquad \boldsymbol{r} \in \Gamma \tag{1.2} $$

$$ \begin{aligned} E^{(v)}(\boldsymbol{r}) &= {E_i}^{(v)}(\boldsymbol{r}) + {k_b}^2 \int_{\Omega} G_b(\boldsymbol{r},\boldsymbol{r}')\,\chi(\boldsymbol{r}')E^{(v)}(\boldsymbol{r}')d\boldsymbol{r}' \\ &= {E_i}^{(v)} + \mathcal{A}_i\left[\chi E^{(v)}\right], \qquad \boldsymbol{r} \in \Omega \end{aligned} \tag{1.3} $$

where ${E_s}^{(v)}(\cdot)$ and $E^{(v)}(\cdot)$ are the scattered field and total field induced in Ω, respectively, while $k_b = \omega\sqrt{\mu_b \varepsilon_b}$ is the wavenumber in the host medium.$\mathcal{A}_e$ and $\mathcal{A}_i$ are a short notation for the bilinear integral radiation operators, which are defined on $\mathrm{X} \times \mathrm{T}$, with $\mathrm{X} \subset L^{\infty}(\Omega)$ the subspace of the possible contrast functions, $\mathrm{T} \subset L^2(\Omega)$ a proper subspace for the total electric fields inside the object, and with value on two proper subspace for the scattered field outside and inside the object, $\mathrm{S}_e \subset L^2(\Gamma)$ and $\mathrm{S}_i \subset L^2(\Omega)$, respectively. $G_b(\boldsymbol{r},\boldsymbol{r}')$ is

the Green's function pertaining to the background medium. If the background is the free space $G_b(\boldsymbol{r},\boldsymbol{r}') = -j/4\, H_0^2(k_b|\boldsymbol{r}-\boldsymbol{r}'|)$, being H_0^2 the zero order and second kind Hankel function. In general case of heterogeneous non homogenous background, $G_b(\boldsymbol{r},\boldsymbol{r}')$ is pertaining to the particular reference scenario at hand and cannot be calculated in closed form, with exception of few canonical scenarios. For this reason, it is typically numerically calculated by using the reciprocity principle.

If the contrast source W, i.e. the current induced inside the scatterer, is considered as alternative auxiliary unknown, the data and state equation are rewritten as follows:

$$E_s^{(v)}(\boldsymbol{r}) = k^2 \int_\Omega G_b(\boldsymbol{r},\boldsymbol{r}')\, W^{(v)}(\boldsymbol{r}')d\boldsymbol{r}' = \mathcal{A}_e\left[W^{(v)}\right], \qquad \boldsymbol{r} \in \Gamma \tag{1.4}$$

$$\begin{aligned} W^{(v)}(\boldsymbol{r}) &= \chi(\boldsymbol{r}) E_i^{(v)}(\boldsymbol{r}) + \chi(\boldsymbol{r})\, k^2 \int_\Omega G_b(\boldsymbol{r},\boldsymbol{r}')\, W^{(v)}(\boldsymbol{r}')d\boldsymbol{r}' \\ &= \chi E_i^{(v)} + \chi \mathcal{A}_i\left[W^{(v)}\right], \qquad \boldsymbol{r} \in \Omega \end{aligned} \tag{1.5}$$

The inverse scattering problem aims at retrieving the unknown contrast $\chi \;\; \forall\, r \in \Omega$ from the scattered fields E_s measured for several receiving positions on Γ and for a set of known incident fields E_i.

As stressed in the Introduction, the inverse scattering problem is non-linear, because of the dependence of W or E on the unknown contrast function χ, and ill-posed because of the compactness of the radiation operator $\mathcal{A}_\mathrm{e}$ [*Bertero and Boccacci*, 1998]. Accordingly, only a finite number of scattering experiments is considered. In so doing, care has to be taken in choosing the positions $\vartheta_1, \ldots, \vartheta_N$ of the N transmitting probes and those of the M receiving ones, $\varphi_1, \ldots, \varphi_M$, in such a way to collect all the available information in a non-redundant fashion. This can be efficiently done by adopting the measurement strategies proposed in [*Bucci and Isernia*, 1997], wherein a Nyquist criterion is essentially suggested for the case at hand. The number of antennas acting both as transmitters and receivers is set on the

order of $2\,\mathcal{R}eal[k_b]\,a$, where a is the radius of the minimum circle enclosing the investigation domain Ω.

1.2 A new framework of the virtual scattering experiments

It is well known that the inverse scattering problems can take advantage from multiple (or multiview) experiments [*Bucci and Isernia*, 1997], i.e., from considering N incident fields impinging from angles ϑ_v, which produce a corresponding set of scattered fields, measured for M angles φ_m. Due to the linearity of the scattering phenomenon, with respect to the primary sources, a superposition of the incident fields, with known coefficient α_v, gives rise to a scattered field which is nothing but the superposition (with the same coefficients) of the corresponding scattered fields. In other words, if

$$\mathcal{E}_i(\boldsymbol{r}) = \sum_{v=1}^{N} \alpha_v \, E_i(\boldsymbol{r}, \vartheta_v) \tag{1.6}$$

is a superposition of the incident fields coming from the N different directions ϑ_v, then:

$$\begin{aligned} \mathcal{E}(\boldsymbol{r}) &= \sum_{v=1}^{N} \alpha_v \, E(\boldsymbol{r}, \vartheta_v) \\ \mathcal{W}(\boldsymbol{r}) &= \sum_{v=1}^{N} \alpha_v \, W(\boldsymbol{r}, \vartheta_v) \\ \mathcal{E}_s(\varphi) &= \sum_{v=1}^{N} \alpha_v \, E_s(\vartheta_v, \varphi) \end{aligned} \tag{1.7}$$

are, respectively, the total field, the contrast source and the scattered field which would be generated for the incident field (1.6).

From the simple reasoning above, it follows that performing several re-arrangements of the original experiments allows to build a set of new experiments. These new experiments are referred to as *Virtual* Experiments,

in order to remark that they do not require new experimental measurements as they are derived from a posteriori software procedures. No a priori information on the contrast function is needed to generate VE.

Clearly, VE are just a different way to consider or to re-weight the originally collected information. In fact, the amount of information carried by VE cannot exceed that of the original ones, and some information could be actually lost if they are not properly designed.

Note that one can recombine in different way the original experiments acting on the coefficients α_v, thus obtaining different total fields $\mathcal{E}$ and corresponding induced currents $\mathcal{W}$, exhibiting different given behaviors.

1.3 Conditioning scattering phenomena by means of suitably designed virtual scattering experiments

The natural question then arises of whether and how one can take advantage from VE, i.e., if their adoption can in some way simplify the problem.

The aim is the same which induce to implement a change of variable in solving a complex integral, or a change of investigation domain (f.i. from space/time domain to Laplace one) in solving a differential equation. In this respect, the VE could be considered as a linear transformation which allows to turn from the domain of the original experiments to a virtual domain in which the solution of the inverse scattering problem is more easily found.

An interesting chance is that of exploiting the VE to condition the scattering phenomenon, i.e. to enforce some given behaviors on the contrast sources or on the total fields inside the Region of Interest (ROI).

The ratio underlying this choice is very simple. In fact, it is well known that inverse scattering problems are non-linear in the relationship between the data and unknowns, as the induced currents and the total fields inside the targets are also unknown. Obviously, an exact knowledge of the internal fields or of the contrast sources would allow to linearize the inverse scattering problem. In this spirit, being internal fields and contrast sources unavailable

(as they depend on the contrast function) it can be argued that exploitation of any possible information on W or E can provide beneficial effects with respect to the possible occurrence of false solutions, thus simplifying the solution of the problem.

Taking profit from such a circumstance, one can re-cast the inverse problem in terms of virtual experiments rather than reasoning in terms of the original ones. In fact, if care has been taken in generating VE in order to avoid loss of significant information, the recasting of the problem in term of properly designed VE implies that the total fields (or the scattered fields) and contrast sources exhibit or approach some given behavior. As a consequence, the exploitation of such properties can be used to remove part of the difficulties that arise in the solution of the inverse problem, and, so, to develop more accurate inversion procedures.

In effect, in addition to the reduction of the nonlinearity, enforcing during the inversion procedure some property or structure on the total fields or contrast sources represents a new way to regularize the problem by acting on the auxiliary unknowns rather than the actual unknown (see subsection I.4.3).

Amongst the different possibilities and considering the case when the scatterers are hosted in a homogeneous background, let us focus on the idea of conditioning the scattering phenomenon in order to enforce a set of scattered fields or contrast sources exhibiting a circular symmetry around a set of different point r_p, called 'pivot points'. In a number of cases (see for instance Section 2.1) such request also implies a localization of the scattering phenomenon. In fact, (but for special cases) enforcing a circular symmetric scattered fields or contrast sources means that these latter seem to emerge from the considered pivot point.

Both the general idea (enforcing circular symmetry) as well as the related localization phenomenon open the way to innovative, convenient and effective solution procedures, which will be introduced and described in the next chapters of the thesis.

1.4 Linear sampling method as a way to synthesize circularly symmetric experiments

To design a set of VE, the scattered fields collected in the original experiments are the only available data, so that one has to act on them to pursue the design goal and to determine the superposition coefficients that define the set of VE.

As stressed in the previous section, amongst the different opportunities, let us consider the case when the scatterers are hosted in a homogeneous background and a corresponding design of the experiments such that each virtual scattered field exhibits (within some required accuracy) a circular symmetry around some pivot points r_p. By considering a proper set of pivot points r_p belonging to the scatterer's support (which can be estimated by a number of methods [*Catapano et al.*, 2007b, *Crocco et al.*, 2013]), the (original) multiview experiments can be turned in multipivot virtual ones (see fig. 1.2).

A possible way to calculate the unknown coefficients is to enforce that the scattered fields $\mathcal{E}_s$ resulting from a VE fulfill the following equation:

$$\mathcal{E}_s(\boldsymbol{r}, \boldsymbol{r_p}) = \sum_{v=1}^{N} {\alpha_v}^p \, E_s(\vartheta_v, \boldsymbol{r}) = G_b(\boldsymbol{r}, \boldsymbol{r_p}) \tag{1.8}$$

where $\boldsymbol{r} \in \Gamma$, $r_p \in \Omega$ is the considered pivot point, $\boldsymbol{\alpha_P} = \{{\alpha_v}^p\}$ with $p = 1,2,\ldots.\mathrm{P}$ identifies the combination coefficients required to implement the VE that give rise to the sought circular symmetry around the P pivot points r_p. In fact, by assuming that one is able to determine these coefficients, by virtue of eq. (1.6) they also modify the original amplitudes of the primary sources in such a way that their combined effect induces a current which radiates (on the measurement curve Γ) a circularly symmetric field around r_p [*Catapano et al.*, 2007b]. The right-hand side of eq. (1.8) is the far-field radiated

on Γ by an elementary source located in r_p (in TM case a filamentary current)[1].

Interestingly, eq. (1.8) is nothing but the discretized version of the well-known Far Field Equation (FFE), i.e., the basic (linear) equation underlying the LSM [*Cakoni and Colton*, 2006], with r_p playing the role of the sampling point. Accordingly, the problem cast in (1.8) is ill-conditioned and has to be solved through some regularization strategy. Its regularized solution is commonly exploited to recover the shape of unknown targets by simply plotting (in a logarithmic scale) the energy of the solution over the sampling grid.

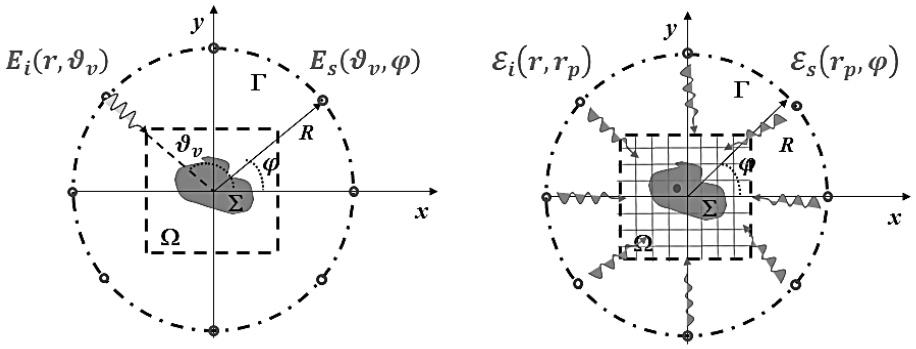

(a) (b)

Figure 2.2 On scattering experiments. (a) Original scattering experiments: the impinging waves on the investigated domain come from directions ϑ_v; multiple angles are used to obtain more information on the unknown target. (b) Virtual scattering experiments: the incident field is the result of the simultaneous excitation of the original primary sources according to a combination criterion ruled by the pivot point r_p.

Detail on the implementation of the regularized solution of FFE can be found in [*Catapano et al.*, 2007b, *Catapano et al.*, 2009b], where the Tikhonov regularization is adopted entailing an interesting effect on the synthesized contrast source. In fact, the minimum energy requirement (on the primary sources) enforced by the Tikhonov regularization corresponds to minimize

[1] Note that the discussion reported in this section can be generalized to the case of non homogeneous scenario. In this respect, the scattered field is enforced to resemble on Γ as a field radiated by an elementary source located inside the reference scenario (see Section 1.6.1 for more details).

the non-radiating component [*Marengo et al.*, 2000, *Marengo and Ziolkowski*, 2000, *Devaney and Wolf,* 1973] of the contrast sources [*Crocco et al.*, 2012b].

By construction, the radiating component of this contrast source will be circularly symmetric around the selected pivot point, whereas it is not possible to foresee its non-radiating behavior (as one is acting on the scattered fields). Nevertheless, the assumption of a circularly symmetric contrast source allows to include the part of non-radiating sources which is circularly symmetric, while the non-radiating or poorly radiating angularly varying sources possibly induced by the virtual incident field are just neglected, as they are expected to be small. As a consequence, being the VE built by adopting the Tikhonov regularization (which enforced a minimum energy requirement), recasting the problem in terms of VE is by itself a form of regularization.

In conclusion, in light of the above reasoning, as long as eq. (1.8) is fulfilled in a regularized sense, the resulting virtual contrast source will exhibit an essentially circularly symmetric structure with respect to the pivot point at hand, while angularly varying (radiating and non-radiating) contrast sources are instead expected to be small and negligible. [*Crocco et al.*, 2012b].

To get a better understanding of all the above, let us report a numerical example with a scattering system made of two obstacles in free space. The ROI is a square of dimension $1.6\,\lambda \times 1.6\,\lambda$ (λ is the considered wavelength) which is assumed to embed the unknown targets and is discretized in $\mathrm{N_c} = 64 \times 64$ cells (following [*Richmond*, 1965]). The targets have different shapes, as shown in fig. 1.3(a), and different electric features: a C-shape target with $\chi = 0.5$, and a circular target with $\chi = 0.85$.

In order to collect in a non-redundant way as much information as possible [*Bucci and Isernia*, 1997], the synthetic data are generated considering 17 plane waves evenly spaced in angle, while the corresponding scattered fields are measured in 17 evenly spaced angular positions on Γ at a distance $\mathrm{R} = 1.6\,\lambda$ from the origin. Finally random gaussian noise with a Signal to Noise Ratio (SNR) of $20dB$ is considered to simulate measurement uncertainties.

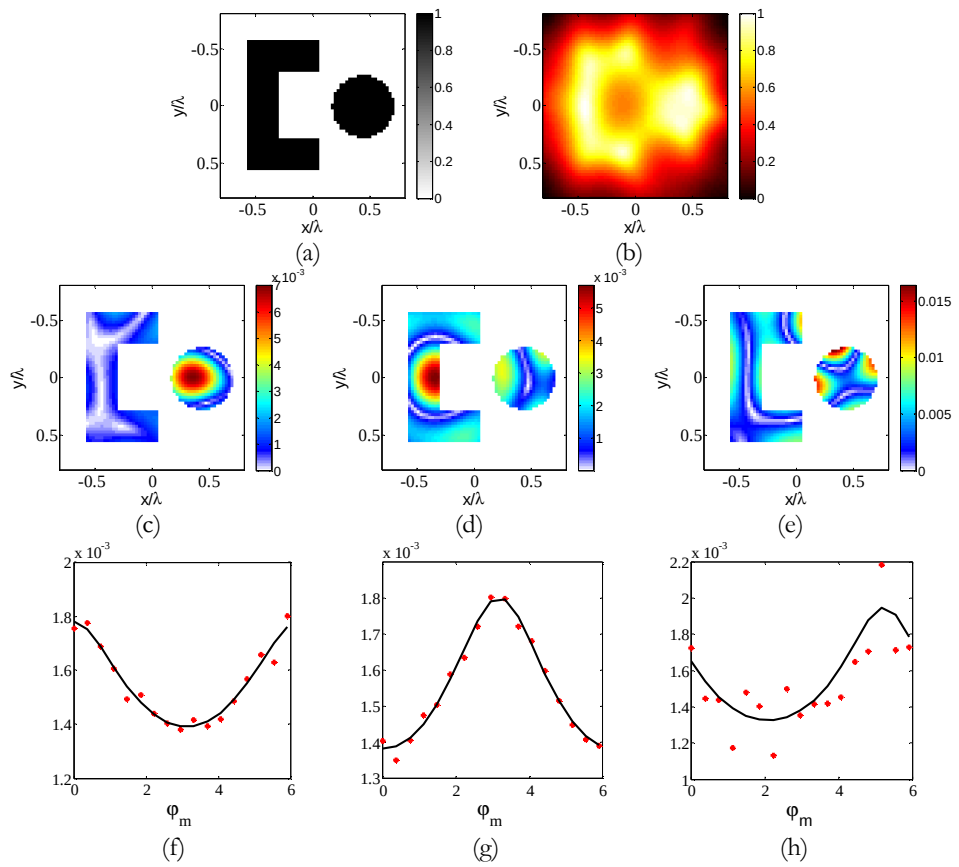

Figure 3.3. The LSM as a way to synthesize circularly symmetric virtual experiments: (a) actual support of the scattering system; (b) retrieved support via LSM energy indicator. Amplitude of virtual induced current for some sampling points: (c) r_p=(0.388 λ, -0.0125 λ), (d) r_p=(-0.413 λ, -0.0125 λ), (e) r_p=(0.288 λ, -0.513 λ). Fitting of LSM equation versus φ_m [rad] for the pivot points considered in (c), (d) and (e), respectively: continuous line represents the values assumed by the right hand side while the red points are the values assumed by the left hand side.

In fig. 1.3(b) the energy of the solution $\alpha_v{}^p$ is reported for all the points belonging to the grid in which the investigation domain Ω is divided. As it can be seen, when the sampling point belongs to the scatterers support an approximately focused and circular symmetric contrast source arises, see fig. 1.3(c)-(d). On the other hand, fig. 1.3(e) shows the virtual current for a sampling point that does not belong to the obstacle support. In this circumstance the current does not show any circular symmetry. This circumstance is also confirmed by fig. 1.3(f)-(h), which shown the data fitting pertaining to eq. (1.8), with respect to the different receiver positions φ_m. When the pivot point does not belong to the support of the scatterer the

solution becomes unbounded and the virtual scattered field does not fit anymore the function $G_b(\boldsymbol{r}, \boldsymbol{r_p})$.

It is worth noting that determining the required set of superposition coefficients $\{\alpha_v{}^p\}$ for the design of circularly symmetric experiments corresponds to solve the problem of focusing an electromagnetic wave in an unknown environment. This is sort of canonical problem, which has been broadly addressed in the literature by means of various approaches. Apart from the LSM, other methods can be considered for the design of VE. These latter may include the FM [*Kirsch*, 1999, *Di Donato,* 2013], adaptive time reversal procedures [*De Rosny et al.*, 2010, *Fink and Prada*, 2001, *Devaney et al.*, 2005] or other more sophisticated methods to achieve field focusing in partially unknown environments [*Crocco et al.*, 2012c].

Among the possible choices, in this thesis a procedure based on the LSM [*Colton et al.*, 2003, *Catapano et al.*, 2007b] is adopted as VE design tool, as it only entails a simple linear processing of the field scattered and the computation of the Singular Value Decomposition (SVD) of the matrix data [*Catapano et al.*, 2007b]. Moreover, LSM yields an estimate of the target's support, which is useful to properly locate the pivot points.

1.5 On the choice of pivot points

The possibility of actually achieving truly circularly symmetric contrast sources and scattered fields is related to the actual support of the scatterer. Luckily, a number of powerful methods for the estimation of such a support do exist [*Crocco et al.*, 2013]. In this respect, the LSM is an effective candidate to pursue this task. In fact, a generalized solution of FFE is such that the l_2-norm of the coefficients $\alpha_v{}^p$, i.e.:

$$\|\alpha_P\|_\Gamma^2 = \sum_{v=1}^{N} |\alpha_v{}^p|^2 \tag{1.9}$$

becomes unbounded when r_p approaches the boundaries from the inside and when r_p does not belong to the support of the scatterer (see fig. 1.3). Therefore, the energy of ${\alpha_v}^p$ plays the role of a support indicator, which is simply obtained by sampling the investigation domain Ω into a grid of points, solving the FFE in those points and then plotting the corresponding values of $\|\alpha_P\|$. In particular, the normalized indicator function, as defined in [*Catapano et al.*, 2009b]:

$$\Upsilon = \frac{\log_{10}\|\alpha_P\| - \log_{10}\|\alpha_P\|_{max}}{min(\log_{10}\|\alpha_P\| - \log_{10}\|\alpha_P\|_{max})} \tag{1.10}$$

can be used. Υ continuously varies between 0 and 1 and assumes its largest values in points belonging to the scatterers. Note that $\|\alpha_P\|_{max}$ is the largest value in the grid of points belonging to Ω.

Once the unknown target support is estimated, the choice of the pivot points has to ensure that the resulting VE are capable of enforcing the expected behavior of the contrast sources and scattered fields. Hence, pivot points whose corresponding virtual scattered fields more closely resemble cylindrical waves should be preferred. In fact, such a condition entails a better circularity of the scattered fields $\mathcal{E}_s$ and contrast sources $\mathcal{W}$. In particular, since the contrast source's support is constrained onto Σ, it is expected that the induced currents for r_p very close to the estimated boundary will not show an exact circular symmetry with respect to r_p [*Catapano et al.*, 2007b, *Crocco et al.*, 2013]. Obviously, no focusing at all of the induced current is possible for points outside of the scatterer. This physical observation corresponds to what is foreseen by LSM theory, according to which the energy of the solution $\|\alpha_P\|$. blows up when $\boldsymbol{r_p}$ approaches the boundary of the scatterer (see fig. 1.3) [*Colton et al.*, 2003].

Accordingly, the choice of the pivot points is carried out following the simple rules which follow.

First of all, the pivot points are chosen among those points that are understood to belong to the estimated support, as provided by Υ. Obviously,

they are not meant as a sampling of the scatterer permittivity, which is unknown.

As far as the number of pivot points and independent scattering experiments is concerned, it depends on the dimensions of the scatterer [*Bucci and Isernia*, 1997], so that a number of pivot points in the order of that deriving from the estimated dimensions of the scatterer (via Υ) is chosen. Note that it is important not to underestimate the number of experiments, so to carry all possible information gathered by the original experiments in the virtual framework[2]. Conversely, considering a larger number would only have a drawback in terms of computational burden. In some cases it may be useful or even appropriate to consider a larger number of pivot points (see Section 2.1.3).

Finally, as far as their location is concerned, the pivot points should be such that enforcing a circular contrast source is possible. Therefore, they should be preferably located in those parts of the region under test where Υ attains values close to 1, as these are the point where enforcing a circularly symmetric source is expected to be simpler [*Catapano et al.*, 2007b, *Crocco et al.*, 2012a, *Crocco et al.*, 2013]. In doing so, one should also avoid to cancel any significant information carried by the original experiments. To this end, pivot points must be chosen not too close each other, as the information carried by VE of clustered pivots would be nearly the same. In practice, the available pivot points are evenly spaced within the estimated support.

[2] Actually, part of the information collected in the original experiments is used in the pre-processing step to estimate the target support.

1.6 New understanding and interpretation of recently introduced inversion strategies

In this section, two inversion methods recently introduced in literature are briefly recalled. Both techniques are here reinterpreted in the light of the reasoning reported in the above sections, which shows the interesting possibility of conditioning the scattered field by means of the design of suitable VE.

It is important to highlight that although the FFE underlying the LSM is herein used to design the VE, the methods which are recalled in this Chapter and are introduced in the next one can be also applied by using different procedures to achieve a conditioning of the scattering phenomenon, as stressed at the end of Section 1.4.

1.6.1 An effective linear approximation of the internal field

In order to avoid non-linear optimization for quantitative imaging, recently a linear model based approximation has been developed in [*Crocco et al.*, 2012a] and successively extended in [*Di Donato et al.,* 2016]. The approach has been introduced as a new scattering approximation based on the physical meaning of LSM, but a new understanding and a general interpretation can be given with respect to the framework of VE.

As explained in previous Sections, while the overall information content in the original experiments remains unchanged, their clever re-arrangements can allow to condition the scattering phenomena, in particular to enforce circular symmetry on the auxiliary unknowns (f.i. the total field).

In the VE design equation (1.8) the function $\alpha_v{}^p$ recombine the measured scattered field at a given receiver arising for the different transmitter's positions in such a way to match the field radiated by an elementary source located in the sampling point. Accordingly, provided that a solution of eq. (1.8) can be actually found, the data equation (1.2) can be revamped in terms of VE as:

$$\mathcal{E}_s(\boldsymbol{r},\boldsymbol{r_p}) = {k_b}^2 \int_{\Omega} G_b(\boldsymbol{r},\boldsymbol{r'})\,\chi(\boldsymbol{r'})\mathcal{E}(\boldsymbol{r'},\boldsymbol{r_p})d\boldsymbol{r'} = \mathcal{A}_e[\chi\mathcal{E}], \quad \boldsymbol{r} \in \Gamma \tag{1.11}$$

wherein $\mathcal{E}_s$, $\mathcal{E}$ are the virtual (measured) scattered and virtual (internal) total fields given by eq. (1.7).

The new eq.(1.11) is still non-linear in terms of the unknowns, as both χ and $\mathcal{E}$ are unknown. However, the peculiar nature of the design equation, which enforces the target to behave like a point-like scatterer (observing the scattered field on Γ), allows to enforce, at least approximately, a given behaviour for the scattered field, and hence to introduce an effective approximation for $\mathcal{E}$ in Ω.

In fact, according to [*Marengo and Ziolkowski*, 2000], a minimum energy solution of eq. (1.8) entails a scattered field in Ω which resembles the one pursued on Γ by the design equation (see fig. 1.3(f)-(g)) [*Catapano et al.*, 2007b, *Crocco et al.*, 2013]. This corresponds, by exploiting the continuity of the field's tangential component, to an analytic prolongation of the field from the measurement curve Γ inside the scatterer and up to the considered pivot point r_p.

Moreover, as long as eq. (1.8) can be solved in r_p, its solution can be used to define an incident field whose corresponding scattered field is a cylindrical wave pattern centered on Γ. Notably, such a scattered field is always the same regardless of the probed target (within the level of accuracy of the regularized LSM solution.) Conversely, the virtual incident wave depends on the scatterer under test through ${\alpha_v}^p$. Obviously, this is the opposite of what happens in usual scattering experiments, where the scattered field changes with the scatterer, while the incident field is independent from it.

This change of roles can be exploited to cast a new approximation of the relationship between the contrast and the scattered fields. In particular, when the sampling point is inside the scatterer's support the total field can be conveniently approximated by means of the following expression:

$$\mathcal{E}(\boldsymbol{r},\boldsymbol{r_p}) \approx \mathcal{E}_i(\boldsymbol{r},\boldsymbol{r_p}) + LP[G_b(\boldsymbol{r},\boldsymbol{r_p})] \tag{1.12}$$

wherein the first addendum at the right hand side is the incident field arising in the VE and the second addendum is a low pass version of the internal Green's function, where the low-pass filtering is meant to avoid the field singularity in the pivot point.

As it can be observed in eq. (1.12), this new powerful approximation consists in approximating the total field $\mathcal{E}$ arising in the VE framework as the contribution of the original incident fields as ruled by the coefficients $\alpha_v{}^p$ plus the elementary field pattern originating at the pivot point r_p [*Crocco et al.*, 2012a].

The field approximation (1.12) has been generalized in the case of partially known scenario [*Di Donato et al.,* 2016], where the ground truth at hand can be conveniently thought as a modification of a known non-homogeneous one.

The VE design equation is again pursued by means of the solution of the LSM but considering a partially known scenario [*Catapano and Crocco*, 2009], i.e. rewriting the equation (1.8) as:

$$\Delta\mathcal{E}_s(\boldsymbol{r},\boldsymbol{r_p}) = \sum_{v=1}^{N} \alpha_v{}^p \, \Delta E_s(\vartheta_v,\boldsymbol{r}) = G_b(\boldsymbol{r},\boldsymbol{r_p}) \tag{1.13}$$

where ΔE_s is the anomalous field, that is the scattered field due to the presence of obstacles or anomalies inside the reference scenario, $\Delta\mathcal{E}_s$ is the anomalous field arising in the VE and, finally, G_b is the elementary field pattern originating at the pivot point in the non-homogeneous reference scenario.

The solution of the distorted FFE (1.13) in the whole ROI and the selection of the pivot points r_p inside the anomaly support allow the design of the VE. Finally, if the problem is recast in term of these experiments, the field approximation (1.12) is generalized as:

$$\mathcal{E}(\boldsymbol{r},\boldsymbol{r_p}) = \sum_{v=1}^{N} {\alpha_v}^p \, {E_b}^{(v)}(\boldsymbol{r}) + LP\{G_b(\boldsymbol{r},\boldsymbol{r}_p)\} \tag{1.14}$$

wherein E_b is the background field arising in the reference scenario and the second addendum is a low pass filtered version of G_b.

Note that both approximations (1.12) and (1.14) take implicitly into account the nature of the scatterer/anomaly through the weighting function ${\alpha_v}^p$. As such, the above linear framework can cope with a class of dielectric profiles, both in terms of dimension and contrast values, widely exceeding the BA, as shown in [*Di Donato et al.,* 2015a], and DBA.

More details concerning the method's implementation and the field approximation can be found in [*Crocco et al.,* 2012a, *Di Donato et al.,* 2016].

1.6.2 A 'fictitious measurements' strategy for aspect limited data

The VE framework can be exploited not only to introduce the above linearized approaches, but also, (and more interesting) to counteract the additional specific difficulty that one could cope with the solution of an inverse scattering problem, when both primary sources and measurement probes cannot surround the region under test. This happens, for instance, in case of subsurface imaging (as described in the last Chapter) or cross-hole borehole imaging, where just 'aspect limited' data pertaining to a reduced angular sector are available.

In this respect, the approximation (1.12) provides an analytical expression for the fields in the ROI. Since the spatial behavior of the scattered field is known everywhere for each VE, one can predict the value of the field in locations where physical measurements are not possible or present. Then, additional equations can be introduced in order to get profit from the expected behavior of the scattered fields in locations other than the measurement point on Γ.

In particular, one can enlarge the set of measurement data, by adding a set of 'fictitious measurements', located in ${r_r}^*$ on a fictitious curve Γ^*

(complementary to Γ), in such a way to restore the full aspect configuration [*Di Donato and Crocco,* 2015]. The value of the (virtually measured) scattered field at these fictitious locations would be obviously given by $G_b(\boldsymbol{r_r}^*, \boldsymbol{r_p})$. According to the above, the (virtual) data equation can be suitably rewritten as:

$$k_b{}^2 \int_{\Omega} G_b(\boldsymbol{r}, \boldsymbol{r}')\, \chi(\boldsymbol{r}') \mathcal{E}(\boldsymbol{r}', \boldsymbol{r_p}) d\boldsymbol{r}' = \begin{cases} \mathcal{E}_s(\boldsymbol{r}, \boldsymbol{r_p}) \text{ if } \boldsymbol{r} = \boldsymbol{r_r} \in \Gamma \\ G_b(\boldsymbol{r}, \boldsymbol{r_p}) \text{ if } \boldsymbol{r} = \boldsymbol{r_r}^* \in \Gamma^* \end{cases} \tag{1.15}$$

where r_r and $r_r{}^*$ denote the actual and the fictitious measurement points, respectively.

Exploiting the achieved field conditioning, it could seem that one can place fictitious measurements as close as possible to the targets, i.e. inside Ω or even inside the scatterers. However, analytical prolongation (which allows for fictitious measurements) works fine outside the scatterers, while it becomes more critical when going inside the scatterers, wherein it may more easily fail. Hence, a convenient and more reliable choice amounts to place the fictitious probes approximately at the same distance of that between the investigated domain and the actual probes.

2
Virtual experiments based solution approaches for inverse scattering

Introduction

In this Chapter, three different approaches for quantitative solution of 2D scalar inverse scattering problems are presented and described. The developed methods share with the linear approximation recalled in the Section 1.6.1 the idea of exploiting suitably designed VE (rather than the multi-view multi-static ones), built in such a way to induce a specific behavior on the scattered field and contrast source.

However, the developed methods are indeed very different from the linear approximation recalled in the Section 1.6.1. In fact, they still take into account the non-linear nature of the inverse scattering problem. Obviously, these circumstances give rise to definite advantages in terms of performances.

In particular, the first method acts on currents rather than fields, which is assumed to be focused and circularly symmetric. The core of the approach is represented by an original approximation of contrast sources, which allows to derive an explicit algebraic relationship between induced currents and contrast function.

The second methods, which acts again on the currents, consists in a new regularization scheme for CSI, in which the scattering problem is recast into a set of VE, and circularly symmetric contrast sources are looked for. In particular, a penalty term is added to the usual CSI cost functional, in order to account for the symmetry of the auxiliary unknowns.

Finally, in the last technique, the linear approximation recalled in Section 1.6.1 is exploited within an iterative scheme, in which Green's functions, VE and corresponding approximations are updated at each step on the basis of intermediate results. Notably, this procedure takes into account

the nature of the scatterer from the first step and, as such, it is expected to outperform the standard DBIM [*Chew and Wang*, 1990], while preserving its flexibility and simplicity. Notably, by proceeding through linear approximations the approach also allows to get profit in as simple fashion from some recently introduced regularization technique (See Section 3.4).

Examples dealing with both numerical and experimental data are provided in the following to assess the effectiveness of proposed methods.

2.1 A direct algebraic reconstruction

Unlike the linear method in Section 1.6.1, the algebraic solution method acts on currents and it allows to take into account in a simple fashion (part of) the non-radiating contrast sources [*Marengo et al.*, 2000, *Marengo and Ziolkowski*, 2000, *Devaney and Wolf,* 1973]. As such, the proposed quantitative inversion method is expected to largely exceed the range of effectiveness of the traditional weak scattering approximations.

The approach takes advantage of two main ideas. First, the original scattering experiments are re-arranged in such a way to give rise to induced currents virtually focused in a set of pivot points belonging to the imaged domain. Second, a novel analytical approximation is introduced for the currents arising in the designed VE, which holds true in a neighborhood of the pivot point. Such an approximation relies on an overlooked theorem for Bessel functions and provides an explicit dependence of the focused currents on the contrast function.

As discussed in the following, these two ideas allow to recast the inverse problem in such a way that the values of the contrast in the pivot points can be achieved by solving a diagonal system of algebraic equations. Then these latter are simply interpolated in order to achieve the unknown properties of the whole ROI. As a consequence, provided the proposed approximation holds true, the inverse scattering problem is solved by means of closed form formulas, and, hence, in a reliable and extremely fast manner.

Note that the applicability of DARE depends on the limitations of the design step, as well as on the validity of the approximations introduced on the contrast sources. As shown through examples in the following and in Section 2.4, the proposed method is capable of imaging targets that are usually tackled by means quantitative inversion tools which are both computationally demanding and prone to false solutions occurrence.

2.1.1 A new approximation for focused contrast sources

Let us consider a set of VE capable to induce currents having a focused distribution around given pivot points r_p. Moreover, let us make the additional assumption that the contrast function is slowly variable around each pivot point, so that one can consider the medium to be approximately homogeneous in a neighborhood of r_p.

By exploiting canonical solutions [*Jones*, 1986] in a reference system centered on the pivot point, the contrast source $\mathcal{W}$ arising in the VE can be expressed as a superposition of Bessel functions, i.e.:

$$\mathcal{W}(\boldsymbol{r}, \boldsymbol{r_p}) = \sum_{n=-\infty}^{+\infty} {w_n}^p J_n(k_p \rho)\, e^{jn\left(\phi_p - \frac{\pi}{2}\right)} \tag{2.1}$$

where ϕ_p and $\rho = |\boldsymbol{r} - \boldsymbol{r_p}|$ are the polar coordinates with respect to r_p, ${w_n}^p$ is an amplitude coefficient, $J_n(\cdot)$ is the Bessel function of order n and $k_p = k_b\sqrt{1+\chi_p}$ and χ_p are, the 'local' wavenumber and 'local' values of contrast in r_p (and its neighborhood), respectively.

Observing that the induced current at hand is focused, and remembering the behavior of Bessel functions in the origin, it follows that the only term which survives in (2.1) in a neighborhood of the pivot point is the one with $n = 0$. As a result, in such a neighborhood the actual contrast sources can be approximated by means of the zero order Bessel function, whose argument depends on the unknown properties of the medium in r_p, i.e.,:

$$\mathcal{W}(\boldsymbol{r}, \boldsymbol{r_p}) \approx {w_0}^p J_0(k_p\, \rho), \qquad \boldsymbol{r} \in \mathcal{I}_{R_p}(\boldsymbol{r_p})$$

(2.2)

where $\mathcal{I}_{R_p}(\boldsymbol{r_p})$ is a circular neighborhood of r_p of radius R_p. Notably, expression (2.2) takes into account both the radiating and non radiating part of the source around the pivot point.

Then, advantage can be taken from the Multiplication Theorem [*Abramowitz and Stegun*, 1964] for Bessel functions, according to which:

$$\varepsilon^{-\nu} J_\nu(\varepsilon z) = \sum_{n=0}^{\infty} \frac{1}{n!} \left[\frac{(1-\varepsilon^2)z}{2}\right]^n J_{\nu+n}(z)$$

(2.3)

so that:

$$J_0(k_p\, \rho) = \sum_{n=0}^{\infty} \frac{1}{n!} \left(\frac{-\chi_p k_b\, \rho}{2}\right)^n J_n(k_b\, \rho)$$

(2.4)

As shown in Appendix A, this series is convergent for any χ_p.

Note expression (2.4) has a two-fold interest. First, as a neighborhood of r_p is considered, by truncating eq. (2.4) to the first few terms, it is possible to rewrite (2.2) as follows:

$$\mathcal{W}(\boldsymbol{r}, \boldsymbol{r_p}) \approx {w_0}^p \left\{ J_0(k_b\, \rho) - \frac{1}{2}\, \chi_p\, k_b\, \rho\, J_1(k_b\, \rho) + \frac{1}{8}\, {\chi_p}^2\, (k_b\, \rho)^2 J_2(k_b\, \rho) \right\}$$

(2.5)

where the argument of the Bessel functions just now depends on the background medium.

Second, it is possible to take into account in a simple fashion (part of) the non-radiating contrast sources [*Marengo et al.*, 2000, *Marengo and Ziolkowski*, 2000, *Devaney and Wolf,* 1973] and, moreover, to separate the radiating and non radiating parts of the source. As shown in Appendix B, an analytical expression for the radiating part of $\mathcal{W}$ is obtained, i.e.:

$$\mathcal{W}_{RAD}(\boldsymbol{r}, \boldsymbol{r}_p) \approx {w_0}^p \left\{ \frac{{R_p}^2}{4} \left[{J_0}^2(k_b R_p) + {J_1}^2(k_b R_p) \right] - \frac{\chi_p}{4} {R_p}^2 {J_1}^2(k_b R_p) \right.$$
$$+ \frac{{\chi_p}^2}{48} {k_b}^2 {R_p}^4 \left[J_0(k_b R_p) J_2(k_b R_p) \right.$$
$$\left. \left. + J_1(k_b R_p) J_3(k_b R_p) \right] \right\} J_0(k\rho)$$

(2.6)

where each term in (2.5) gives a contribution, while the non radiating part is simply the difference between $\mathcal{W}$ and $\mathcal{W}_{RAD}$.

Eq.(2.5) is a remarkable result, as it provides (within the range of validity of the approximation resulting from the truncation) an explicit algebraic relationship between $\mathcal{W}$ and χ_p, which is linear if the expansion is truncated to the second term, and quadratic otherwise.

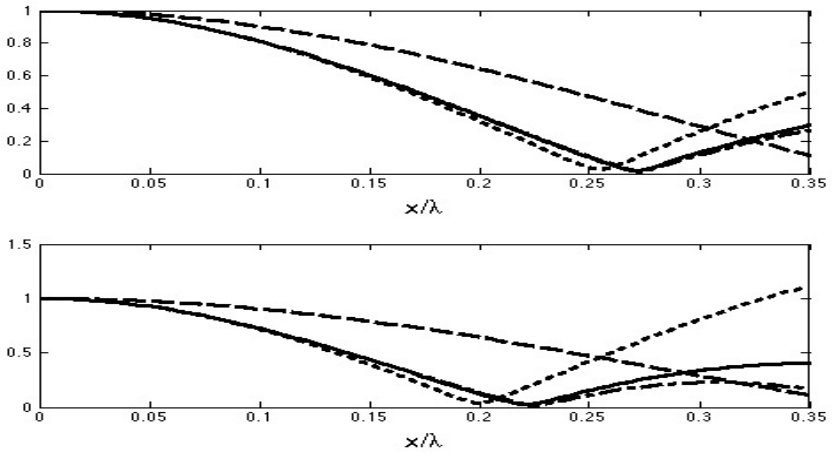

Figure 2.1 Behavior of the Bessel function amplitude (solid line) as compared to the approximation (2.4) truncated at the first term (dashed line), at the second term (dotted line) and at the third term (dash-dot line). Two complex contrast values are reported: in the upper panel $\chi_v = 1 - 0.05i$, while in the lower one $\chi_v = 2 - 0.1i$. The background medium is lossless.

Of course, eq. (2.5) has a limited validity, which depends on the distance ρ from the considered pivot point, as well as from the local value of the contrast. As expected, (see also fig. 2.1) the larger ρ (and the higher is χ_p),

the smaller the range of validity of the approximation (2.5). As χ_p is the unknown of the problem, the determination of the actual geometric neighborhood of validity is not trivial (see the following subsections for further discussion).

However, in the proximity of the pivot point it is possible to express the contrast source as an algebraic function of the contrast times a scalar variable ($w_0{}^p$), which provides the basis for a new and effective inversion method.

2.1.2 A new algebraic solution procedure

To introduce the proposed inversion method, let us first rewrite the scattering equations with respect to the relevant VE framework. In particular, the state equation (1.5) can be rewritten as:

$$\mathcal{W}(\boldsymbol{r},\, \boldsymbol{r_p}) = \chi(\boldsymbol{r})\mathcal{E}_i(\boldsymbol{r},\boldsymbol{r_p}) + \chi(\boldsymbol{r})\, {k_b}^2 \int_{\mathcal{I}_{R_p}} G(\boldsymbol{r},\boldsymbol{r'})\, \mathcal{W}(\boldsymbol{r'},\, \boldsymbol{r_p}) d\boldsymbol{r'} + \chi(\boldsymbol{r})\, {k_b}^2 \int_{\bar{\mathcal{I}}_{R_p}} G(\boldsymbol{r},\boldsymbol{r'})\, \mathcal{W}(\boldsymbol{r'},\, \boldsymbol{r_p}) d\boldsymbol{r'}, \quad \boldsymbol{r} \in \Omega \tag{2.7}$$

As approximations (2.2) and (2.5) are going to be used, the domain Ω is divided in two non-overlapping subdomains: the neighborhood $\mathcal{I}_{R_p}$ of r_p and its complementary set with respect to Ω, $\bar{\mathcal{I}}_{R_p}$. As long as the currents induced by the VE are well focused, and $\mathcal{I}_{R_p}$ is properly chosen, it is possible to neglect the second integral.

Similarly, the data equation (1.4) can be split into two contributions:

$$\mathcal{E}_s(\boldsymbol{r},\boldsymbol{r_p}) = {k_b}^2 \int_{\mathcal{I}_{R_p}} G(\boldsymbol{r},\boldsymbol{r'})\, \mathcal{W}(\boldsymbol{r'},\, \boldsymbol{r_p}) d\boldsymbol{r'} + {k_b}^2 \int_{\bar{\mathcal{I}}_{R_p}} G(\boldsymbol{r},\boldsymbol{r'})\, \mathcal{W}(\boldsymbol{r'},\, \boldsymbol{r_p}) d\boldsymbol{r'}, \quad \boldsymbol{r} \in \Gamma \tag{2.8}$$

where the second term at the right hand side can be again neglected.

A. Inversion procedure

By means of the explicit relationship between the $\mathcal{W}$ and χ_p and following the analytical developments reported in Appendix C, it is possible to particularize and merge eqs. (2.7) and (2.8) for each pivot point into the single third order algebraic equation:

$$\bar{A}^p {\chi_p}^3 + \bar{B}^p {\chi_p}^2 + \bar{C}^p \chi_p + \bar{D}^p = 0 \tag{2.9}$$

where the only unknown is the value of the contrast in the considered pivot point. In fact, the scalar variable ${w_0}^p$ can also be expressed by means of eq. (C.2) in terms of the local contrast function χ_p. Eq.(2.9) is the core of the new inversion method, as it allows to estimate the unknown contrast in the pivot point at hand by solving a cubic equation, which admits, as well known, a closed form solution [*Cardano*, 1545]. Hence, the required estimate is obtained in a very efficient way, without resorting to iterative methods.

To evaluate the overall contrast, one can consider all the pivot points for which the VE are designed, so that the overall inverse scattering problem can be formulated as a diagonal system of polynomial equations:

$$A(\mathrm{X} \odot \mathrm{X} \odot \mathrm{X}) + B(\mathrm{X} \odot \mathrm{X}) + C\mathrm{X} + D = 0 \tag{2.10}$$

where $\odot$ denotes the Hadamard product between vectors, $X = [\chi_1 \cdots \chi_k \cdots \chi_P]^T$ is the vector that contains the punctual values of the unknown contrast in the selected pivot points r_p, and $(\,)^T$ denotes the matrix transposition. Finally, A, B, C and D are diagonal matrices given by:

$$A = \begin{bmatrix} \bar{A}^1 & \cdots & 0 \\ \vdots & \ddots & \vdots \\ 0 & \cdots & \bar{A}^P \end{bmatrix}$$

$$B = \begin{bmatrix} \bar{B}^1 & \cdots & 0 \\ \vdots & \ddots & \vdots \\ 0 & \cdots & \bar{B}^P \end{bmatrix}$$

$$C = \begin{bmatrix} \bar{C}^1 & \cdots & 0 \\ \vdots & \ddots & \vdots \\ 0 & \cdots & \bar{C}^P \end{bmatrix}$$
$$D = \begin{bmatrix} \bar{D}^1 & \cdots & 0 \\ \vdots & \ddots & \vdots \\ 0 & \cdots & \bar{D}^P \end{bmatrix} \quad (2.11)$$

and the expression of the different elements can be found above in eq. (C.4).

Starting from the solution of (2.10), which provides the values of the contrast function in the P considered pivot points, an interpolation is performed in order to obtain the image of the reconstructed contrast over the investigated region. In particular, a linear interpolation is adopted in the following because of the assumed slow spatial variations of the contrast.

Note that an important feature of the proposed method is the very low computational burden it requires. In fact, for each pivot point the solution is achieved in real time by solving the eq. (2.9) and independently from each other. In fact, the diagonal nature of the algebraic system (2.10) allows to handle the different pivot points in parallel.

B. Managing false solutions

The non-iterative inversion method described above is extremely effective and efficient, and it has the unique feature of allowing to solve the non-linear inverse scattering problem through simple algebraic tools. Note that the achieved equations preserve the non-linearity of the problem, while allowing to deal with a kind of localized scattering phenomenon, which translates into a diagonal relationship between the data and the unknown contrast in the pivot points.

Notably, diagonalization and algebraic nature also allow to manage in an effective fashion the false solutions problem [*Isernia et al.,* 2001]. In fact, the third degree polynomial considered in the method admits three roots, so that two of them correspond to false solutions. In the canonical case of targets embedded in free space, these roots are expected to be spaced (in the average) of 120°, so that only one of them is physically realizable, i.e. only one root will have a positive real part and a negative imaginary part. In addition, a

priori information concerned with the expected 'slow' spatial variability of the contrast can be possibly exploited.

Similar 'physical feasibility' arguments are expected to hold in more general cases.

C. On the Choice of R_p and of the order of Bessel Expansions

In the proposed method, the radius R_p is a free parameter, whose choice obeys a very obvious trade off. In fact, from one side, one needs a value of R_p as large as possible, as this will reduce the error arising from neglecting the second term in (2.7) and (2.8). On the other side, large values of R_p may imply lack of validity of both (2.2) and (2.5). Notably, as already stated, the 'optimal' choice of R_p also depends on the value of χ_p, which is unknown.

By taking advantage of the very fast inversion allowed by the obtained diagonal algebraic formulation, an 'a posteriori' criterion is suggested in order to choose a suitable value of R_p for all pivot points. In particular, after using several trial values for R_p and estimating the corresponding contrast functions, the fitting achieved in eq. (1.5) is quantified. To this end, the following residual is introduced:

$$Res(R_p) = \sum_p \frac{\left\| \mathcal{W}(\boldsymbol{r}, \boldsymbol{r}_p) - \chi\, \mathcal{E}_i(\boldsymbol{r}, \boldsymbol{r_p}) + \chi \mathcal{A}_i[\mathcal{W}(\boldsymbol{r}, \boldsymbol{r}_p)] \right\|_\Omega^{\,2}}{\left\| \mathcal{E}_i(\boldsymbol{r}, \boldsymbol{r_p}) \right\|_\Omega^{\,2}} \tag{2.12}$$

where χ and $\mathcal{W}$ are the contrast and the contrast sources obtained for a given radius R_p. In particular, $\mathcal{W}$ is evaluated as in eq. (2.2), where ${w_0}^p$ is calculated by using eq. (C.2).

To set R_p, the residual (2.12) is appraised for different tentative values (belonging to a limited range), as well as for second and third order expansions of the Bessel function (see eq. (2.5)) Then, the value corresponding to the minimum residual error is picked as the most appropriate one.

The above outlined 'tuning' procedure entails the repeated execution of the (computationally negligible) task of solving the system of equations (2.10). As such, it may result in an increase of the overall computation time required by the method. However, the optimization procedure is intrinsically parallel, as R_p is equal for all pivot points and each residual value associated to a specific radius R_p can be computed independently from the other ones. Thus, by relying on such an implicit parallelism, the inversion can be carried out in real time by considering a number of processors in the order of the number of tentative radii.

Even if in bidimensional case, dealt with in the Section, all results are already achieved almost in real time, this is an interesting point to address in the view of the future extension to 3D problems, wherein parallelization can be exploited to achieve, also in this more challenging case, real time imaging results.

2.1.3 Method's assessment

In the following a 'controlled' assessment is carried out with simulated data. In these examples, one or more unknown objects are positioned inside a square domain of side L and, following [*Bucci and Isernia*, 1997], the same number of receivers M and transmitters N, both located on a circumference Γ of radius R, is considered, with $\mathrm{N} = \mathrm{M} = 2\,\mathcal{R}\mathrm{e}[k_b]\mathrm{L}/\sqrt{2}$. The scattered field data, simulated by means of a full-wave forward solver based on the method of moments, are corrupted with a random Gaussian noise with given SNR.

To evaluate the accuracy of the retrieved contrast function, the normalized mean square error is defined as $err = \frac{\|\chi - \tilde{\chi}\|^2}{\|\chi\|^2}$ where χ is the actual contrast profile and $\tilde{\chi}$ the estimated one.

The first example deals with a lossless circular cylinder embedded in free space, see fig. 2.2(a), with $\chi = 1$ and $\mathrm{L} = 1.5\,\lambda$. Following [*Richmond*, 1965], a number of cells N_c equal to 64×64 is used, while $\mathrm{N} = \mathrm{M} = 15$, $\mathrm{SNR} = 20$ dB and $\mathrm{R} = 3\,\lambda$.

First, the target support is estimated from the LSM indicator (1.10) [*Colton et al.*, 2003, *Catapano et al.*, 2007b] over the imaged domain, see fig. 3.2(b). Then, the pivot points are uniformly spread over the estimated support, see fig. 2.2(b), and the coefficients pertaining to the LSM solutions in the selected pivot points are used to define the VE. Note, respect to the guidelines given in Section 1.5, the pivot points are also selected near to the border of the scatterer, as the contrast function is obtained by interpolating each punctual value χ_p.

Finally, the diagonal system of third degree algebraic equations is solved, adopting the criteria in Section 2.1.2 to choose the 'physically feasible' root of the algebraic equation in each pivot point. The real and imaginary parts of the obtained contrast values are shown in figs 2.2(c) and (d), respectively. Note that the value of the imaginary part of the contrast in some pivot points is clipped to zero to guarantee both the expected slow variability and the physical feasibility condition (i.e., $\mathcal{I}m\{\chi\} \leq 0$).

The retrieved contrast function, resulting from the linear interpolation of the punctual values estimated in the selected pivot points (figs. 2.2(c)-(d)), is shown in figs. 2.2(e)-(f). As it can be seen, the real part is accurately estimated, and the lossless nature is also envisaged as the imaginary part is indeed negligible with respect to the real one. In the proximity of the scatterer boundary, the contrast is slightly underestimated, because of the reduced capability of the LSM to focus the currents. The final reconstruction error is as low as 8%.

The second example is the same one considered in Section 1.4, constituted by two different scatteres, a C shape target and a circle cylinder. As it can be noted from figs 2.3(e)-(f), notwithstanding the cumbersome nature of the objects, a quite accurate reconstruction, corresponding to $err = 34\%$, is achieved.

Many other examples have been considered in order to appreciate the potentiality of DARE method. In particular, an accurate validation analysis has been carried out by considering homogenous circular cylinders (as the one considered in fig. 2.2) with different radii and electromagnetic properties. The

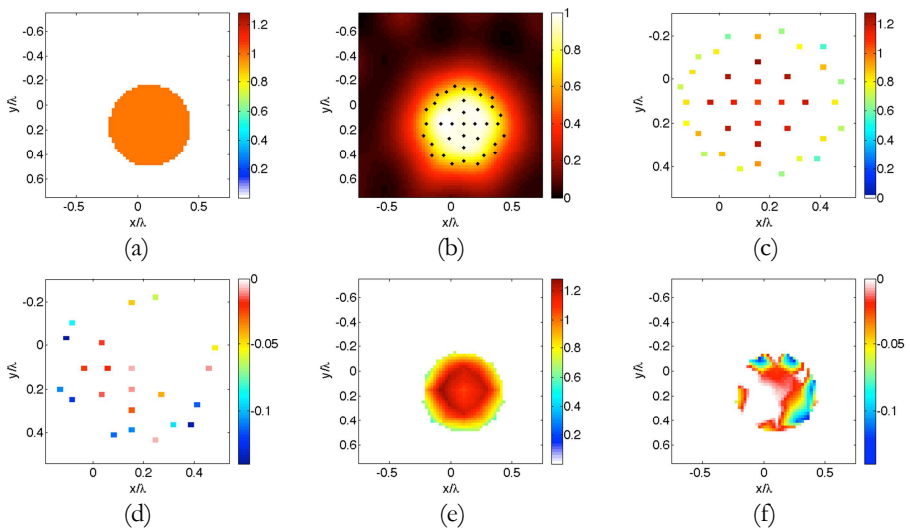

Figure 2.2. Numerical assessment of DARE. The circular homogeneous target: (a) real part of the reference profile; (b) LSM indicator map with the selected pivot points superimposed as dots; (c) real part and (d) imaginary part of punctual value of retrieved contrast, before interpolation; (e) real part and (f) imaginary part of retrieved contrast.

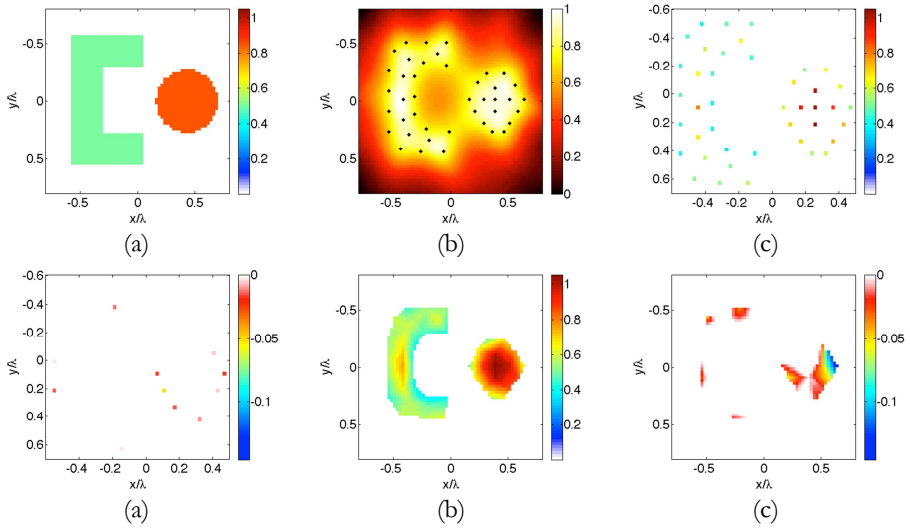

Figure 2.3. Numerical assessment of DARE. The C-O target: (a) real part of the reference profile; (b) LSM indicator with the selected pivot points superimposed as dots; (c) real part and (d) imaginary part of punctual value of retrieved contrast, before interpolation; (e) real part and (f) imaginary part of retrieved contrast.

method has worked fine as long as the LSM has been able to build focalized currents. In fact, for radii larger than $0.4\,\lambda$ or contrasts larger 2.5, the contrast sources recombined by means of the LSM solution turn out to be not focalized anymore and the hypothesis of applicability of the method is not fulfilled.

2.2 A regularized contrast source inversion

As discussed in Section I.4, in order to overcome the difficulty of the inverse scattering problem, a class of solution approaches that is broadly adopted is the one of modified gradient methods [*Kleinman and van den Berg*,. 1993, *van den Berg and Kleinman*, 1997, *Isernia et al.*, 1997, *Isernia et al.*, 2004, *Chen*, 2010], in which the inverse problem is cast as the minimization of a cost functional. Such a functional depends on both the unknown contrast and the auxiliary unknown, which can be the field in the ROI or the contrast source therein induced.

These methods do not require any approximation (but for the obvious discretization), nor an explicit solution of the forward problem at each step. However, due to the large number of unknown parameters, similar to other non-linear inversion schemes, modified gradient methods are based on local iterative optimization, so that they are prone to the occurrence of false solutions [*Isernia et al.*, 1997, *Isernia et al.,* 2001], and provide the correct result only for an initial estimate that lies in the attraction basin of the solution.

As it not possible to foresee in general whether or not the initial guess is 'good', regularization schemes are introduced in order to defeat the ill-posedness of the problem, as well as the occurrence of false solutions. In this respect, the regularization techniques described in Section I.4.1 are widely adopted. As these latter work by imposing constraints on the contrast function, the choice of the most suitable one depends on the expected contrast properties (for instance, smoothness, piecewise constant behavior and so on).

In this Section, different from the schemes recalled above, a novel strategy is explored, in which the non-linearity and ill-posedness of the problem are tackled by acting on the contrast sources and without relying on a priori information on the contrast function. Rather, even if deeply different, it may be related to the Subspace Optimization Method (SOM) [*Chen*, 2010], as also SOM pursues the inversion stability by acting on the auxiliary unknown.

In particular, it is again explored the possibilities offered by a set of VE, capable to induce contrast sources that are circularly symmetric, (in terms of spatial distribution of these sources, not of their shape or topology) with respect to some properly chosen points within the ROI. In particular, the VE are exploited in conjunction with the popular CSI scheme [*van den Berg and Kleinman*, 1997], which tackles the problem by looking for both the unknown contrast χ and the auxiliary unknown $\mathcal{W}$ (see Appendix D for more details).

2.2.1 A new contrast source regularization scheme

Let us assume that eq. (1.8) is applied to the whole imaging domain Ω. Then, let $r_p^1, \ldots, r_p^P$ be a set of P pivot points for which the equation is solved (in a regularized sense) and denote with $\boldsymbol{\alpha_1}, \ldots, \boldsymbol{\alpha_P}$ the sets of corresponding coefficients. Now, it is possible to recast the original scattering equation (1.4) and (1.5) in terms of the obtained VE in which a circular symmetry of the contrast sources around the selected pivot points is expected. With respect to the devised VE, the CSI scheme (D.1) is now recast in terms of the recombined data, as follows:

$$\Phi_{VE}\left(\chi, \mathcal{W}^{(1)}, \ldots, \mathcal{W}^{(P)}\right) = \sum_{p=1}^{P} \frac{\left\| \mathcal{W}^{(p)} - \chi \mathcal{E}_i{}^{(p)} - \chi \mathcal{A}_i\left[\mathcal{W}^{(p)}\right] \right\|_{\Omega}^2}{\left\| \mathcal{E}_i{}^{(p)} \right\|_{\Omega}^2} + \sum_{v=1}^{N} \frac{\left\| \mathcal{E}_s{}^{(p)} - \mathcal{A}_e\left[\mathcal{W}^{(p)}\right] \right\|_{\Gamma}^2}{\left\| \mathcal{E}_s{}^{(p)} \right\|_{\Gamma}^2} + \Phi\left(\mathcal{W}^{(1)}, \ldots, \mathcal{W}^{(P)}\right) \tag{2.13}$$

and equipped with an additional regularizing term Φ that account for the peculiar structure of the enforced virtual contrast sources, which reads:

$$\Phi\left(\mathcal{W}^{(1)}, \ldots, \mathcal{W}^{(P)}\right) = \sum_{p=1}^{P} \tau_p \left\| \frac{\partial \mathcal{W}^{(p)}}{\partial \phi_p} \right\|_{\Omega}^2, \boldsymbol{r} \in \mathcal{I}_{R_p}\left(\boldsymbol{r_p}\right) \tag{2.14}$$

where ϕ_p is the angular coordinate of a local polar reference system centered in r_p which spans the circular neighborhood $\mathcal{I}_{R_p}(\boldsymbol{r_p})$, and $\{\tau_p\}_1^P$ are non-negative parameters controlling the relative weight of such a regularization term.

The penalty term (2.14) is a way to enforce the expected contrast sources properties by minimizing the angular variation of each $\mathcal{W}^{(P)}$ around the pertaining pivot point r_p. It is important to note that, with respect to DARE, the currents must not be necessarily focused (it is sufficient they are circularly symmetric), which implies a significant enlarging of the range of applicability.

Notably, the functional Φ encourages also the research of circularly symmetric non radiating sources, while angularly varying (radiating and non-radiating) contrast sources are instead neglected, as they are expected to be small. However, angularly varying currents are herein penalized, but not strictly forbidden.

2.2.2 Implementation of the penalty term

While the reader is referred to Appendix D and to [*Isernia et al.*, 1997] for the general structure of the optimization procedure, the implementation of the new regularization term in the framework of a gradient-projection optimization is detailed in the following.

The expression of the gradient and the line search parameter for the functional $\Phi\left(\mathcal{W}^{(1)}, \dots, \mathcal{W}^{(P)}\right)$, defined in (2.14), within a conjugate gradient scheme is analytically derived following the approach in [*Isernia et al.*, 1997]. The gradient of the penalty term Φ respect to $\mathcal{W}^{(p)}$ is computed by using the following definition:

$$\Delta\Phi_{\mathcal{W}^{(p)}} = \langle \nabla\Phi_{\mathcal{W}^{(p)}}, \Delta\mathcal{W}^{(p)} \rangle \tag{2.15}$$

where $\langle\cdot,\cdot\rangle$ denotes the scalar product and $\Delta\Phi_{\mathcal{W}^{(P)}}$ is the variation of Φ^P due to an increment of $\mathcal{W}^{(p)}$. Then by considering the expression of Φ, it follows that:

$$\Delta\Phi_{\mathcal{W}^{(p)}} = \tau_p \langle \frac{\partial \mathcal{W}^{(p)}}{\partial \phi_p}, \frac{\partial \Delta\mathcal{W}^{(p)}}{\partial \phi_p} \rangle + c.c.$$

(2.16)

where $c.c.$ stands for the conjugate of the first addendum. By taking into account the properties of the involved differential operator [*Kantorovich and Alkilov*, 1977], the eq. (2.16) can be rewritten as:

$$\Delta\Phi_{\mathcal{W}^{(p)}} = \tau_p \langle -\frac{\partial^2 \mathcal{W}^{(p)}}{\partial {\phi_p}^2}, \Delta\mathcal{W}^{(p)} \rangle + c.c.$$

(2.17)

Then, by comparing eq. (2.15) and (2.17) it follows:

$$\nabla\Phi_{\mathcal{W}^{(p)}} = -2\tau_p \frac{\partial^2 \mathcal{W}^{(p)}}{\partial {\phi_p}^2}$$

(2.18)

To obtain the line search parameter, let us consider the behavior of the functional (2.14) along an arbitrary line whose direction is given by $\mathcal{W}^{(p)} + \lambda\Delta\mathcal{W}^{(p)}$ so that:

$$\Phi\left[\mathcal{W}^{(p)} + \lambda\Delta\mathcal{W}^{(p)}\right] = \sum_{p=1}^{P} \tau_p \langle \frac{\partial \mathcal{W}^{(p)}}{\partial \phi_p} + \lambda \frac{\partial \Delta\mathcal{W}^{(p)}}{\partial \phi_p}, \frac{\partial \mathcal{W}^{(p)}}{\partial \phi_p} + \lambda \frac{\partial \Delta\mathcal{W}^{(p)}}{\partial \phi_p} \rangle$$

(2.19)

Due to the nature of the involved operator, eq. (2.19) can be rewritten as a second degree algebraic polynomial, i.e.:

$$f(\lambda) = c_2\lambda^2 + c_1\lambda + c_0$$

(2.20)

wherein:

$$c_2 = \sum_{p=1}^{P} \tau_p \left\| \frac{\partial \Delta W^{(p)}}{\partial \phi_p} \right\|_{\Omega}^2$$

$$c_1 = 2\mathcal{R}e \sum_{p=1}^{P} \tau_p \left\langle \frac{\partial W^{(p)}}{\partial \phi_p}, \frac{\partial \Delta W^{(p)}}{\partial \phi_p} \right\rangle$$

$$c_0 = \sum_{p=1}^{P} \tau_p \left\| \frac{\partial W^{(p)}}{\partial \phi_p} \right\|_{\Omega}^2$$

Note that both (2.18) and (2.20) the circular neighborhood $\mathcal{I}_{R_p}(\boldsymbol{r_p})$, as defined in (2.14), acts to take into account the localized nature of the regularizing penalty term.

A. On the choice of τ_p *and* R_p

To set the parameters appearing in the inversion procedure (the pivot points r_p, the weight τ_p, and radius R_p), one takes advantage of the fact that our design equation (1.8) also provides an estimate of the unknown targets' support simply obtained by plotting the norm of the solution over the ROI. In particular, the normalized indicator function defined in (1.10) is used. About the choice of the pivot points r_p, see the guidelines given in the Section 1.5.

To select the suitable radius R_p of the circular domain $\mathcal{I}_{R_p}$, it is worth recalling that the contrast source must have the same support Σ as the scatterer [*Catapano et al.*, 2007b, *Crocco et al.*, 2013]. Hence, the maximum allowed value for the radius R_p will be ruled by the distance between r_p and the estimated boundary of the scatterer. Note this means that circular domain of different radius (and extent) will be adopted for the different pivot points, depending on the distance from the boundary. In particular, the closer the pivot point to the (estimated) borders of the scatter, the smaller the radius of the corresponding $\mathcal{I}_{R_p}$.

Similar arguments can be exploited for the choice of τ_p. In particular, since the contrast source's support is constrained onto Σ, it is expected that

the induced current for r_p close to the estimated boundary will not show an exact circular symmetry with respect to r_p [*Catapano et al.*, 2007b, *Crocco et al.*, 2013]. This physical observation corresponds to what is foreseen by LSM theory, according to which the energy of the solution $\|\alpha_P\|_\Gamma^2$ blows up when r_p approaches the boundary of the scatterer [*Colton et al.*, 2003]. Accordingly, an automatic way to select τ_p is devised by relying on the LSM indicator. In particular, τ_p is set equal to the value obtained by normalized indicator function defined in (1.10) in the relevant r_p. Note this allows to set values of τ_p in the range]0, 1].

2.2.3 Method's assessment

In this subsection an assessment of the proposed regularized method is given. In particular, a ring-shaped scatterer which is known to be critical for the LSM [*Catapano et al.*, 2007b, *Crocco et al.*, 2013] is considered.

To deal with such a case, the simulated data are corrupted with a random Gaussian noise with $SNR = 15dB$. The filamentary currents used as transmitting and receiving probes are evenly displaced in angle on a circumference of radius $R = 3.3\,\lambda$, the background medium is vacuum, and the number of probes is fixed equal to $M = N = 21$ according to [*Bucci and Isernia*, 1997]. The considered lossy dielectric ring is shown in figs. 2.4(a)-(b). The parameters for this example are $\varepsilon = 2.5, \sigma = 0.025, N_c = 64 \times 64$.

Due to the multiple connection of the support and the circular symmetry of the contrast profile, the LSM fails in retrieving the actual shape, but it can provide an image of the target's convex hull [*Cakoni and Colton*, 2006, *Catapano et al.*, 2007b, *Crocco et al.*, 2013], as indeed shown in fig. 2.4(c). As a consequence, many of the selected pivot points do not lie within the actual target support. With respect to these points, the radius R_p, see figs. 2.4(d)-(f), is set equal to $\lambda/2$, $\lambda/3$, and $\lambda/6$, respectively.

It is interesting to note that the final achieved result correctly guesses both the actual target's shape and its permittivity (see figs. 2.4(g)-(h)) and corresponds to an MSE of 21%.

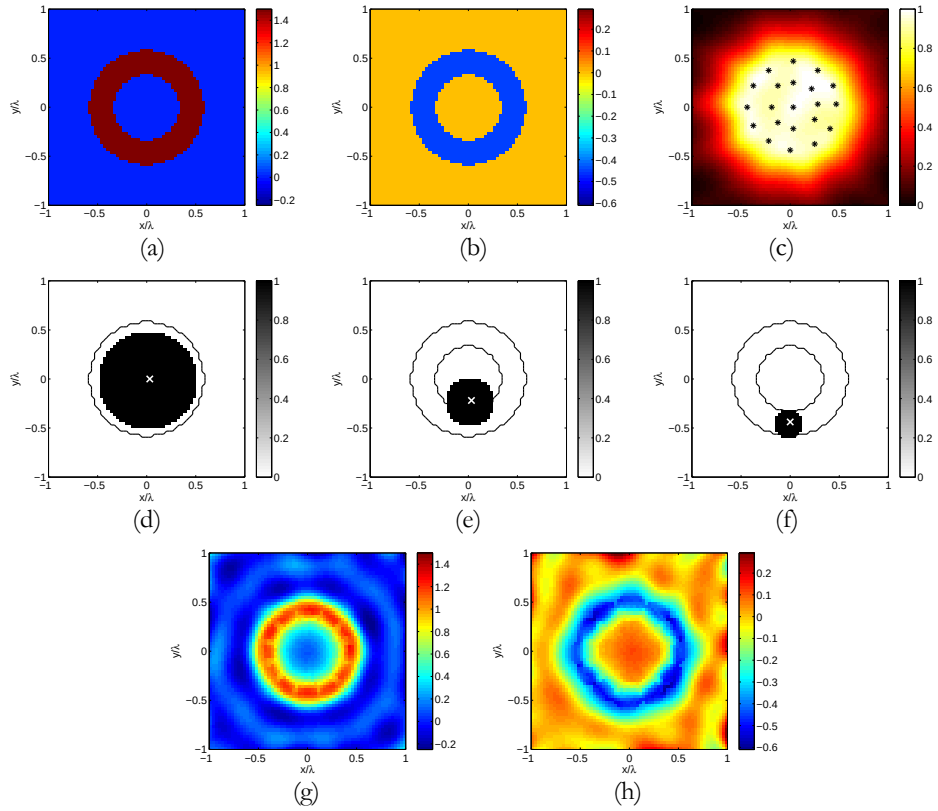

Figure 2.4. Numerical assessment of RCSI. The ring-shaped scatterer. (a) Real part and (b) imaginary part of the contrast profile; (c) Normalized logarithmic LSM indicator map with the selected pivot points superimposed as dots; (d) visual sketch of the circular region $\mathcal{I}_{R_p}$ for the innermost pivot point with a contour plot of the actual scatterer support; (e) same as (d), but for the inner pivots; (f) same as (d), but for the outermost pivot points; (g) real part and (h) imaginary part of the retrieved contrast.

Such a result is only in apparent contradiction with the map in fig. 2.4(c). In fact, it has to be stressed that, differently from the standard theory of LSM, (where eq.(1.8) is used to appraise the shape) in our case eq. (1.8) is just used to enforce a circular symmetry of the contrast source. As a consequence, differently from DARE approach, in the present case the pivot points do not need to belong to the actual scatterer support. Rather, it is sufficient to have an estimation of the target's convex hull and that VE are able to enforce some circularly symmetric contrast source around each of the selected pivot points.

2.3 A distorted iterated virtual experiments method

As briefly discussed in the Section I.4, in literature different strategies exist to counteract the non-linearity of inverse scattering problem. Among them, the standard DBIM, originally proposed by Chew and Wang [*Chew and Wang*, 1990], overcomes this difficulty by considering a series of intermediate linearizations based on DBA [*Devaney and Oristaglio*, 1983]. The outline of this approach can be summarized in the following steps:

a) solution of the inverse scattering problem for a first estimation of the contrast function by using the BA where the homogeneous Green's function is considered;
b) solution of the forward problem and computation of the Green's function in the investigated domain and at the observation points, considering the last estimated contrast function as reference scenario;
c) updating of the data equation by substituting the field and the Green's function calculated at step b), and solution of the inverse scattering problem by DBA to refine the profile distribution;
d) return to step (b) and comparison the field obtained by the last reconstructed distribution function and the measured data. If the difference is less than a set threshold or is larger than the difference at the previous iteration, the procedure terminates, otherwise the cycle is repeated until the solution is convergent.

Note that at each iteration DBIM involves the solution of a forward problem to update the background field as well as the Green's function. In general, the final outcome of the procedure depends on the starting point, obtained by considering BA, i.e. $E = E_i$, as well as on the validity of the intermediate linearizations based on DBA.

As recalled in the Section 1.6.1, recently, a new linear approximation, which relies on the emerging framework of the VE, has been introduced. In particular, in [*Di Donato et al.,* 2015a] a quantitative criterion to foresee the method's applicability is derived to show the effectiveness of the method in

imaging non-weak targets and in outperforming the linearized inversion method based on the standard BA approximation. On the other hand, its limitations, with respect to target with increasing values of the refractive index and electrical dimensions of the scatterer, are highlighted.

In order to further extend the validity of the considered linear approximation, a further possibility offered by scattering conditioning enforced by means of the VE framework is introduced and discussed in this Section. In particular, inspired by DBIM, an iterative method is proposed, wherein, besides updating the Green's function, each iteration involves the design of new ad hoc VE, the recasting of the problem in terms of these latter and its solution by means of VE based linear approximation. Notably, this procedure takes into account the nature of the scatterer from the first step and at each step. Therefore, this new iterative method is expected to outperform the standard DBIM.

2.3.1 New iterated scheme

In the same spirit of DBIM, the proposed iterative procedure, called Distorted Iterated Virtual Experiments method (DIVE), involves successive linearizations, but each linearization is based on properly designed VE. Each new design of the VE implies a new conditioning of the scattering phenomena. DIVE procedure can be summarized in five steps, as follows.

1) *Initialization:* a first estimation χ^0 of the contrast function is done by using the linear approximation recalled in Section 1.6.1, where the homogeneous Green's function is used[3].

2) *Forward Scattering Solution, calculation of Green's function*: the forward scattering problem pertaining to the last reconstructed object χ^k is solved in order to update the background field $E_b{}^k$, that is the total field arising in χ^k, and the anomalous field $\Delta E_s{}^k$, that is the difference between E_s and the field

[3] Note that on the basis of a priori information the proposed iterative procedure could consider other more favorable starting guesses.

scattered by χ^k Next, the Green's function ${G_b}^k$ with χ^k as the background permittivity is numerically computed by exploiting the reciprocity theorem.

3) Convergence control: in order to check the convergence of the iterative algorithm, a stopping rule is considered by defining the relative residual error (RRE) at k^{th} iteration as $RRE^k = \left\|\Delta {E_s}^k\right\|_2 / \|E_s\|_2$. If RRE^k is less than a set threshold (10^{-5}) or is larger than the RRE^{k-1}, the procedure terminates and the solution of the underlying problem is represented by χ^k. Otherwise, the iterative procedure continues until stopping criterion is fulfilled.

4) Identification of the contrast perturbations and new design of virtual experiments: in order to localize and identify possible perturbations and corrections $\Delta\chi^k$ respect to the last reconstructed profile χ^k, the Distorted Linear Sampling Method (LSM) is exploited and the relevant FFE is solved in case of partially known scenario, i.e.:

$$\sum_{v=1}^{N} {\alpha_v}^k(\boldsymbol{r_p})\, \Delta {E_s}^k(\vartheta_v, \boldsymbol{r}) = {G_b}^k(\boldsymbol{r}, \boldsymbol{r_p}), \quad \boldsymbol{r} \in \Gamma \tag{2.21}$$

wherein ${\alpha_v}^k$ are the unknown coefficients computed at k^{th} iteration required to implement the k^{th} set of VE. As discussed in Chapter 1, the energy of the coefficients ${\alpha_v}^k$ provides an estimation of the shape of $\Delta\chi^k$. In particular, the support indicator Υ^k normalized over the sampling grid is defined as:

$$\Upsilon^k(\boldsymbol{r_p}) = \frac{log_{10}\|{\alpha_v}^k\| - log_{10}\|{\alpha_v}^k\|_{max}}{min(log_{10}\|{\alpha_v}^k\| - log_{10}\|{\alpha_v}^k\|_{max})} \tag{2.22}$$

Then, the pivot points r_p belonging to the estimated anomaly support are selected and finally the VE are built.

5) Solution of the distorted virtual scattering problem and update of the solution:

The relevant data equation (1.2) is reformulated in case of partially known scenario and recast in term of VE as follows:

$$\Delta\mathcal{E}_s{}^k(\boldsymbol{r},\boldsymbol{r_p}) = \int_{\Omega} G_b{}^k(\boldsymbol{r},\boldsymbol{r}')\,\Delta\chi^k(\boldsymbol{r})\mathcal{E}^k(\boldsymbol{r}',\boldsymbol{r_p})d\boldsymbol{r}' = \mathcal{A}_e[\Delta\chi^k\mathcal{E}^k] \tag{2.23}$$

where $\Delta\mathcal{E}_s{}^k$ and $\mathcal{E}^k$ are the anomalous and total fields arising in the VE, respectively. Unlike the DBIM, the total field $\mathcal{E}^k$ in equation (2.23) is not approximated by considering only the background field, but also by taking into account the contribution of the anomaly by means of the field approximation introduced in Section 1.6.1.

After solving the distorted linear inverse problem, a new profile is generated by adding the reconstructed corrections to the current reference scenario, i.e. $\chi^{k+1} = \chi^k + \Delta\chi^k$.

6) Return to step 2. The iteration continues until the stopping criterion is fulfilled.

The proposed imaging scheme is shown in the flowchart of fig. 2.5.

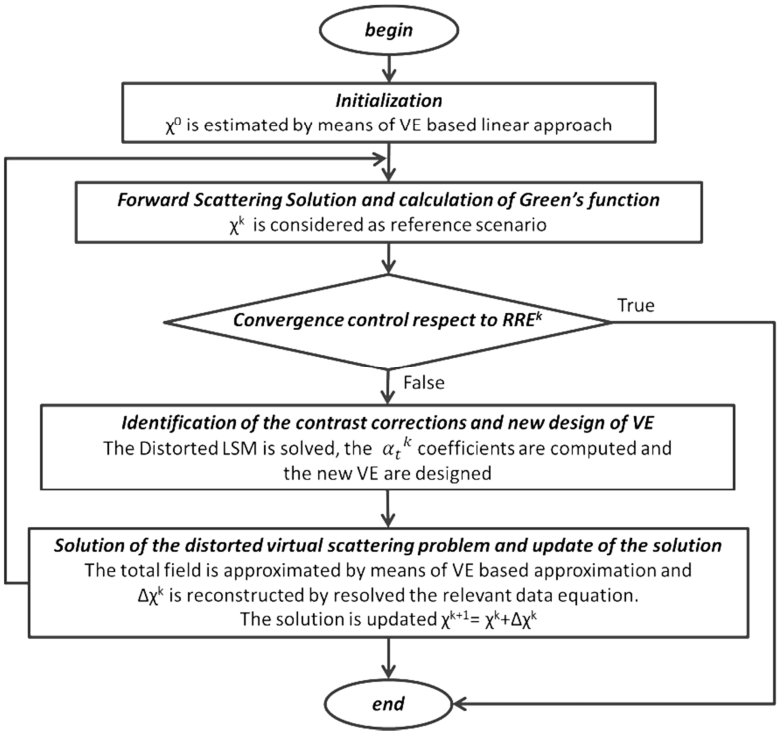

Figure 2.5 The Flowchart describing the DIVE method.

Both in step 1) and 5), a regularized solution of an ill-posed problem is sought. For this purpose, in this section the well-known Truncated Singular Value Decomposition (TSVD) [*Bertero and Boccacci,* 1998] is used. The truncation index N_T, which represents the regularization parameter of this inversion scheme, is determined by exploiting the Picard plot technique [*Hansen*, 1990, *Hansen and O'Leary*, 1993], in particular by identifying the index of the singular value corresponding to a change of slope, related to the transition from a solution dominated by regularization error to the one dominated by the noise error.

2.3.2 Method's assessment

The results in [*Crocco et al.*, 2012a] show that the linear inversion method recalled in Section 1.6.1 has a limit for its applicability in the case of objects with $|k_m|d > 7.70$, being k_m and d the wavenumber and diameter of the homogeneous lossy scatterer, respectively.

In this Section, in order to demonstrate the capability of the new iterative method to extend and outperform the linear method in [*Crocco et al.*, 2012a], the kite scatterer, similar to the one analyzed in [*Di Donato et al.,* 2015a], is considered. In particular, the leading dimension of the kite is λ, while the permittivity and the conductivity are, respectively, equal to 2 and 0.1 S/m.

The target is positioned inside a square domain of side $\mathrm{L} = 2.16\,\lambda$ discretized in $N_c = 42 \times 42$ cells (see fig 2.6(a)-(b)). Moreover, a number of receivers and transmitters equal to 24, both located on a circumference Γ of radius $\mathrm{R} = 1.66\,\lambda$, is considered. The scattered field data are corrupted with a random Gaussian noise with $\mathrm{SNR} = 25$ dB.

In figs. 2.6(e)-(h) the LSM indicator Υ^k for $k = 0$ and $k = 1$ are shown. As it can be seen in fig 2.6(e), at the first step the LSM is able to identify the support of the target and the pivot points are selected inside it, thus allowing the design of the VE. Nevertheless, the linear approximation does not work fine, as witnessed by figs. 2.6(c)-(d). For $k = 1$, the new design

of VE is realized on the basis of the new LSM map in fig 2.6(h), which allows to identify the support of the searched variation $\Delta\chi^1$. By iterating the design of VE, the proposed method in conjunction with TSVD is able to progressively correct the first reconstruction χ^0 and finally obtain a satisfactory and quantitative reconstruction with err=20% after a number of iterations equal to 13 (see figs 2.6(f)-(g)). During the iterative procedure N_T = [90, 81, 105, 86, 113, 78, 109, 89, 73, 84, 109, 88, 64].

For the sake of comparison, the same analysis is performed by using the DBIM (see figs. 2.6(i)-(j)), achieving an unsatisfactory retrieved profile corresponding to err=115%. In particular, the truncation indices N_T is set equal to the index of the first singular value whose magnitude is 15 dB below that of the leading one.

For more details on the number of iterations, *err* and RRE see Table I and figs. 2.6(k)-(l).

	err (k=0)	***err***	***RRE***	***# iterations***
DBIM-TSVD	0.90	1.15	0.12	3
DIVE-TSVD	0.77	0.20	0.01	13

Table I. Numerical assessment of DIVE. The kite target: details of the inversion procedures.

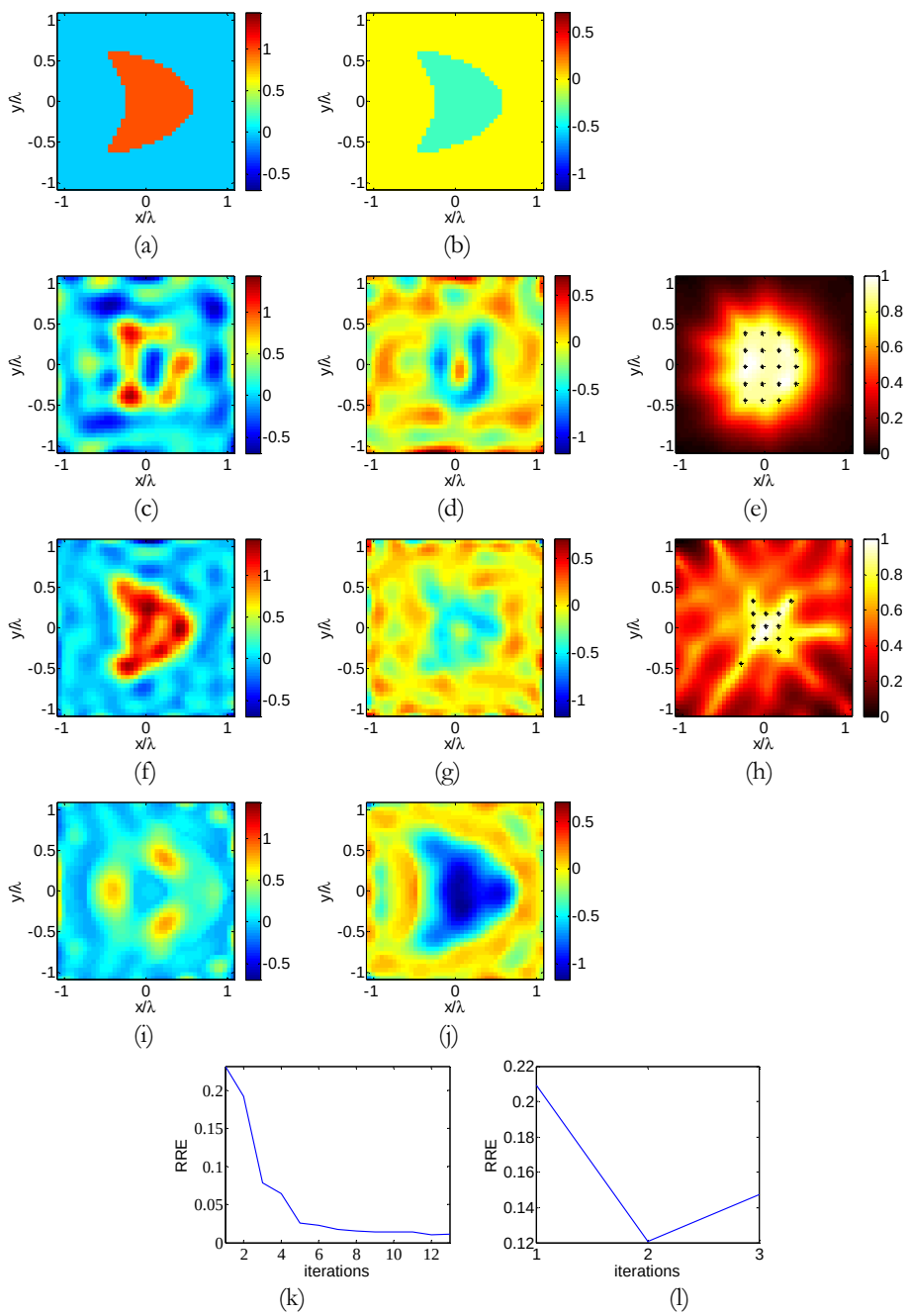

Figure 2.6. Numerical assessment of DIVE. The kite target: (a) real part and (b) imaginary part of the reference profile. LSM indicator maps with the selected pivot points superimposed on it, for k=0 (e) and k=1 (h). Real part and imaginary part of the initial estimation (c)-(d) and of the final reconstruction (f)-(g). Real part and imaginary part of the retrieved contrast function with DBIM (i)-(j). The RRE versus iterations respectively for DIVE (k) and DBIM (l), respectively.

2.4 Assessments against experimental and single frequency data

In this Section the three proposed methods are assessed against the Institute Fresnel experimental data [*Belkebir and Saillard*, 2001, *Belkebir and Saillard*, 2005], which are usually adopted to benchmark inverse scattering procedures.

As compared with the previous examples using simulated data, the Fresnel experiments introduce the additional difficulty of dealing with a partially aspect limited configuration. As a matter of fact, Fresnel targets are probed by primary sources that completely surround them, but, for each source position, the fields are measured by moving the receiving probe along a 240° arc, excluding the 120° degree angular sector centered on the incidence direction of the source [*Belkebir and Saillard*, 2001, *Belkebir and Saillard*, 2005]. In particular, both the targets of the 2001 and 2005 Fresnel dataset are considered, in particular:

- the *TwinDielTM* target [*Belkebir and Saillard*, 2001], which consists of two identical dielectric cylinders of radius 1.5 cm and relative permittivity 3 ± 0.3;
- the *FoamDielIntTM* target [*Belkebir and Saillard*, 2005], which is a piecewise inhomogeneous dielectric target made by two nested, non-concentric, circular cylinders, a high contrast inner one ($\varepsilon = 3 \pm 0.3$) and a low contrast outer one ($\varepsilon = 1.45$);
- the *FoamTwinDielTM* target [*Belkebir and Saillard*, 2005], in which a circular cylinder having the same dimensions and features of the high contrast core is placed in contact with the *FoamDielIntTM* target.

The complete description of the targets and the measurement set-up can be found in [*Belkebir and Saillard*, 2001, *Belkebir and Saillard*, 2005].

For the first test bed, $N = 36$ illumination directions and $M = 49$ measurements for each view are considered, for the second one $N = 72$ and $M = 61$, and for the third target $N = 18$ and $M = 241$. As the database provides the incident field only at the receiving locations, the incident fields inside the imaging domain are modeled by means of a multipole expansion

whose coefficients are evaluated trough a least square fitting procedure at the measurement locations (where the measured incident field is available). By taking into account the dimension of the antenna's aperture, such a superposition results in 19 Hankel functions as proposed in [*Crocco and Isernia*, 2001].

Typically, Fresnel data are tackled by using iterative inversion procedures and multiple frequency data (see for instance [*Abubakar et al.*, 2005, *Gilmore et al.*, 2009, *van den Berg et al.*, 2003, *Crocco and Isernia*, 2001, *Crocco et al.*, 2005]). Hence, the capability of successfully handling them with monochromatic data is indeed very significant. For this reason, it is important to underline that the reconstructions reported in the following (and also in the next Chapter) are obtained by using just single frequency data. Moreover, no a priori information on the unknown contrast is enforced through regularization (in particular, no constraint is enforced on the admissible values of permittivity and conductivity) but for the algebraic method in which 'physical feasibility' arguments are necessarily used in order to select the correct root. Note this is a significant difference with respect to several previous contributions, such as for instance [*Abubakar et al.*, 2005, *Gilmore et al.*, 2009].

Tables II-IV summarize the details of the inversion procedures for the three considered targets, i.e., the adopted frequency, the size of the imaging domain, which is a square of side L, the actual size of the data matrix processed in the design step. In fact, to build the VE and cast the corresponding scattering equations for each target, the multiview-multistatic data matrix is obtained by means of an under sampling of the original data in which the unavailable entries are replaced with zeros.

The inversion procedure for each method is the same outlined in the previous Sections. In particular, for the RCSI method, the radii R_p in terms of the background wavelength are selected according to Section 2.2.2 equal to:

- $\lambda/2$, $\lambda/3$ and $\lambda/8$, for innermost, inner and outermost points, respectively, in the *TwinDielTM* target;
- $\lambda/3$, $\lambda/5$ and $\lambda/10$, for innermost, inner and outermost points, respectively, in the *FoamDielTM* target;

- $\lambda/2$, $\lambda/4$ and $\lambda/8$, for innermost, inner and outermost points, respectively, in the *FoamTwinDielTM* target.

Moreover, during the iterative procedure of DIVE the truncation indices N_T are set equal to:

- N_T = [140, 117, 90, 148, 106, 91, 126, 115, 154, 122, 131, 142] for the *TwinDielTM* target;
- N_T = [47, 55, 36, 51, 40, 47, 35, 46, 51, 55] for the *FoamDielTM* target;
- N_T = [86, 86, 73, 96, 72, 50, 74, 34, 67, 68, 83, 69, 48] for the *FoamTwinDielTM* target.

As it can be observed in the figures 2.7-2.9, the dielectric permittivity values of the different targets are accurately and quantitatively retrieved by means of all the three methods. By comparing the different reconstructions, one must take into account the following considerations.

- DARE approach is able to give back better imaging results in term of shape of the targets, as they are different from zero only inside the estimated target support, which is implicitly assumed as a priori information. In fact, for each pivot point the local value of the contrast is reconstructed and, so, the inversion is localized, while in RCSI and DIVE the reconstruction concerns the entire ROI.
- No a priori information on the target's nature is enforced when DIVE and RCSI are exploited, and no regularization is enforced on the contrast function in RCSI.
- Opposite to DARE which involves an inversion procedure very fast (only few minutes), DIVE and RCSI are iterative and, so, they require a much larger computational burden (up to a thirty minutes).

In particular, concerning the *TwinDielInt* (see fig. 2.7), both DARE and RCSI are able to retrieve accurately the shape of the two cylinders, opposite to DIVE which, nevertheless, starting form a completely wrong first estimation χ^0, see fig. 2.7(f)-(g), is able at the end to successful retrieved the two cylinders. On the other hand, the permittivity is better envisaged by

means of DARE and DIVE, while RCSI slightly underestimates the real part of the contrast profile.

The *FoamDielInt* target represents an extremely challenging case for DARE approach, as the contrast profile exhibits an abrupt discontinuity of the electromagnetic features, thus violating the assumption underlying the approximation introduced in Section 2.1.1. As it can be seen, despite the above mentioned difficulties, DARE method is still able to successfully image the unknown target, although overestimates in dimension the inner cylinder, with respect to RCSI and DIVE. This is probably due to the adopted linear interpolation (see fig. 2.8). Note in this example, in order to better emphasize the different feature of the three methods, the retrieved profiles are shown in different color scales.

Finally, the *TwinFoamDielInt* data set is processed by consider only DIVE and RICS, in order to compare the two iterative methods. As it can be observed in fig. 2.9, the DIVE method slightly overestimates the electromagnetic properties of the targets and underestimates the dimension of the outer cylinder, if compared with the RCSI. This is probably due to the contrast regularization exploited in order to solve the underlying ill-posed linear problem. As it will be shown in the next Chapter, another kind of contrast regularization can improve the performance of the DIVE method.

In conclusion, the three proposed methods are viable for a large class of targets. In particular, the results obtained by processing Fresnel experimental data have shown that the new proposed approaches are actually capable, by only using monochromatic data, of successfully imaging targets which have been so far processed in the literature taking advantage of frequency diversity and/or enforcing some priori information on the target.

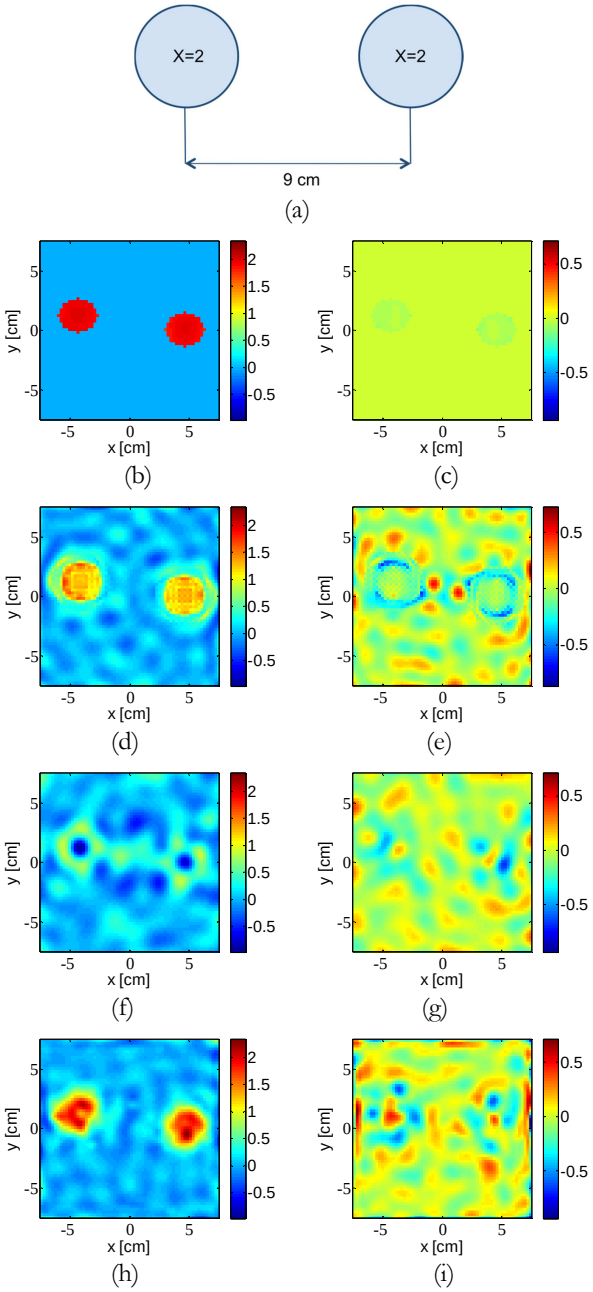

Figure 2.7. Validation of VE based methods with the Fresnel *TwinDielTM* target data: (a) Reference profile. Real part and imaginary part of the retrieved contrast function with DARE (b)-(c), RCSI (d)-(e) and DIVE (f)-(i). In particular (f)-(g) is the initial estimation and (h)-(i) is the final reconstruction.

	***Frequency*[GHz]**	$l_D[cm]$	***data matrix*** $[M \times N]$
VE-DARE	6	15	72x36
VE-RCSI	6	15	72x36
DIVE-TSVD	6	15	72x36

Table II. The Fresnel *TwinDielTM* target: details of the inversion procedures.

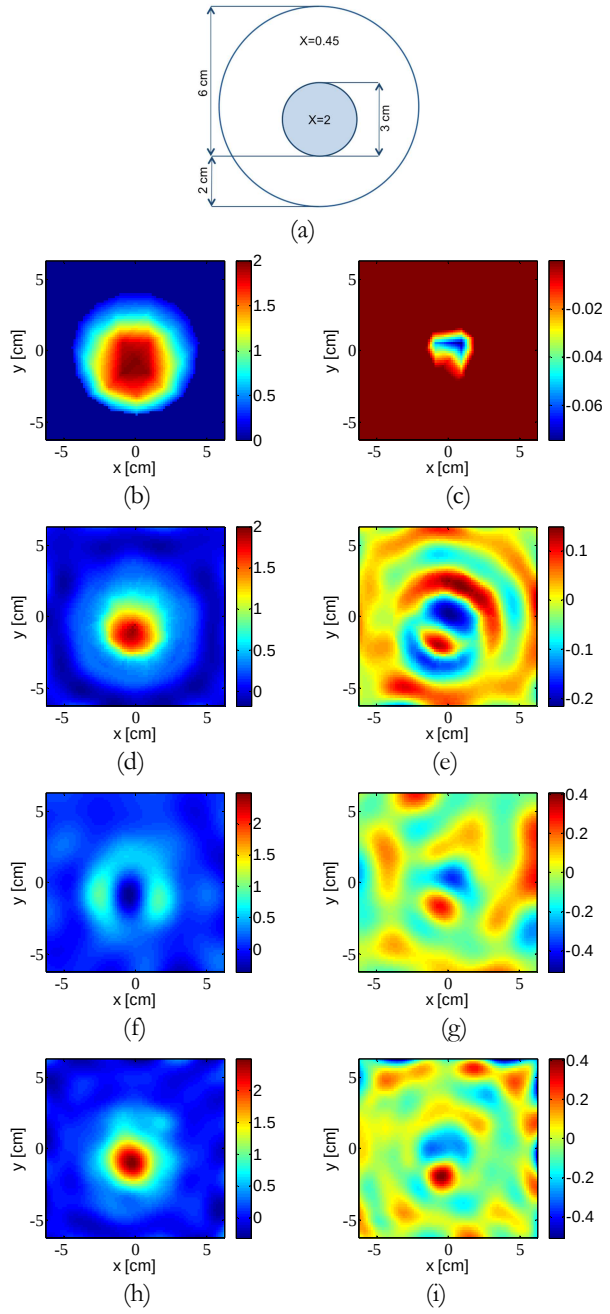

Figure 2.8. Validation of VE based methods with the Fresnel *FoamDielIntTM* target data: (a) Reference profile. Real part and imaginary part of the retrieved contrast function with DARE (b)-(c), RCSI (d)-(e) and DIVE (f)-(i). In particular (f)-(g) is the initial estimation and (h)-(i) is the final reconstruction.

	***Frequency*[GHz]**	$l_D[cm]$	***data matrix*** $[M \times N]$
VE-DARE	4	12.5	45x36
VE-RCSI	4	12.5	45x36
DIVE	4	12.5	23x18

Table III. The Fresnel *FoamDielIntTM* target: details of the inversion procedures.

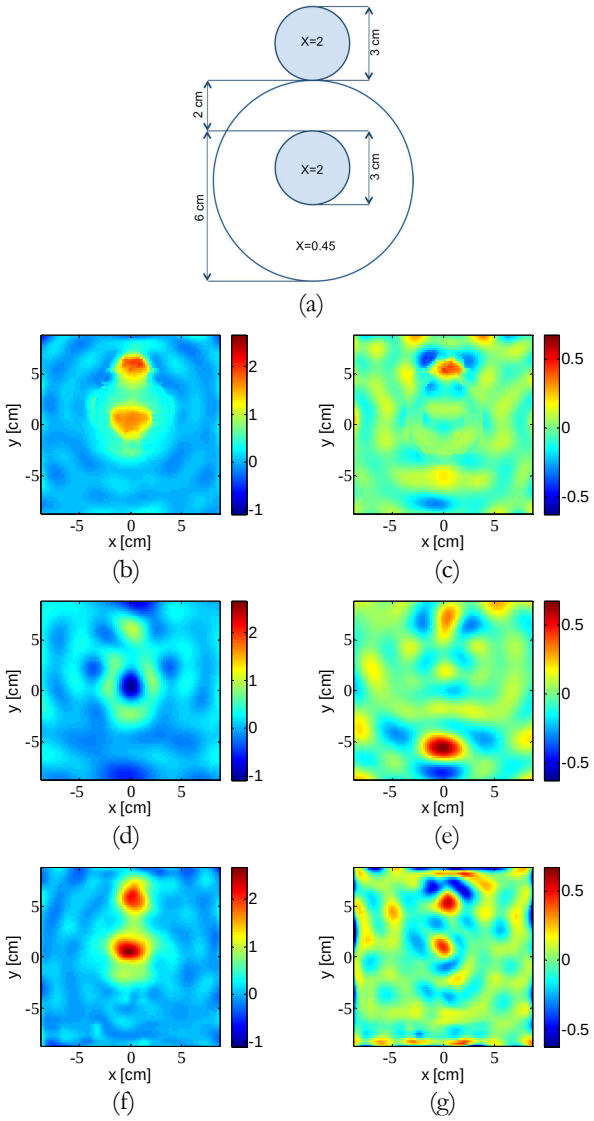

Figure 2.9. Validation of VE based methods with the Fresnel *FoamTwinDielIntTM* target data: (a) Reference profile. Real part and imaginary part of the retrieved contrast function with RCSI (b)-(c) and DIVE (d)-(g). In particular (d)-(e) is the initial estimation and (f)-(g) is the final reconstruction.

	***Frequency* [GHz]**	l_D $[cm]$	***data matrix*** $[M \times N]$
VE-DARE	4	17.5	45x18
VE-RCSI	4	17.5	45x18

Table IV. The Fresnel *FoamTwinDielIntTM* target: details of the inversion procedures.

2.5 Future extensions

The inversion procedures proposed in this Chapter are just some of the many possibilities offered by the framework of VE. As a consequence, the question arises of how it is possible to further improve the introduced approaches and develop new and even more performing approaches.

First of all, the applicability of the three methods is limited by the range of validity of the design step, i.e. the LSM. As a consequence, one can exploit the improvements that have been recently achieved in the capability of estimating the shape of the unknown targets [*Crocco et al.*, 2013], as well as the possibility of improving the focusing achieved via LSM by resorting to an ex-post constrained convex optimization [*Crocco et al.*, 2012c] or considering other focusing procedures.

Second, future developments will aim at extending the methods, or better at exploiting their underlying concepts, in the more challenging 2D and 3D vectorial scenario, where the brought advantages would become even more important.

Third, one can exploit the new methods in conjunction with other inversion methods.

In particular, an interesting aspect for DARE is the chance of considering hybridizations with the 'classic' iterative inversion methods based on local optimization, by using the obtained results to build a very convenient starting point, thus allowing to avoid the occurrence of false solutions. On the other hand, the application of a local optimization technique starting from the algebraic method solution could provide a further refinement of the solution especially when the algebraic method does not work under its ideal conditions (i.e., smoothly varying contrast function).

Concerning RCSI, if the problem has an elevate degree of non-linearity, so the contrast function assumes very large values and/or the dimensions of the scattering system increases, the penalty term inducing the research of circularly symmetric currents could be not able to reduce as much as possible the occurrence of false solutions. In these cases, an interesting possibility would be to test the performances of the technique in conjunction with

regularization technique acting on the contrast function. Better robustness and further improvements of the achievable results and reconstruction capabilities are indeed expected, similar to what has been recently observed when exploiting SOM in conjunction with Multiplicative Regularization (MR) [*Song et al.*, 2015].

Also for DIVE inversion unsatisfactory performances are observed when the contrast function becomes too large or the profile too complex, as in case of breast phantoms. This trouble could be solved by collecting more data, for instance multi frequency data. In this direction, one could develop DIVE method in conjunction with frequency hopping techniques.

Fourth, further possibilities amount to develop other performing approaches by adopting some convenient and useful representation for the fields or the contrast sources, resembling the expected properties of the auxiliary unknowns enforced by the exploited conditioning.

Finally, future work will also aim at building VE which try to enforce other properties rather than the circular symmetry on the scattered field or induced currents. For example, other kind of VE can be achieved by considering multipolar order terms in the solution of the LSM equation [*Crocco et al.*, 2013]. Alternatively, the idea of recombining the total fields in order to obtain a constant virtual field could emphasize the contrast discontinuities which can be for instance useful for their identification inside unknown obstacles.

3
Sparsity promoting methods for inverse scattering

Introduction

In the last years, compressive sensing (CS) has emerged as an increasingly relevant paradigm in signal processing and recovery community, as witnessed by the very large number of papers being published on the subject, and by the thousands of citations of the two basic papers [*Donoho*, 2006, *Candès et al.,* 2006] originating the area. As a matter of fact, part of the success of the CS paradigm comes from statements such as 'the possibility of overcoming the Nyquist criterion' or to achieve 'super-resolution' in a number of recovery (and imaging) problems.

To provide these remarkable outcomes, CS exploits the concept of *sparsity*, where a signal is said to be sparse in a given basis, if it can be exactly represented by means of a few non-zero elements (whose indices are however unknown). A related concept is *compressibility* [*Donoho*, 2006]. A signal is compressible in a given basis if the magnitudes of the sorted coefficients observe power law decay. The faster is the magnitudes decay and more the signal is compressible. Roughly speaking, this implies that by using a sufficiently large number of non-zero coefficients the signal can be safely approximated without any significant information loss. Note a signal which is compressible to a dimension S is nothing but a S sparse signal plus some component outside of the different $\mathbb{R}^S$ subspaces. Notably, in both cases of sparse and compressible signals one does not know a priori which elements of the representation are different from zero.

Provided the proper expansion is used in order to guarantee a sparse or compressible representation of the unknown function, CS theory guarantees that an accurate retrieval of the unknown is possible even for a number of

data much lower than the overall number of basis coefficient, but sufficiently larger than the number of nonzero elements.

In inverse scattering problems, it is commonplace that the number of independent data is much less than the original number of unknowns, and one has to tackle this difficulty by relying on additional information about the quantity to be retrieved. As such, the CS paradigm is definitely attractive, as it can both improve the accuracy of existing inversion procedures and/or drive the design of simpler (and hence cheaper) measurement set-ups than those foreseen in [*Bucci and Isernia*, 1997].

In addition, the sparsity requirement recalled above is actually applicable to most cases dealt with in inverse scattering problems. As a matter of fact, in several applications one can safely assume that not all of the voxels constituting the scenario are independent. This is for instance the case of two of the main fields of exploitation of microwave tomography, i.e., biological or biomedical monitoring and non-invasive inspection of man-made objects. In both cases, one can indeed assume that different homogeneous sub-regions constitute the scenarios. Hence, few parameters (with respect to the number of voxels in which discretize the ROI) are required for an accurate recovery of the electromagnetic properties profile, so that the sparsity (or compressibility) assumption can be fulfilled, provided proper basis functions (possibly suggested by the application) are used to represent the unknown function.

On the other side, in pursuing possible applications of CS to the area of inverse scattering, one fundamental difficulty comes into play, besides the choice of a convenient representation basis for the specific problem at hand. This is represented by the intrinsic non-linear nature of the electromagnetic inverse scattering problem. In fact, while CS theory is well developed and understood for the case of phenomena described through linear models, in inverse scattering problems the relationship between the unknown and the measurements is usually non-linear, so that a number of theoretical results are still missing.

As a consequence, the exploitation of CS in inverse scattering has been so far restricted to cases where the scatterers are both sparse in space (point-

like) and 'weak', so that the BA can be safely used [*Poli et al.*, 2012, *Ambrosanio and Pascazio.*, 2015]. More recently, the joint exploitation of CS, BA and total variation (TV) has been proposed to image extended targets [*Oliveri et al.*, 2014]. Unfortunately, the range of applicability of this linearized approximation is very limited, and the underlying assumptions are hardly met in the applications, thus strongly limiting the usefulness of these methods. More recent contributions have also investigated the possibility to take advantage from CS under the Rytov approximation [*Oliveri et al.*, 2012], but their validity remains still limited. As a natural extension of the Born approximation, other contributions use sparsity constraint regularization combined with the Distorted Born Iterative Method [*Desmal and Bagci*, 2014, *Azghani et al.*, 2015], which further extends applicability.

In this respect, the first part of this Chapter aims at showing how it is possible to significantly enlarge the range of applicability of CS to inverse scattering problems by relying on the VE framework. In fact, as recalled in Section 1.6.1, by means of a proper pre-processing and re-arranging of the scattering experiments, it is possible to introduce a new effective field approximation which goes well beyond the range of validity of usual weak scattering approximations.

Moreover, to move towards the effective CS-based procedures in general inverse scattering problems, two possible applications of CS to fully non linear inverse scattering problems are also introduced and discussed. In particular, the applicability of CS is first explored within the CSI scheme [*van den Berg and Kleinman*, 1997], which represents a very popular and effective reconstruction algorithms for inverse scattering.

Successively, in the same spirit as for DBIM, iterated linearizations (based on the VE framework) of the scattering equation are considered, so that CS can be safely applied in each iteration.

3.1 The compressive sensing theory for an effective recovery

Let us recall the basics of CS, considering a generic linear problem:

$$\boldsymbol{y} = \boldsymbol{A}\boldsymbol{x} \tag{3.1}$$

where $\boldsymbol{y}$ is the $N_y \times 1$ data vector, $\boldsymbol{x}$ is the $N_x \times 1$ vector that represents the unknown function, and $\boldsymbol{A}$ is the $N_y \times N_x$ matrix which relates the unknown vector to the data vector[4].

Let us now suppose to adopt some convenient basis functions, so that the representation coefficients are sparse (i.e. only few coefficients are different from zero). In such situation, it is convenient to rewrite the linear problem as:

$$\boldsymbol{y} = \boldsymbol{A}\boldsymbol{\Psi}\boldsymbol{s} = \boldsymbol{\Theta}\boldsymbol{s} \tag{3.2}$$

where $\boldsymbol{\Psi}$ is an $N_x \times N_x$ matrix having the basis function as columns and $\boldsymbol{s}$ is the vector that contains the unknown coefficients of the representation. Notably, $\boldsymbol{\chi} = \boldsymbol{\Psi}\boldsymbol{s}$ and also $\boldsymbol{s} = \boldsymbol{\Psi}^{\boldsymbol{T}}\boldsymbol{\chi}$. Finally, $\boldsymbol{\Theta}$ denotes the product of $\boldsymbol{A}$ times $\boldsymbol{\Psi}$.

According to CS theory, by taking advantage from the sparsity of the unknown coefficients $\boldsymbol{s}$, it is possible to solve the inverse problem even if N_y is (much) less than N_x , but it is anyway sufficiently larger than the number S of coefficients different from zero (with $S < N_y < N_x$). In particular, the correct number of measurements N_y, necessary to obtain a faithful solution, is lower-bounded and has to satisfy the inequality $N_y \geq N_y'$, where N_y' is proportional to S and to $\log N$ [*Donoho*, 2006].

Note the exact reconstruction of a sequence of a S-sparse signal is possible when the number N_y of measurement is sufficiently larger than S, but this result is only true in a probabilistic sense. Numerical analysis of

[4] In literature usually the dimension of the data vector is referred to as M, while the one of the unknown vector is referred to as N.

canonical cases has suggested that a successful reconstruction is achieved in more than 50% of the cases when $N_y \geq 4S$, and in more than 90% of the cases when $N_y \geq 8S$ [*Donoho*, 2006, *Baraniuk*., 2007].

A very relevant non-intuitive circumstance is that it is not just the number of measurements which plays a role, as the kind of measurements which is performed plays a role as well.

Intuitively, the matrix $\boldsymbol{\Theta}$ has to be deeply different from a subset of the identity matrix and should not cancel out any information about the original signal. In particular, the image of the columns of $\boldsymbol{\Psi}$ should be spread out in the domain defined by the rows of $\boldsymbol{A}$. As a matter of the fact, the larger this incoherence, the better the possibility to retrieve sparse signals by compressed measurements.

Moreover, the matrix $\boldsymbol{\Theta}$ should approximately preserve the Euclidean length of *S*-sparse signals, so each *S*-sparse vector cannot be mapped in the null space of $\boldsymbol{\Theta}$, and each *S*-sparse vector has to have a non-negligible image in the space of measurements.

The exact requirements can be formalized by means of the so-called Restricted Isometry Property (RIP) [*Baraniuk*, 2007, *Candès et al.,* 2006], which guarantees conditions for an exact recovery.

Provided the above conditions are fulfilled, it is possible to solve the inverse problem $\boldsymbol{y} = \boldsymbol{Ax}$ by means of the following optimization constrained problem [*Donoho*, 2006, *Baraniuk*, 2007]:

$$\min_{\boldsymbol{s}} \{\|\boldsymbol{s}\|_{\ell_1}\} \quad subject\ to \quad \|\boldsymbol{\Theta s} - \boldsymbol{y}\|_{\ell_2} \leq \delta \tag{3.3}$$

where $\|\cdot\|_{\ell_1}$ is the ℓ_1 norm and δ is a positive parameter which depends on the level of required accuracy, on the level of noise on the data and on the error model.

The problem in (3.3) is known as Basis Pursuit denoising (BPDN) or Least Absolute Shrinkage and Selection Operator (LASSO) problem [*Tibshirani*, 1996]. In eq. (3.3) the minimization of the ℓ_1 norm encourages the search of sparse solutions, while the constraint enforces the data consistency.

In other words, among all solutions which are consistent with the measured data within a given error, one searches the one which is sparsest.

Note that, while the optimization problem should consider indeed the so called ℓ_0 norm [*Baraniuk*, 2007], the relaxation into to ℓ_1-norm adopted in eq. (3.3) reduces the problem to a convex programming one, and it has been shown that the two formulations are equivalent for a very wide range of cases [*Donoho*, 2006, *Candès et al.,* 2006].

For a better understanding and for an original geometrical interpretation of CS theory, the reader is deferred to Appendix E.

3.2 Compressive sensing and linearized inverse scattering

The linearized model introduced in [*Crocco et al.*, 2012a] and recalled in Section 1.6.1 is able to image targets out the range of validity of usual BA [*Di Donato et al.,* 2015a]. As such, this new approximation allows to significantly enlarge the applicability of CS to inverse scattering problems. This new linear approximation is based on the VE framework and allows to recast the discretized version of the data equation (1.2) for different P pivot points, thus achieving a system of linear equations, which can be formally expressed as:

$$\boldsymbol{\mathcal{E}_s} = \boldsymbol{A}\,\boldsymbol{\chi} \tag{3.4}$$

where $\boldsymbol{\mathcal{E}_s}$ is the $(M \times P) \times 1$ data vector which contains the measured scattered field arisen in the VE, $\boldsymbol{\chi}$ is the unknown function of the problem, i.e. the contrast function, organized into an $N_c \times 1$ dimensional vector, and, finally, $\boldsymbol{A} = \boldsymbol{A_e}\boldsymbol{\mathcal{E}}$ is the $(M \times P) \times N_c$ matrix which relates the unknown vector to the data vector. Note $\boldsymbol{A_e}$ is the discretized version of the integral radiation operator $\mathcal{A}_e$ and $\boldsymbol{\mathcal{E}}$ contains the approximated total field arisen in the VE (see eq.(1.12)).

In [*Crocco et al.*, 2012a] the TSVD inversion scheme has been proposed as a way to fix the ill-posedness of the linearized inverse problems (3.4). In

the following, the CS theory is proposed as an alternative to TSVD, thus allowing nearly optimal reconstructions.

3.2.1 CS inspired linear inversion

Once the problem is properly linearized, the choice of a convenient representation basis, which allows to reduce as much as possible the number S of coefficients different from zero is the real key point. Obviously, it is appropriate and convenient to exploit all the available priori information about the kind and nature of the investigated scenario.

In what follows, different possibilities are introduced in order to tackle the imaging of both point-like and extended targets.

A. CS approach for point-like scatterers

In order to solve the inverse scattering problem and retrieve the unknown profile, the investigated domain is usually discretized in a certain number of cells or pixels, according to the value of the used frequency and the expected maximum value of the permittivity and conductivity of the unknown object [*Richmond*, 1965].

In a number of applications one can assume that the unknown targets are small and localized, and hence sparse in the usual pixel based representation. These cases include, but are not limited to, contrast agent aided breast cancer imaging [*Scapaticci et al.*, 2014], intra-wall imaging of large areas [*Ahmad and Amin*, 2013] and differential imaging [*Scapaticci et al.*, 2012a]. In these cases, by considering $\boldsymbol{\Psi}$ equal to the identity matrix, $\boldsymbol{\Theta} = \boldsymbol{A}$ and $\boldsymbol{s} = \boldsymbol{\chi}$, the problem (3.3) can be reformulated as:

$$\min_{\boldsymbol{\chi}} \{\|\boldsymbol{\chi}\|_{\ell_1}\} \quad subject\ to \quad \|\mathbf{A}\boldsymbol{\chi} - \boldsymbol{\mathcal{E}}_s\|_{\ell_2} \leq \delta \tag{3.5}$$

where $\boldsymbol{\chi}$ is the contrast function represented in pixel basis.

B. CS and Wavelets basis for extended scatterers

In a number of cases, reasoning in term of pixels is not a convenient way to solve eq. (3.4) and it is more convenient to use a different basis. Amongst the different possibilities, the multi-resolution wavelet representation [*Mallat*, 1989, *Mallat*, 2008] is particularly attractive, as its capability to faithfully represent complex scenarios with few coefficients has been already demonstrated in many applications [*Antonini et al.*, 1992, *Chang et al.*, 2000, *Li et al.,* 2013, *Scapaticci et al.*, 2012b].

In light of the above reasoning, the problem (3.3) can be rewritten as:

$$\min_{\boldsymbol{s}}\left\{\|\boldsymbol{s}\|_{\ell_1}\right\} \quad subject\ to \quad \|\boldsymbol{AWs}-\boldsymbol{\mathcal{E}_s}\|_{\ell_2}\leq\delta \tag{3.6}$$

where $\boldsymbol{W}$ is the matrix which contains a wavelet basis and $\boldsymbol{s}$ is the vector containing the wavelet coefficients of the contrast function.

C. CS and Total Variation for extended scatterers

When the targets cannot be assumed to be small with respect to the probing wavelength, one may have the a priori information that the contrast profile is piecewise constant, which entails a sparse representation in terms of step functions, or, which is the same, it has a sparse gradient in the usual pixel representation. This happens indeed in a number of cases including non-destructive testing, sub-surface sensing, geophysical probing, as well as a number of biomedical applications. Accordingly, problem (3.4) can be solved by:

$$\min_{\boldsymbol{\chi}}\left\{\|\boldsymbol{D_x\chi}\|_{\ell_1}+\left\|\boldsymbol{D_y\chi}\right\|_{\ell_1}\right\} \ subject\ to \quad \|\mathbf{A}\boldsymbol{\chi}-\boldsymbol{\mathcal{E}_s}\|_{\ell_2}\leq\delta \tag{3.7}$$

where $\boldsymbol{D_x}$ and $\boldsymbol{D_y}$ are the discretized version of the partial derivatives evaluated with respect to the spatial variables x and y, respectively, i.e. the discretized version of the gradient along the coordinate directions. In other words, $\boldsymbol{D_x\chi}$ and $\boldsymbol{D_y\chi}$ are the $N_c\times 1$ vectors containing the forward differences of the unknown function $\boldsymbol{\chi}$ [*Candès et al.*, 2008].

Roughly speaking, the optimization problem now amounts to look for a solution whose gradient has the minimum ℓ_1 norm among all the contrast functions which are consistent, within a given error, with the measured data.

The approach described in (3.7) is able to identify in a simple fashion the target discontinuities along two preferential directions, i.e. the directions parallel to the coordinate axes. Hence, discontinuities having different orientations are not always correctly identified, and the approach provides a kind of 'squared' reconstruction of the target.

In order to counteract, at least in a partial fashion, the orientation dependence of the approach, a new objective function can be considered, which allows also to identify additional discontinuities located at + or – 45° with respect to the coordinate axes. Let define $\boldsymbol{D_d}$ as the discretized version of the directional derivative evaluated along the directions parallel to $x = \pm y$. In other words, $\boldsymbol{D_d\chi}$ is the vector, which contains the forward differences along directions parallel to the principal and secondary diagonal of the matrix of pixels representing the unknown function $\boldsymbol{\chi}$. Accordingly, the eq.(3.7) is recast as:

$$\min_{\chi}\left\{\|\boldsymbol{D_x\chi}\|_{\ell_1} + \left\|\boldsymbol{D_y\chi}\right\|_{\ell_1} + \|\boldsymbol{D_d\chi}\|_{\ell_1}\right\}$$
$$\textbf{subject to} \quad \|\boldsymbol{A\chi} - \boldsymbol{\mathcal{E}_s}\|_{\ell_2} \leq \boldsymbol{\delta} \tag{3.8}$$

The optimization problem now amounts to look for a solution whose gradient evaluated also in the 'oblique' directions, has the minimum ℓ_1 norm among all the contrast functions fulfilling within a given error the data equation.

Along the same lines of reasoning, a 'corner identifier' approach can be introduced for profiles where all discontinuities are parallel to x or y axis. In fact, the vector $\boldsymbol{D_{xy}\chi}$, which contains the discrete value of second mixed partial derivative, will correspond to S number of corners and so much less than the value achieved when using the gradient. For example, a rectangular homogeneous target will imply S=4 independently from its dimensions. As a

consequence, an approach based on such a derivative can identify more easily scatterers constituted by a superposition of squares and rectangles.

When such a kind of qualitative information is available, an accurate quantitative reconstruction can be obtained by solving:

$$\min_{\chi}\left\{\left\|\boldsymbol{D}_{xy}\boldsymbol{\chi}\right\|_{\ell_1}\right\} \quad \textbf{subject to} \quad \|\boldsymbol{A}\boldsymbol{\chi}-\boldsymbol{\mathcal{E}}_s\|_{\ell_2}\leq\boldsymbol{\delta} \tag{3.9}$$

It is worth underlying that the qualitative information which enables (and suggests) the use of (3.9) can be eventually achieved by a preliminary estimation (based, for instance, on the approach (3.7)). Saying it in other words, eq. (3.9) can be eventually seen as a possible 'post processing' technique.

3.2.2 Numerical analysis

In order to investigate the performances of the proposed CS inspired inversion techniques, some numerical examples with simulated data are considered in the remainder of this Section.

In particular, all examples deal with scatterers belonging to the range of applicability of the approximation (1.12) [*Di Donato et al.,* 2015a]. In each example the scattering equation is first linearized and then the solution is looked for by considering one of the above introduced approaches.

A. On the choice of δ *parameter*

The choice of the positive tolerance parameter δ is a non-trivial issue. In fact, besides the level of required precision and the amount of noise on data, this parameter depends on the model error introduced by the field approximation (1.12). Of course, the larger the expected model error and noise on data, the larger the parameter δ.

In absence of model error, only the noise on data plays a role in the choice of δ. In this case, if the measurement system specifications (in terms of dynamic range and SNR) are known (which is a reasonable assumption),

the choice of δ directly relates to the SNR [*Lustig et al.*, 2008, *Gurbuz et al.*, 2009].

On the contrary, when dealing with problems when the model error is unavoidably present (like the case at hand), the choice of δ is not any more straightforward, as the model error can be hardly quantified a priori.

On the other hand, also in presence of model error, it is possible to define an interval which δ belongs to. In particular, the upper bound of this interval is represented by the ℓ_2 norm of the data $\boldsymbol{\mathcal{E}_s}$. As a matter of fact, in order to avoid the trivial solution, that is the null vector, δ must be selected lower than $\|\boldsymbol{\mathcal{E}_s}\|_{l_2}$, as with $\delta \geq \|\boldsymbol{\mathcal{E}_s}\|_{l_2}$ the null vector could satisfy the constraint on the data and simultaneously minimize the objective function. Accordingly, in performing the numerical analysis, δ is set such that $\delta = \hat{\delta}\|\boldsymbol{\mathcal{E}_s}\|_{\boldsymbol{\ell_2}}$ with $\hat{\delta} < 1$. The lower bound, instead, is dictated by the amount of noise on data. Then, $\hat{\delta}$ is chosen inside this interval through an iterative optimization procedure, similarly to what is done in cross-validation strategies [*Gurbuz et al.*, 2009, *Zhang et al.*, 2012b, *Boufounos et al.*, 2007]. In particular, $\hat{\delta}$ is set equal to the smallest value which allows to obtain a feasible (where with feasibility one means the possibility to find a solution that satisfies the constraint on the data consistency). In fact, if $\hat{\delta}$ is too small, the problem could be unfeasible, as the set identified by the data constrain could be an empty set and no solution could exists at all.

B. Numerical examples

In the following examples, one or more unknown objects are embedded into a square imaging domain Ω of side L. N receivers and M transmitters, with $N = M$, are located on a circumference Γ of radius $R = 4\,\lambda$. The number of cells N_c of the discretized domain is chosen according to the Richmond's rule. Furthermore, the scattered field data are corrupted with a random Gaussian noise with different SNR levels.

In the first example, five lossless point-like targets are considered (see fig. 3.1(a)). The imaging domain is discretized into $N_c = 46 \times 46$ square

cells, while the inverse problem grid is 23×23 cells. Moreover $L = 2\lambda$, $N = M = 21$ and $\mathrm{SNR} = 10\mathrm{dB}$. By estimating the target support, fig. 1(b), it is possible to choose the more suitable approach. Accordingly, the approach described in 3.2.1.A is exploited and the result reported in figs. 3.1(c)-(d) is obtained. As it can be seen, the joint exploitation of VE and CS allows a very accurate reconstruction ($\hat{\delta}$=0.15 and *err*=0.26%). In order to understand the roles played by VE experiments and field approximation respectively, in figs. 3.1(e)-(f) is reported the reconstruction obtained by using the VE and approximating the internal field with the incident one. As it can be seen, reconstructions appear to be considerably worse ($\hat{\delta}$=0.15 and *err*=10%). Notably, exploitation of the BA to the original data yields completely unreliable results.

In the second example, three lossless squares embedded in a domain of side $L = 3\lambda$ are considered. The domain is discretized into $N_c = 50 \times 50$ cells and the SNR is 20 dB, $N = M = 26$. As the scatterers are not sparse in the pixel basis, see fig. 3.2(b), the approach (3.7) is used in order to retrieve the unknown profile. The result agrees with the reference contrast profile, as it can see in figs. 3.2(c)-(d) ($\hat{\delta}$=0.23 and *err*=8%).

As a third example, the lossy profile in fig. 3.3(a)-(b) is presented. In this example, $N = M = 21$, $L = 2\lambda$, $N_c = 32 \times 32$ and $\mathrm{SNR} = 20\ dB$. Also in this case, the CS based approach is exploited and the reconstruction is shown in figs. 3.3(d)-(f) ($\hat{\delta}$=0.16 and *err*=11%). For the sake of comparison, the reconstruction by means of TSVD was also performed in such a case, by considering the truncation index N_T equal to 80. As it can be seen in figs. 3.3(g)-(h), the retrieved profile is less accurate, especially for the imaginary part. As a matter of fact, CS is able to outperform the TSVD both in terms of shape and quantitative reconstruction of the electromagnetic features.

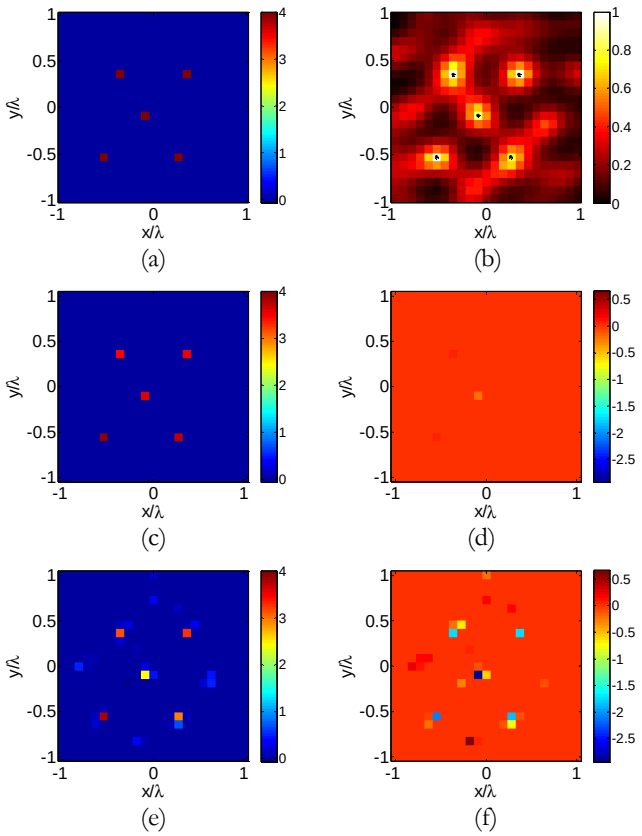

Figure 3.1. Numerical assessment of CS linearized approaches. The five lossless point-like scatterers. (a) Actual contrast profile. (b) LSM indicator map with the selected pivot points superimposed as dots. Contrast profile retrieved profile via the approach (3.5) (c) real and (d) imaginary part. The retrieved profile with approach (3.5) cast for just the virtual incident fields: (e) real and (f) imaginary part.

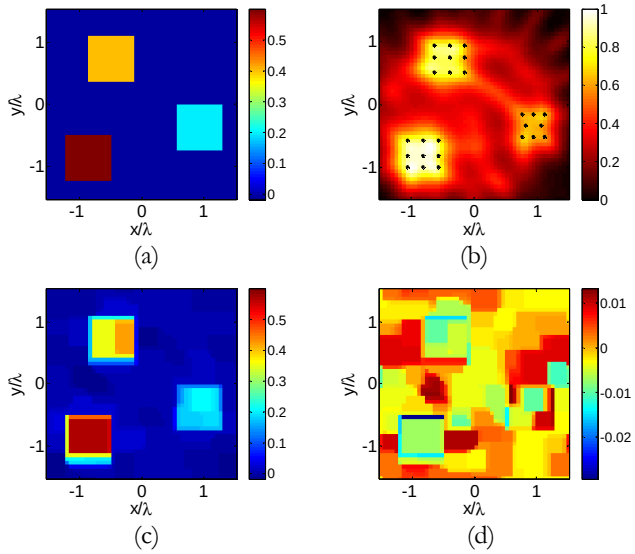

Figure 3.2. Numerical assessment of CS linearized approaches. The three square target. (a) Actual contrast profile. (b) LSM indicator map with the selected pivot points superimposed as dots. The retrieved profile with approach (3.7): (c) real and (d) imaginary part.

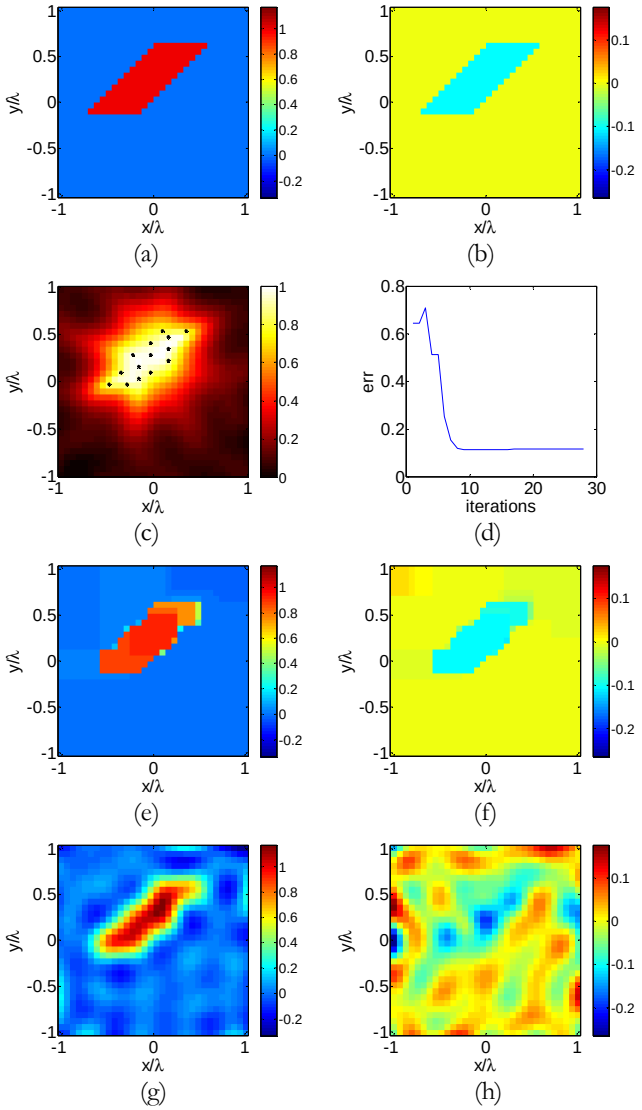

Figure 3.3. Numerical assessment of CS linearized approaches. The slanted square target. Contrast reference profile: (a) real part, (b) imaginary part. (c) LSM indicator map with the selected pivot points superimposed as dots. (d) The mean square error versus the number of iterations. The retrieved profile with approach (3.7): (e) real (f) imaginary part. The retrieved profile with TSVD: (g) real (h) imaginary part.

In the last example a square ring scatterer with $\varepsilon = 1.3$ is considered (see fig. 3.4). In particular, $N_c = 32 \times 32$, $M = N = 21$, $R = 4\lambda$, $L_D = 1.33\lambda$. The reconstruction by using the approach (3.7) already gives an accurate result ($\hat{\delta} = 0.072$ and $err = 8\%$) and suggests the scatterer at hand is in the class suitable for the corner identifier approach. Then, application of the formulation (3.9) allows a still better reconstruction as seen in figs 3.4(e)-(f), achieving an error as low as 1.5% ($\hat{\delta} = 0.072$).

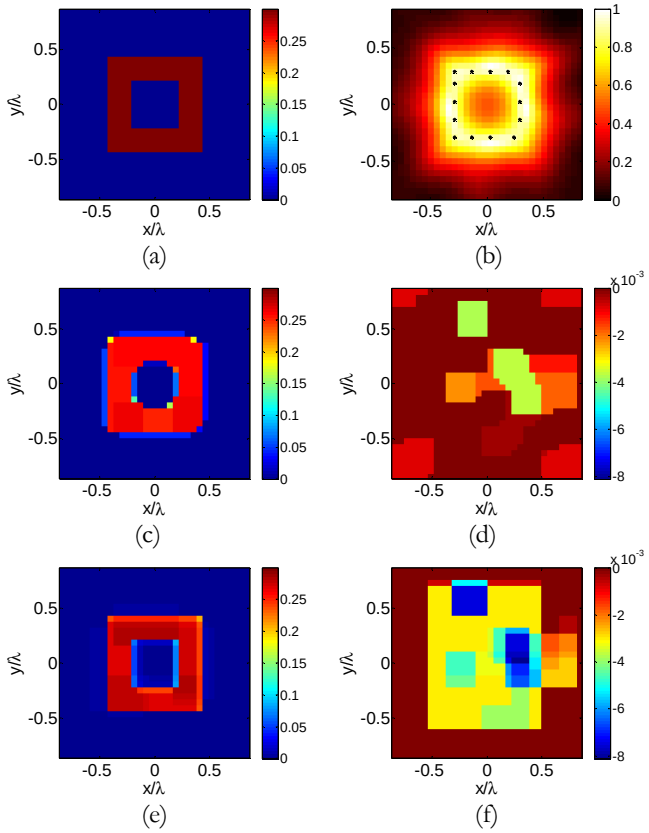

Figure 3.4. Numerical assessment of CS linearized approaches. The ring square example. (a) Real part of the contrast reference profile. (b) LSM indicator map with the selected pivot points superimposed as dots. The retrieved profile by means of the approach (3.7): (c) real and (d) imaginary part. The retrieved profile by means of the approach (3.9): (e) real and (f) imaginary part.

Many other examples confirm the interest of the proposed VE-CS based linearized method.

3.3 Compressive sensing and nonlinear inverse scattering

According to CS theory, given a linear problem wherein the unknown function $\boldsymbol{x}$ can be assumed to be sparse, it can be solved by considering the well known Basis Pursuit denoising (see eq. (3.3)), or equivalently the following ℓ_1-norm constrained optimization problem:

$$min\{\|\boldsymbol{A}\,\boldsymbol{\Psi}\boldsymbol{s}-\boldsymbol{y}\|_{\ell_2}\} \quad s.t. \quad \|\boldsymbol{s}\|_{\ell_1} \leq \sigma \tag{3.10}$$

or even the dual ℓ_1-norm penalized least squares problem:

$$\min\{\|\boldsymbol{A\Psi s} - \boldsymbol{y}\|_{\ell_2} + k\|\boldsymbol{s}\|_{\ell_1}\} \tag{3.11}$$

where σ is positive real number, which is related to the number and the power of the contributing nonzero elements of $\boldsymbol{s}$, while k is a positive parameters controlling the relative weight of the ℓ_1 regularization term. Note in equation (3.10) the optimization problem is organized in such a way to minimize the ℓ_2-norm of data-unknowns relationship by constraining the unknown function inside a limited space defined by the ℓ_1-norm constraint. In (3.11), the problem is instead faced by an unconstrained optimization scheme wherein the sparsity is enforced by a penalty function.

Applications of CS to non linear inverse scattering have not been found in the literature (but for [*Desmal and Bagci*, 2014, *Azghani et al.*, 2015]). For this reason, in this section two possible ways to exploit the CS theory are explored in conjunction with CSI. A further possibility is explored in the next Section with reference to the class of distorted iterated approaches.

Let us suppose the unknown profile is sparse in some suitable basis Ψ. In order to improve the inversion results obtained by means of CSI and to make them both more reliable against the occurrence of false solutions as well as more robust with respect to ill conditioning, sparsity can be take into account during the inversion procedure, considering both the possibilities suggested in eqs. (3.10) and (3.11).

In fact, with respect to the traditional CSI, sparsity can be enforced both by adding a ℓ_1-norm constraint, i.e. by limiting the research space of the unknown as well as by introducing a ℓ_1-norm term in the cost functional as penalization. The two strategies are detailed in the subsections which follow.

3.3.1 Sparsity constrained scheme

Inspired by approach (3.10), a ℓ_1-norm constraint limiting the space of research of the unknown can be included into the CSI scheme. More in detail,

the inverse problem is solved by researching the global minimum of the functional (D.1) inside the space defined by all the unknowns whose ℓ_1-norm of the coefficients of the representation basis Ψ is lower than a positive parameter σ, i.e.:

$$\min_{W,\chi} \Phi(W,\chi) \quad subject\ to\ \|s\|_{\ell_1} \leq \sigma \tag{3.12}$$

The inclusion of the ℓ_1-norm constraint could allow to more easily fall into the right attraction basin, by avoiding to be trapped in a false solution during the minimization procedure. All local minima of functional (D.1) not belonging to the space of research defined by the constraint do not represent feasible solutions anymore. This can be simply explained by considering a generic monodimensional non quadratic cost functional, as the one in fig. 3.5. In fact, if one were so lucky to limits the space of research just at the right attraction basin, which is the one highlighted by the dashed line, the local minimum would exactly corresponded to the global optimum.

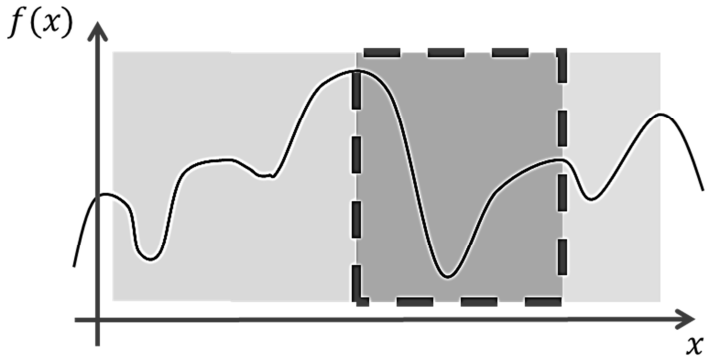

Figure 3.5 Plot of a generic monodimensional and non quadratic cost functional. The different local minima correspond to different attraction basins.

With respect to the standard CSI scheme, at each iteration the sparsity constraint implies a modification of the line minimization step along search direction. In particular, the minimization step length μ_k has to be chosen such to be a minimizer of problem (D.3) and such that the solution at the

next iteration belongs to the research space, i.e. $\|s_k + \mu_k \Delta s_k\|_{\ell_1} \leq \sigma$. In other words, μ_k has to be lower than the distance β between the current solution s_k and the boundary of the feasible solution set along the current descent direction, (identified by the gradient of the functional Φ with respect to χ).

As performed in the hit step described in [*Isernia et al.*, 2000], the distance β along the descent direction $\hat{\imath}_g$ is evaluated as:

$$\beta: \quad \left\| s^{(k)} + \beta \hat{\imath}_g \right\|_{\ell_1} = \delta \tag{3.13}$$

At each iteration the solution of problem (D.3) is compared with the distance β. In particular, if μ_k is lower than β, the solution is updated according to (D.2) and it is still inside the feasible set. Otherwise, μ_k is set equal to β. This means that the solution belongs to the boundary of the feasible set.

Unlike the case considered in [*Isernia et al.*, 2000], the problem at hand is non-linear and, so, the solution does not necessary belong to the boundary of the feasible set. As a consequence, to avoid the stagnation of the minimization procedure on the boundary, the solution is projected inside the set defined by the sparsity constraint, by nullifying the coefficients whose magnitude is below the 20% of magnitude of the maximum coefficient. This is reasonable as the contrast function is expected to be sparse or compressible.

3.3.2 Sparsity penalized scheme

Rather than enforcing sparsity by means of a constraint, the solution of inverse problem can be also obtained by adding in the functional (D.1) a penalty term that accounts for the peculiar feature of the search contrast function, i.e.:

$$\min_{W,s} \Phi(W,s) + \Phi^P(s) = \Phi(W,s) + k\|s\|_{\boldsymbol{\ell_1}} \tag{3.14}$$

Unlike the previous approach which limits the space of search thus enhancing the possibilities to fall within the right attraction basin, in (3.14) the inclusion of the penalty term Φ^P modifies the shape of the cost functional and its attraction basins. All local minima of (D.1) not satisfying the sparsity condition induced by the penalty term disappear when considering (3.14).

The implementation of this new regularization term in the framework of a gradient-projection optimization is detailed in the following. The expression of the gradient for the functional (3.14) within a conjugate gradient scheme is analytically derived by following the approach in [*Isernia et al.*, 1997]. The gradient of the penalty term Φ^P respect to $\boldsymbol{s}$ is computed by using the following definition:

$$\Delta\Phi^P{}_s = \langle \nabla\Phi^P{}_s, \Delta s \rangle \tag{3.15}$$

where the variation Δs gives rise to $\Delta\Phi^P{}_s$, which represents the variation of Φ^P. Then by considering the expression of $\Phi^P(s)$, it follows that

$$\Delta\Phi^P{}_s = \frac{k}{2}\langle s^{\frac{1}{2}}, \Delta s\, s^{-\frac{1}{2}} \rangle + c.c. = \frac{k}{2}\langle s^{\frac{1}{2}} \left(s^{-\frac{1}{2}}\right)^* , \Delta s \rangle + c.c. \tag{3.16}$$

where $\langle \cdot,\cdot \rangle$ denotes the scalar product, while $c.c.$ stands for the conjugate of the first addendum. Then comparing eq. (3.15) and (3.16) it follows:

$$\nabla\Phi^P{}_s = k\,\frac{s}{|s|} \tag{3.17}$$

On the other hand, even if for the gradient an analytical expression can be obtain, for the line search parameter μ_k it is not possible to reduce the problem (D.3) to the solution of an algebraic equation, due to the nature of the involved operator. So, unfortunately, the problem (D.3) must be numerically solved, thus increasing the computational burden.

Let us observe that in many case of actual interest the targets are piecewise constant dielectric profiles and are sparse in term of the step

functions, as recalled in the Section 3.2. As a consequence, the penalty term can be modified in $\Phi^P(\chi) = k\|D\chi\|_{\ell_1}$, where D is the vector containing the forward differences of the unknown function χ. In this case the analytical expression of the gradient is $\nabla\Phi^P{}_s = -D\left(k\,\frac{D\chi}{|D\chi|}\right)$.

3.3.3 Numerical validation

In order to assess performances of the proposed approaches, let us consider two numerical examples dealing with simulated data. As usual, a number of measurements points M and transmitters N is considered according to [*Bucci and Isernia*, 1997]. The receivers and transmitters are spaced on a circumference of radius R. The scattered field data is obtained by means of a full-wave forward solver based on CG-FFT procedure and corrupted with a random Gaussian noise with known SNR.

Concerning the choice of the positive parameter k controlling the relative weight of the l_1 penalty term in (3.14), an accurate numerical investigation has revealed that the optimal choice is on the order of the ratio $1/(2\,N_c\,DOF)$, where DOF are the degrees of freedom of the problem at hand, i.e. the maximum amount of independent data. In such a way the penalty term is normalized respect to the number of independent data times the numbers of cells. The factor 2 depends on the presence of the gradient respect to both x and y axes.

On the contrary, the choice of σ parameter in eq. (3.12) influences the dimension of the search space. If it is too large, the set of feasible solutions could be too wide and the constraint would not influence the minimization procedure. On the other side, one cannot select a very small value, as the actual solution could not be included in such a small set. More in detail, the σ parameter represents an upper bound for the energy in ℓ_1-norm of the coefficients of the considered representation basis. This latter is obviously unknown and it can be only estimated by considering some priori information. In the following the role of this parameter is analyzed by

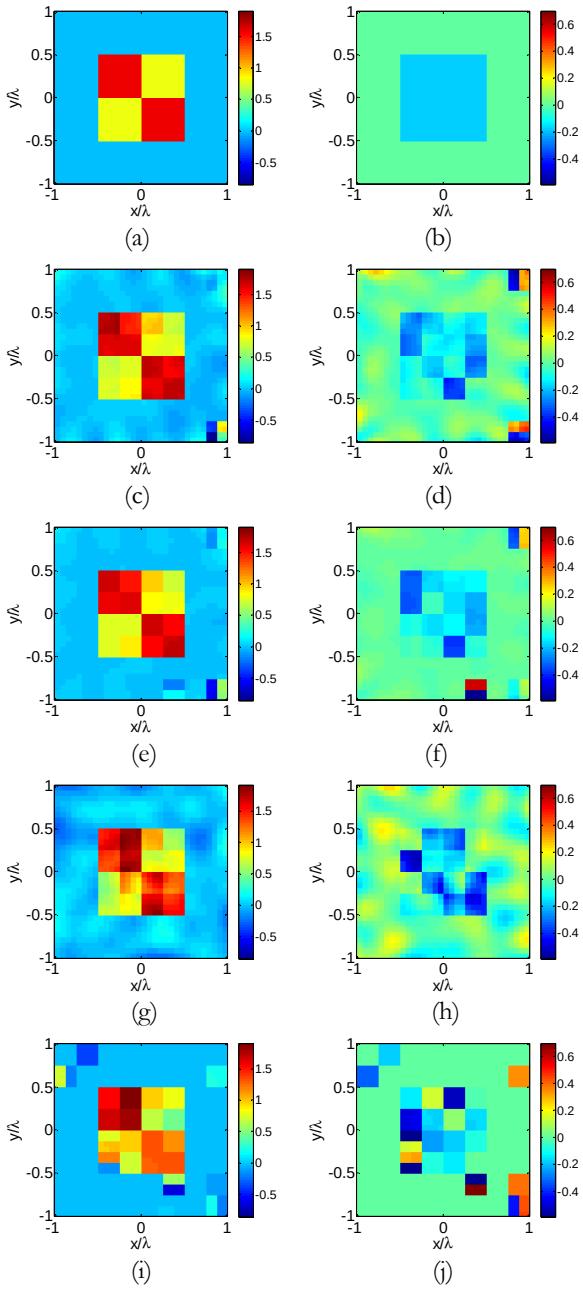

Figure 3.6. Numerical assessment of CS non linear approaches. The inhomogeneous square. (a) Real part and (b) imaginary part of the contrast reference profile. The retrieved profile with approach (3.12) (σ = 150, err=5%): (c) real and (d) imaginary part. The retrieved profile with approach (3.12) (σ = 100, err=4%): (e) real and (f) imaginary part. The retrieved profile with approach (3.12) and considering $M = V = 14$ (σ = 150, err=7%): (g) real and (h) imaginary part. The retrieved profile with approach (3.12) and considering $M = V = 11$ (σ = 150, err=16%): (i) real and (j) imaginary part.

considering two overestimations of the actual value of ℓ_1 energy of about 30% and 95%.

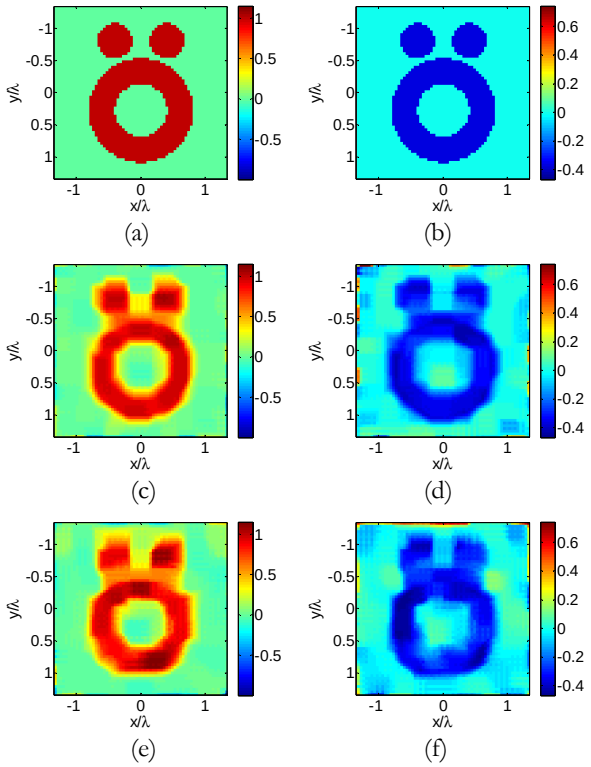

Fig. 3.7. Numerical assessment of CS non linear approaches. The lossy Austria profile. (a) Real part and (b) imaginary part of the contrast reference profile. The retrieved profile with approach (3.14) (k = $5 \cdot 10^{-8}$, err=15%): (c) real and (d) imaginary part. The retrieved profile with approach (3.14) and considering $M = V = 16$ (k = $5 \cdot 10^{-8}$, err=19%): (e) real and (f) imaginary part

In order to evaluate the robustness of the methods and show the possible advantages offered by sparsity regularizations, an analysis of the performances when varying the number of data exploited for the inversion procedure is also provided. In particular, a reduction of both the number of transmitters and receiver antennas are considered.

The first numerical example is dealt with a lossy non-homogeneous square scatter, shown in figs. 3.6(a)-(b). The working frequency is $1GHz$, while the region of interest is a square of side $\mathrm{L} = 0.6\,m$, and the scatterer is hosted in free space. Moreover, $\mathrm{R} = 1.2\,m$ and a number of antennas equal to $M = V = 21$ is initially considered. The data are corrupted by considering SNR equal to $10dB$. The iterative procedure is initialized by using a back-propagation solution.

The CSI is implemented by adopting the projection of the unknown contrast function onto wavelet Haar basis of level equal to 2, in order to obtain the sparsest target representation. The number of cells used to discretize the scenario are $N_c = 32 \times 32$. Two different value of the σ parameter (100 and 150) are considered in order to understand its role in the reconstruction procedure. Note that the ground truth ℓ_1-norm energy is 77.

The contrast profiles retrieved by approach (3.12), and after a number of iterations equal to 1000, are reported in figs. 3.6 (c)-(f). The results are in agreement with the reference contrast profile with a negligible reconstruction error.

To get a deeper understanding of the results, the reconstruction one is able to achieve when considering a reduced number of data is also checked. In particular a number of independent data equal to 98 ($M = V = 14$) and 66 ($M = V = 11$) are considered. The reconstruction errors are about 7% and 16%, respectively. As it can be seen in figs. 3.6(g)-(j) enforcing sparsity allows the achievement of reliable results also in case of a significant reduction of the number of antennas. Note the number of DOF for the scenario at hand is about 231, which represents the maximum amount of independent data [*Bucci and Isernia*, 1997].

By analyzing other examples, it is revealed that approach (3.12) is strongly influenced by the adopted representation basis and is mainly suitable for very sparse contrast profile. In fact, if number of non zero elements S is large the space of research could be not restricted as much as possible and there could be again the risk of being trapped in false solutions. Moreover, the above discussed projections could continue without a solution convergence and the procedure could oscillate between different false solutions.

In order to test the potentiality of the penalized CSI approach, in the second example the Austria profile is considered inside a domain divided into $N_c = 64 \times 64$ cells. This profile is often used as benchmark in testing the inverse scattering inversion algorithm [*Chen.*, 2010, *Xu et al.*, 2015, *van den Berg et al.*, 2003]. In this example, a more challenging case is considered due to the presence of losses (figs. 3.7(a)-(b)). The working frequency is $400MHz$, while

the region of interest is a square of side $\mathrm{L} = 2\,m$, and the scatterer is hosted in free space. Moreover, $\mathrm{R} = 3\,m$ and at the beginning a number of antennas equal to $M = N = 25$ is considered. The data are corrupted by considering a SNR equal to $20dB$. The iterative procedure is initialized by using a back-propagation solution and the profile is represented by using the step functions.

The results, reported in figure 3.7 are very accurate also when 136 number of independent data are collected (with a reduction of more than 2 respect to the DOF), as witnessed by the synthetic error (err=0.19). Note the result in figs. 3.7 (e)-(f) is really interesting if compared with [*Chen.*, 2010] and [*van den Berg et al.*, 2003], which process respectively a 16×32 and a 48×48 scattered field data matrix.

Many other examples have proved the considerable performances of approach (3.14) to deal with targets having both complex shapes and large values of contrast. However, if the problem at hand exhibits a larger degree of non linearity, the addition of the ℓ_1 penalty term in the cost functional (D.1) could not be able to compensate the presence of local minima, as also discussed for the RCSI method. In such a case, better robustness and performances could be observed by considering this approach in conjunction with 'contrast sources' oriented regularizations and scattering conditioning.

3.4 CS-regularized distorted iterated virtual experiments method

In Section 2.3, a novel iterative approach consisting in successive linearizations, based on the emerging framework of the VE, has been introduced and described. The concept of field conditioning is exploited within an iterative scheme, wherein the relevant Green's function and the VE are updated in order to achieve an approximated expression of the total field within the investigated domain. This approximation is then exploited in order to linearize the inverse scattering problem and refine the unknown contrast distribution at each iteration.

By exploiting the CS theory, such innovative approach can be further improved in order to achieve nearly optimal imaging of unknown targets. The CS theory involves the solution of a constrained optimization problem, which relies on an iterative procedure, so it implies a larger computational effort with respect to the TSVD, used in Section 2.3. However, this is a price which is worth being paid, as it offers interesting advantages both in term of achievable resolution as well as in terms of a potential reduction of the measurement apparatus complexity (as discussed in Section 3.3.3).

In order to set the details of the method, and appreciate then actual performances, let us consider a piecewise constant target, which is of course sparse if represented in terms of step functions. The linearized inverse problem involved in step 5) of DIVE method (see Section 2.3.1) can be solved by rewriting the 'orientation invariant' approach (3.8), i.e.:

$$\min_{\Delta\boldsymbol{\chi}^{\boldsymbol{k}}} \left\{ \left\| \boldsymbol{D_h}\, \boldsymbol{\chi}^{\boldsymbol{k+1}} \right\|_{\ell_1} + \left\| \boldsymbol{D_v}\, \boldsymbol{\chi}^{\boldsymbol{k+1}} \right\|_{\ell_1} + \left\| \boldsymbol{D_d}\, \boldsymbol{\chi}^{\boldsymbol{k+1}} \right\|_{\ell_1} \right\}$$
$$\textbf{subject to} \quad \left\| \boldsymbol{A}^{\boldsymbol{k}} \Delta\boldsymbol{\chi}^{\boldsymbol{k}} - \boldsymbol{y} \right\|_{\ell_2} \leq \boldsymbol{\delta} \tag{3.18}$$

where $\Delta\boldsymbol{\chi}^{\boldsymbol{k}} = \boldsymbol{\chi}^{\boldsymbol{k+1}} - \boldsymbol{\chi}^{\boldsymbol{k}}$, $\boldsymbol{y}$ is the data vector containing the differential scattered fields arising in the VE, and $\boldsymbol{A}^{\boldsymbol{k}}$ is the matrix that relates at each iteration the unknown vector to the data vector according to the subsection 2.3.1. Note for $k = 0$ the first estimation of the contrast function is performed by considering the original approach in (3.8).

It is worth observing that while the TSVD regularization adopted in Section 2.3 acts at each iteration on the perturbation $\Delta\boldsymbol{\chi}^{\boldsymbol{k}}$, the CS inspired regularization (3.18) enforces sparsity on the whole contrast profile.

In the following, in order to carry out a comparison with the TSVD, the same examples analyzed in Section 2.3.2 and 2.4, dealing with both numerical and experimental data, are considered.

3.4.1 Assessment with numerical and experimental data

An important point for the CS regularization strategy is the choice of the suitable parameter $\boldsymbol{\delta}$ in (3.18), as also discussed in Section 3.2.2. Nevertheless, as DIVE is based on successive refinement of the contrast profile, it turns out to be more robust respect to the choice of $\hat{\delta}$ parameter.

As a consequence, in the following examples $\hat{\delta}$ is considered constant during the iterative procedure. However, as in the initialization step a high amount of model error is expected and no priori information about the unknown scatterer is available, a larger value of $\boldsymbol{\delta}$ is chosen with respect to the one adopted for $k > 0$. For instance in the example dealing with simulated data we consider $\hat{\delta} = 0.50$ for iteration $k = 0$ and $\hat{\delta} = 0.40$ for $k > 0$.

Moreover, when dealing with Fresnel data, because of the aspect limited measurement configuration, a lower level of accuracy has to be required especially in case of undersampled data. Therefore, we use in the following, $\hat{\delta} = 0.75$ for $k = 0$ and $\hat{\delta} = 0.40$ for $k > 0$, in case of a larger number of data, while in case of undersampled data $\hat{\delta} = 0.75$ for $k = 0$ and $\hat{\delta} = 0.55$ for $k > 0$ are considered.

For the kite target, the results are reported in fig. 3.8. The initial estimation χ^0 is reported in figs. 3.8(a)-(b), while the reconstruction obtained at the last iteration is shown in figs. 3.8(c)-(d). As it can be seen by comparing this latter with the reconstruction obtained with TSVD (see figs. 2.6(f)-(g)), the CS inspired inversion is able to obtain a nearly optimal reconstruction both in term of shape and electromagnetic properties, as also witnessed by the final reconstruction error equal to 4%. Moreover, the profile in the background region appears more homogeneous than the one in figs. 2.6(f)-(g). In table V the number of iterations and the error metrics are summarized.

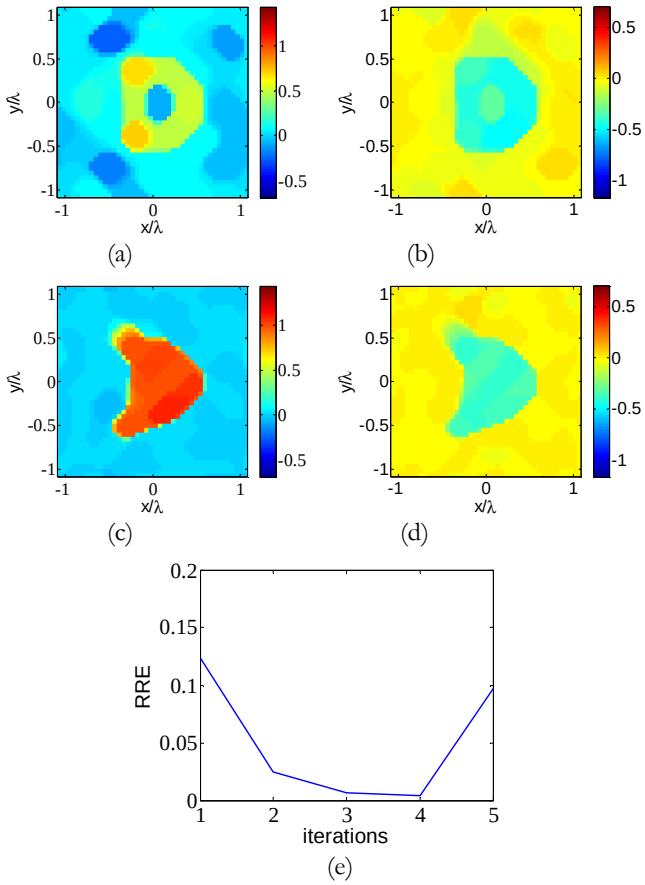

Figure 3.8. Numerical assessment of DIVE-CS. The kite target: real part and imaginary part of the retrieved contrast function at the initial step (a)-(b) and at the last iteration (c)-(d). The RRE versus iterations for DIVE-CS(e).

	err (k=0)	***err***	***RRE***	***# iterations***
DBIM-TSVD	0.90	1.15	0.12	3
DIVE-TSVD	0.77	0.20	0.01	13
DIVE-CS	0.46	0.04	0.004	5

Table V. Numerical assessment of DIVE-CS. The kite target: overall details of the inversion procedures.

In order to evaluate the robustness of the methods and demonstrate the possible advantages offered by sparsity regularizations, let us consider, for the case of Fresnel data set, an analysis of the performances with a reduced number of data. In the following the total dimension of the processed data matrix is referred with K.

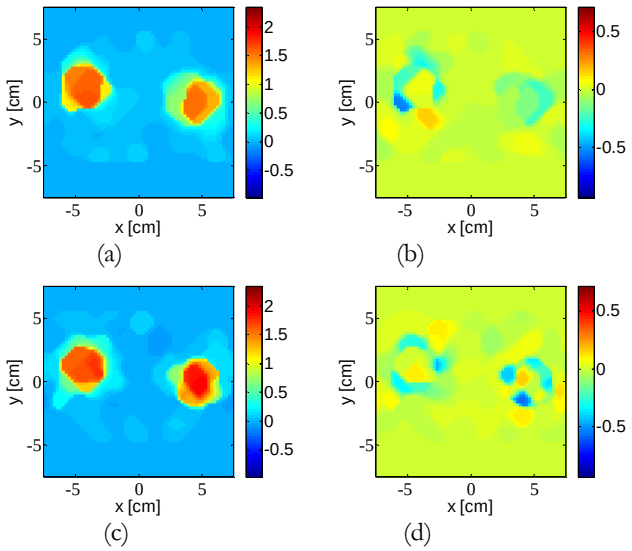

Figure 3.9. Validation of DIVE-CS with experimental data: the Fresnel TwinDielTM target at 6 GHz: (a)-(b) real part and imaginary part of the retrieved contrast function. (c)-(d) are the same of (a)-(b) for reduced number of processed data.

	RRE	***# iterations***
DIVE-TSVD – K=72x36	0.06753	12
DIVE-CS – K=72x36	0.06826	5
DIVE-CS – K=36x18	0.05374	7

Table VI. The Fresnel *TwinDielTM*: overall details of the inversion procedures.

For the *TwinDielTM* target the results are reported in fig. 3.9. The working frequency is 6 GHz and the side of the squared investigated area is 0.15 m. The result is achieved by adopting both the original data set, constituted by 36 incident fields and 72 receivers per view, and a 18×36 multiview-multistatic data matrix, obtained by undersampling the original data. As it can be seen, the reconstruction obtained by considering the CS tool emphasizes the remarkable improvements respect to the TSVD (see figs.2.7(h)-(i)). For more details on the number of iterations and final RRE see Table VI.

For the *FoamTwinDielTM* target, the working frequency is set equal to 4 GHz, and the side of the investigated area is 0.175 m. The results reported in fig. 3.10 are achieved by adopting both a 45×18 and 23×18 multiview-multistatic data matrices. Again, the CS based inversion strategy allows to improve the reconstruction accuracy (fig. 3.10) with respect to the results

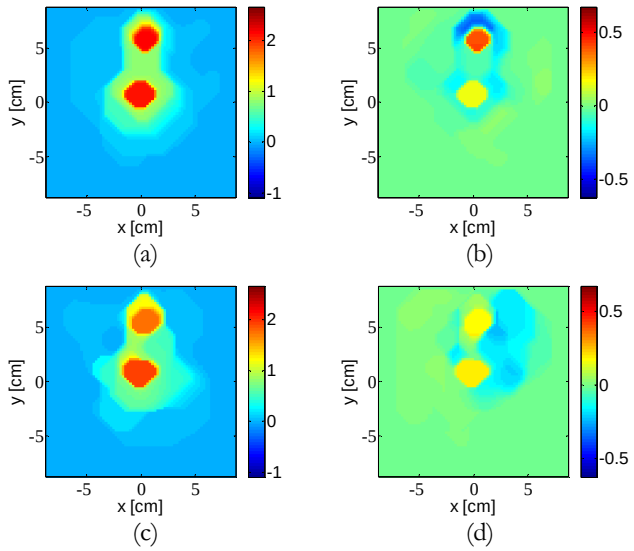

Figure 3.10. Validation of DIVE-CS with experimental data: the Fresnel *FoamTwinDielIntTM* target at 4 GHz: (a)-(b) real part and imaginary part of the retrieved contrast function. (c)-(d) are the same of (a)-(b) for reduced number of processed data.

	RRE	***# iterations***
DIVE-TSVD - K=45x18	0.01669	17
DIVE-CS - K=45x18	0.01419	7
DIVE-CS - K=23x18	0.09123	6

Table VII. The Fresnel *FoamTwinDielIntTM*: overall details of the inversion procedures.

achieved in Section 2.3 (figs. 2.9(f)-(g)). For more details on the number of iterations and RRE see Table VII.

For the *FoamDielIntTM* target, the results, reported in fig. 3.11, are achieved by adopting 23×18 and 9×9 multiview-multistatic data matrices. The working frequency is 4 GHz and the side of the investigated area is 0.125 m. As it can be seen, the CS tool is able to provide a nearly optimal reconstruction of the electromagnetic properties of both the two nested cylinders, also in case of more challenging case of extreme reduction of the data matrix. Note that the results in figs. 3.11 (c)-(d) is really surprising as the target is correctly retrieved even if a 9×9 scattered field data matrix is processed. For more details see Table VIII.

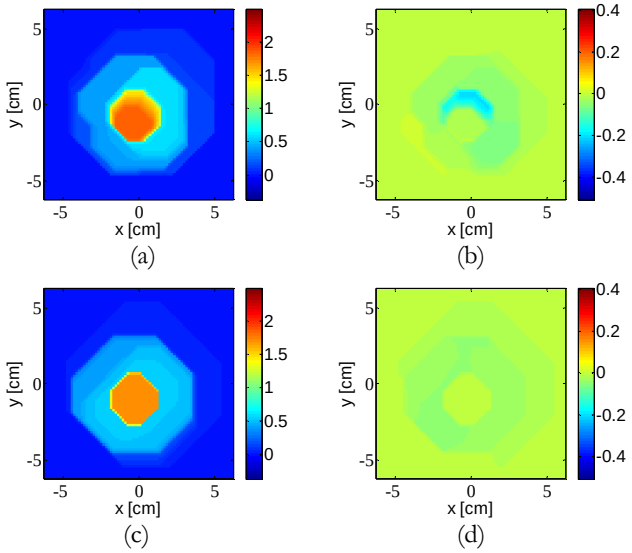

Figure 3.11. Validation of DIVE-CS with experimental data: the Fresnel *FoamDielIntTM* target at 4 GHz. (a)-(b) Real part and imaginary part of the retrieved contrast function. (c)-(d) are the same of (a)-(b) for reduced number of processed data.

	RRE	***# iterations***
DIVE-TSVD - K=23x18	0.0182	10
DIVE-CS - K=23x18	0.0188	5
DIVE-CS - K=9x9	0.0354	6

Table VIII. The Fresnel *FoamDielIntTM*: overall details of the inversion procedures.

3.5 Possible developments

The inversion procedures proposed in this Chapter are just some of the many possibilities offered by the CS theory. In fact, this new paradigm is in continuous development and, so, new interesting possibilities and improvements are also expected.

First of all, the proposed approaches are based on the sparsity assumption and so limited by the choice of a suitable basis. In this respect, the possibility of recovering signals from undersampled data has been recently investigated in the common situation where such signals are not sparse in an orthonormal basis or incoherent dictionary, but in a truly redundant dictionary [*Candès et al.*, 2011]. In fact, there are numerous practical examples in which a signal of interest is not sparse in an orthonormal basis, and more often sparsity is expressed not in terms of an orthonormal basis but in terms of an overcomplete dictionary [*Candès et al.*, 2011]. This means that the signal is expressed by means of some overcomplete dictionary, belonging to $\mathbb{R}^{n\times d}$, in which there are possibly many more columns than rows. The use of overcomplete dictionaries is now widespread in signal processing and data analysis, as there may not be any sparsifying orthonormal basis. Moreover, the research community has come to appreciate and rely on the flexibility and conveniences offered by overcomplete representations.

Moreover, recently [*Candès et al.*, 2008] has introduced the use of a new norm able to outperform the classical ℓ_1-norm in the term of fewer measurements for sparse signal recovery. The algorithm consists of solving a sequence of weighted ℓ_1-minimization problems where the weights used for the next iteration are computed from the value of the current solution. Superior gains are also achieved when the weighted ℓ_1-norm is applied to recover signals with assumed near-sparsity in overcomplete representations.

Another possibility is offered by non-convex regularizer, which can promote sparsity more strongly than the ℓ_1-norm regularization, but generally leads to a non-convex optimization problem with non-optimal local minima. More recently in [*Selesnick and Bayram*, 2014, *Selesnick et al.*, 2015] maximally sparse approaches are proposed, which require a suitable parametric non-

convex (sparsity-inducing) penalty function which are constrained so to ensure convexity of the total cost function. Examples of such functions are the logarithmic and the arctangent penalty [*Selesnick and Bayram*, 2014, *Selesnick et al.*, 2015].

All these interesting possibilities could be explored in the near future in order to improve the performances of the technique proposed in this Chapter, both in the linear and non-linear framework.

Part II

NEW APPROACHES FOR MICROWAVE IMAGING IN BIOMEDICAL DIAGNOSIS AND SUBSURFACE PROSPECTIONS

4

A compressive sensing approach for breast cancer microwave imaging enhanced by magnetic nanoparticles

4.1 Introduction and relevance of the problem

In the last years, the evidence that human tissues exhibit different electromagnetic properties at microwaves, depending on their typology and physio-pathological status, has given rise to a huge interest in MWI for medical applications. In particular, MWI has gained increasing interest in breast cancer diagnostics [*Fear et al.*, 2002].

However, recent studies on the electric properties of mammary tissues have outlined that the electric contrast between healthy fibroglandular tissues and cancerous ones may be not as high as initially thought [*Lazebnik et al.*, 2007]. As a consequence, in order to improve sensitivity and specificity of a microwave based diagnostic technique, the use of contrast agents, able to increase the contrast between fibroglandular healthy tissues and cancerous ones, has been introduced [*Shea et al.*, 2010, *Mashal et al.*, 2010, *Chen et al.*, 2010].

In particular, Magnetic Nanoparticles have been recently considered [*Bellizzi et al.*, 2011, *Helbig et al.*, 2014], since they are already allowed for clinical use and, by exploiting biochemical targeting techniques [*Leuschner et al.*, 2006, *Park et al.*, 2009], they present a unique capability of inducing a specific and selective contrast into tumoral tissues. As a matter of fact, the non-magnetic nature of human tissues allows to pursue the cancer imaging through the reconstruction of a magnetic contrast, specifically associated to the tumor, embedded into a purely electric scenario.

The feasibility of the technique has been already demonstrated through a wide numerical analysis involving anthropomorphic breast phantoms [*Bucci*

et al., 2014a, *Scapaticci et al.*, 2014], as well as through preliminary experimental measurements [*Helbig et al.*, 2014]. In particular, in [*Scapaticci et al.*, 2014] an effective imaging procedure based on the TSVD has been proposed for the solution of the inverse problem underlying the technique.

Notably, since only a low amount of MNP can actually reach cancerous cells, the inverse scattering problem arising in MNP enhanced MWI can be reliably described through a linear model [*Bellizzi et al.*, 2011, *Scapaticci et al.*, 2014]. In addition, the selective targeting of MNP in the tumor implies that the unknown inclusion is small and localized, so it is intrinsically sparse in the voxel basis.

Inspired by these peculiar features of MNP enhanced MWI for breast cancer diagnosis, in this Chapter the CS theory is exploited for the development of a novel imaging technique. More in detail, an *ad hoc* 'constrained' CS algorithm is tailored for MNP enhanced microwave breast cancer imaging. In particular, the standard CS implementation (see eq. (3.3)) is enhanced by exploiting information on the maximum concentration of contrast agent that can be achieved in human tissues [*Josephson et al.*, 1999].

In the Sections which follow, the potentialities of CS in overcoming the low-pass effect inherent to TSVD regularization, as well as in reducing the number of antennas are discussed. Both these aspects will be assessed in detail in 3D geometry, and a robustness analysis of the imaging procedure against *a priori* information will be also performed.

4.2 Basics and math of MNP enhanced MWI

A key feature of MNP enhanced microwave breast cancer imaging is the adoption of a differential measurement strategy [*Bellizzi et al.*, 2011], which allows to extract the useful signal, i.e. the signal scattered by the targeted tumor, in a 'smart' way. In more details and as schematized in fig.4.1, by exploiting the possibility of modulating the magnetic response of MNP when they are exposed to an external polarizing magnetic field (PMF), the technique requires to perform two measurements with two PMF of different

intensities [*Bellizzi et al.*, 2011, *Bucci et al.*, 2014a]. Since the PMF does not perturb the electric scenario, i.e., the breast under test, the difference of the fields gathered at the two stages of the measurement is actually associated to the magnetic contrast variation into the tumor.

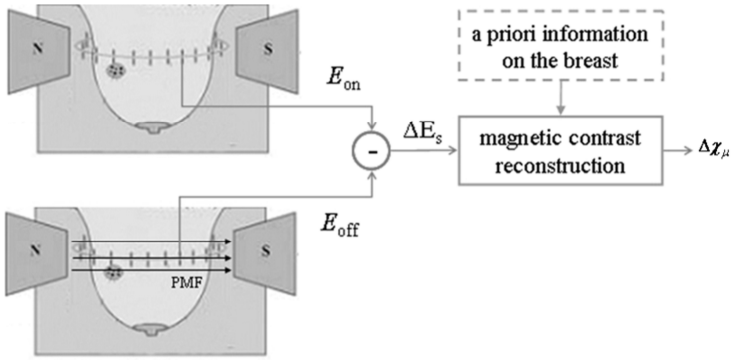

Figure 4.1. Conceptual scheme of the differential measurements procedure adopted in MNP enhanced MWI to extract the useful signal.

Due to the low magnitude of the magnetic contrast that can be induced within the tumor, it is possible to assume that the magnetic anomaly does not perturb the field due to the electric scenario. Hence, the relevant scattering phenomenon can be modeled by means of the distorted Born approximation [*Devaney and Oristaglio,* 1983].

Accordingly, by omitting some unessential factors, the $M \times M$ differential scattering matrix $\boldsymbol{\Delta E_s(r_v, r_m)}$ (M being the number of adopted probes) is given by [*Bellizzi et al.*, 2011, *Scapaticci et al.*, 2014]:

$$\boldsymbol{\Delta E_s(r_v, r_m)} = \int_{\Omega} \boldsymbol{G^{EM}(r_m, r)\, \Delta\chi_\mu(r) H_i(r, r_v) dr} = \boldsymbol{\mathcal{L}^{EM} \Delta\chi_\mu} \tag{4.1}$$

In (4.1), $\boldsymbol{\Omega}$ denotes the region hosting the breast, $\boldsymbol{r_m}$ denotes the receiving probe's positions and $\boldsymbol{r_v}$ is the vectors containing the positions of the transmitting antennas, with $\boldsymbol{v, m} = 1, \dots, M$. $\boldsymbol{G^{EM}(r_m, r)}$ is the dyadic electric-magnetic Green's function of the reference scenario, i.e., the electric field in $\boldsymbol{r_m}$ generated by an elementary magnetic source in $\boldsymbol{r}$. $\boldsymbol{H_i(r, r_v)}$ is the

magnetic incident field into the electric scenario, i.e., the magnetic field generated by an electric source located in $\boldsymbol{r_v}$ in the point $\boldsymbol{r} \in \Omega$, in presence of the breast, but without any magnetic anomaly. Due to the reciprocity principle, $\boldsymbol{G^{EM}(r_m, r) = H_i^T(r, r_v)}$, where the superscript *T* denotes the transpose matrix. Finally, $\boldsymbol{\Delta\chi_\mu}$ represents the differential magnetic contrast, i.e., the susceptibility variation due to the change of the PMF intensity between the two stages of the measurement.

As it can be seen from (4.1), the data to unknown relationship is linear, since the operator $\boldsymbol{\mathcal{L}^{EM}}$ does not depend on the unknown $\boldsymbol{\Delta\chi_\mu}$ [*Scapaticci et al.*, 2014]. Nevertheless, $\boldsymbol{\mathcal{L}^{EM}}$ depends on the electric properties of the breast under test, which obviously are not known a priori, through the electric-magnetic Green's function $\boldsymbol{G^{EM}}$ or equivalently through the magnetic field $\boldsymbol{H_i}$.

4.3 Effective recovery by ad-hoc compressive sensing approach

As previously stated, the unknown differential magnetic contrast is intrinsically sparse in the voxel basis and the relationship between data and unknowns can be considered linear. As a consequence, CS theory can be exploited as an effective and reliable procedure to accurately image the induced magnetic anomaly. Accordingly, by exploiting CS theory, the properly discretized version of the linear problem (4.1) can be solved by rewriting the optimization in (3.5) as:

$$\min_{\boldsymbol{\Delta\chi_\mu}} \left\|\boldsymbol{\Delta\chi_\mu}\right\|_{\ell_1} \textit{subject to } \left\|\boldsymbol{\mathcal{L}^{EM}\Delta\chi_\mu - \Delta E_s}\right\|_{\ell_2} < \delta \tag{4.2}$$

Notably, the cardinality of the differential data $\boldsymbol{\Delta E_s}$ can be (much) smaller than the overall number of voxels into which the investigated domain is discretized, but sufficiently larger than the number of nonzero elements of $\boldsymbol{\Delta\chi_\mu}$.

In order to exploit all the a priori information about the considered application, the standard LASSO problem in (4.2) is enhanced by considering a further constraint, that is:

$$|\Delta\chi_\mu| < |\Delta\chi_\mu|_{max} \tag{4.3}$$

In fact, the maximum concentration of MNP which can be targeted into human tissues is known from biochemical studies [*Josephson et al.*, 1999] and it is linearly related to the induced contrast variation [*Bellizzi and Bucci.*, 2013]. For this reason, it is reasonable to assume also the maximum amplitude of the magnetic contrast variation $|\Delta\chi_\mu|_{max}$ induced in the tumor.

The equation (4.3) is incorporated as a further constraint, which restricts the searching space of the unknown. As a consequence, among all solutions which are consistent with the measured data and which satisfies the upper bound on the absolute value of the magnetic contrast, one searches the sparsest one.

The addition of this constraint (4.3) represents a kind of tailored implementation of CS for MNP enhanced microwave breast cancer imaging and, as observed in the numerical analysis reported in the following, the optimization problem greatly benefits of this additional constraint.

4.4 Numerical validation

The performance of the imaging strategy herein proposed are assessed with respect to two different anthropomorphic breast phantoms, derived from magnetic resonance images and taken from the Wisconsin University Repository [*Zastrow et al.*, 2008]. In particular, the two phantoms which are taken into account are:

- a heterogeneously dense breast (ID: 070604PA2), denoted in the following as *Ph*1.

- a scattered fibroglandular breast (ID: 012204), characterized by a high percentage of adipose tissue and denoted as *Ph*2.

In both cases the breast is immersed in a homogeneous lossless matching medium, whose relative permittivity is $\varepsilon_b = 25$.

The adopted measurement configuration is depicted in fig. 4.2 and it consists of a 3 rings array of z-directed elementary dipoles working both in transmitting and receiving mode at a fixed frequency of 2 GHz. The array is centered with respect to the imaging domain and each ring, of radius 16 cm and containing 8 probes, is 3.5 cm far from the other one. Due to reciprocity, in such a configuration the total number of independent data is equal to 300 [*Bucci and Isernia*, 1997].

In this Section, the tumor is modeled as a spherical inclusion of 1 cm in size, having the same electric features of the fibroglandular tissue ($\varepsilon_{tum} = 60, \sigma_{tum} = 0.7$). In *Ph*1 the inclusion is positioned at $(0cm;\ 0cm;\ 1.2cm)$, in fibroglandular tissue, while in *Ph*2 it lies at $(0cm;\ -1cm;\ 0cm)$, across fatty and fibroglandular tissue. The transverse slices of the corresponding permittivity profiles, cutting the center of the tumors are shown in fig.4.3. A variation of the magnetic contrast between the two stages of the measurement of $|\Delta\chi_\mu| = 0.0094$ is considered. Note that, according to the experimental results reported in [*Bellizzi and Bucci*, 2013], this differential magnetic contrast corresponds to a realistic MNP concentration of about $12 mg/cm^3$. Accordingly, $|\Delta\chi_\mu|_{max}$ is chosen equal to 0.01.

The synthetic data for the described phantoms are simulated by using a full-wave forward solver based on a conjugate gradient FFT implementation of the method of moments. The imaging domain is discretized into $100 \times 100 \times 100$ square cells (each cell is about 0.05 λ in size, λ being the wavelength in the background medium), while, in order to avoid inverse crime, the inverse problem grid is discretized with $64 \times 64 \times 64$ cells (entailing a voxel size of about 0.078 λ) [*Richmond*, 1965]. Moreover, an additive Gaussian noise on the scattered field with $SNR = 20dB$ is considered.

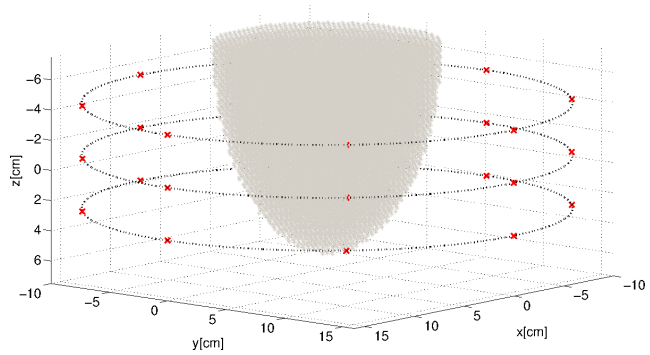

Figure 4.2. Measurement configuration adopted in the breast cancer MWI.

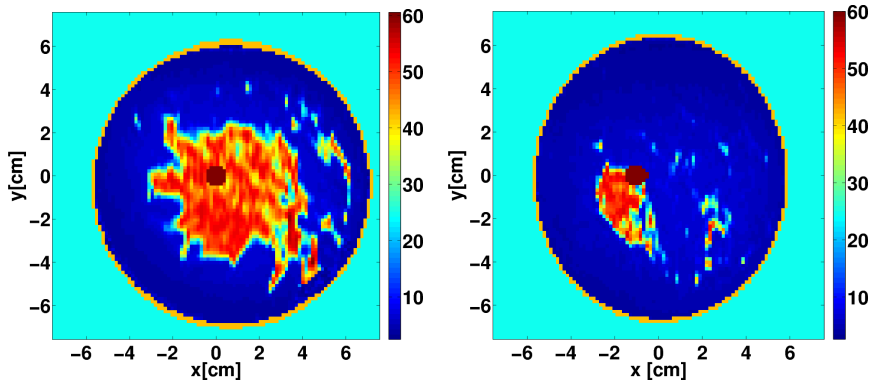

Figure 4.3 Transversal slices of the permittivity maps across the tumor for the two considered breast phantoms derived from magnetic resonance images and taken from the Wisconsin University Repository [*Zastrow et al.*, 2008]: (a) *Ph*1, (b) *Ph*2.

Note that, as highlighted also in [*Bucci et al.*, 2014a] and [*Scapaticci et al.*, 2014], the level of the SNR equal to 20dB is chosen according to realistic levels of noise which can be tolerated in MNP enhanced MWI. More precisely, in [*Bucci et al.*, 2014a] it has been demonstrated that the level of the useful differential signal is at least 70dB below the actually measured signal (at one stage of the measurement). This entails that, considering a SNR of 20dB on the differential signal corresponds a measurement requirement (in term of dynamic range) of at least 90dB, in order to reliably gather the useful signal. This requirement, although challenging, is already achieved in practice [*Bourqui et al.*, 2012].

The problem (4.2), with the addition of the constraint (4.3), is a convex one, thanks to the presence of the convex function ℓ_1 norm, and as such it can be solved by exploiting the vast theory on convex optimization.

In order to quantitatively assess the quality of the reconstructions, rather than the classical mean square error, two quantitative indexes are evaluated: the total reconstructed magnetic polarizability and the dimensional error[5]. The total reconstructed magnetic polarizability is the integral of the reconstructed magnetic contrast on the overall imaging domain [*Scapaticci et al.*, 2014], i.e.:

$$P = \sum_{n=1}^{N_c} \boldsymbol{\Delta\hat{\chi}_{\mu}}\, \Delta V \tag{4.4}$$

where $\boldsymbol{\Delta\hat{\chi}_{\mu}}$ denotes the retrieved magnetic contrast, ΔV the volume of the discretization cell, N_c the number of cells into which the domain is discretized. The correct estimation of the magnetic polarizability is of interest because it allows to appreciate the total amount of nanoparticles which is targeted, related to the tumor's size and to the achieved MNP concentration [*Bellizzi et al.*, 2011].

The dimensional error ϵ_{Δ} is defined as:

$$\epsilon_{\Delta} = \frac{V_{rec} - V_{ref}}{V_{ref}} \tag{4.5}$$

V_{rec} and V_{ref} being the volume of the reconstructed and the reference magnetic anomaly, respectively. Note that for the estimation of V_{rec}, the normalized reconstructions are thresholded at 0.3.

This metric allows to appreciate the performance of the method in reconstructing the volume of the anomaly.

4.4.1 On the choice of CS parameters

A. *The role of the constraint on the maximum amplitude of the magnetic contrast*

The addition of constraint (4.3) further regularizes the problem (4.2) by restricting the searching space of the unknown, through the exploitation of reasonable *a priori* information. As a first validation of the proposed imaging

[5]It is worth remarking that a common defined mean square error is not suitable to evaluate point-like contrast functions, like the ones dealt with in this Chapter.

method, the role played by the constraint (4.3) on the maximum amplitude of the unknown magnetic contrast is assessed. To this end, the phantom *Ph*1 is considered and then the results obtained by applying an unconstrained CS implementation and those provided by the constrained method are compared. Moreover, in this first validation the exact knowledge of the electric features of the breast is assumed.

The figure 4.4 shows the transversal slice of the retrieved absolute value of the induced magnetic contrast at $\mathrm{z} = \{0.83, 1.07, 1.30, 1.54\}\, cm$. As it can be seen, the presence of the additional constraint (4.3) is crucial to obtain an accurate reconstruction of the inclusion. As a matter of fact, the unconstrained CS solution, while still allowing a satisfactory localization of the target, highly overestimates the amplitude of $|\boldsymbol{\Delta\chi_\mu}|$ (0.08 versus 0.0094) while underestimates the dimensions (see panel (a) of fig. 4.4). This is confirmed also by the high value of the dimensional error ($\epsilon_\Delta = 0.87$).
Such a circumstance can be attributed to the maximal sparsity requirement, which concentrates the overall magnetic anomaly in much fewer voxels than in actual ground truth.

On the contrary, the constrained solution (fig. 4.4(b)) appears more accurate, both qualitatively and quantitatively (in this case $\epsilon_\Delta = 0$).

The exploited a priori knowledge of the level of induced contrast represents an upper bound for the case at hand. More precisely, the maximum contrast value of 0.01 is associated to the maximum (optimistic!) amount of nanoparticles that can be targeted. What can happen in practice is that a lower amount on MNP (and of the induced contrast) is achieved in the tumor, but for the way in which the problem is formulated, this would be still a possible solution of the implemented algorithm. Nevertheless, by taking into account that the knowledge of $|\boldsymbol{\Delta\chi_\mu}|_{max}$could be not precise, it has been assessed how the method works when an error in the order of $\pm$25% on the expected maximum contrast function is present, in order to test the robustness of constrained CS with respect to a wrong setting of constraint (4.3). From this numerical analysis no significant deterioration has been observed in the final reconstruction. The tumor is still localized and its

dimension is correctly retrieved, as confirmed by the dimensional index computed when considering an error on $|\boldsymbol{\Delta\chi_\mu}|_{max}$ of 25% and −25% (ϵ_Δ = 0.22 and ϵ_Δ = 0.45, respectively).

B. On the choice of δ parameter

The δ parameter depends on many factors, namely, the level of required precision, the amount of noise on data and the model error introduced by the estimation of $\boldsymbol{G^{EM}(r_m, r)}$. Of course, the larger the expected model error and noise on data, the larger the parameter δ.

The choice of this parameter is not-trivial and for this reason the guidelines described in Section 3.2.2.A are followed. More in detail, the optimal δ is chosen through an iterative optimization procedure as the smallest value which allows to obtain a feasible and localized solution. In fact, it is observed that the smallest δ which allows a feasible solution, provides a reconstruction with randomly located high contrast voxels inside the domain of interest (while the searched target is known to be localized and sparse).

As an example, in fig 4.5 a slice cutting the center of the tumor of *Ph*1 at $z = 1.2\,cm$ is reported, when choosing the smallest δ which provide a feasible solution. As it can be seen, although the target of interest is detected, there is the presence of many randomly located voxels different from zero, which are a clear indication of a wrong setting of δ.

4.4.2 Analysis of robustness against a priori information on the breast under test

The relationship between the differential scattered field and the induced magnetic contrast, reported in (4.1), while being linear, depends on the electric properties of the breast under test through the electric-magnetic Green's function $\boldsymbol{G^{EM}}$ and the magnetic field $\boldsymbol{H_i}$. In realistic cases, the exact knowledge of the electric scenario (and of the corresponding magnetic field inside it) is not available.

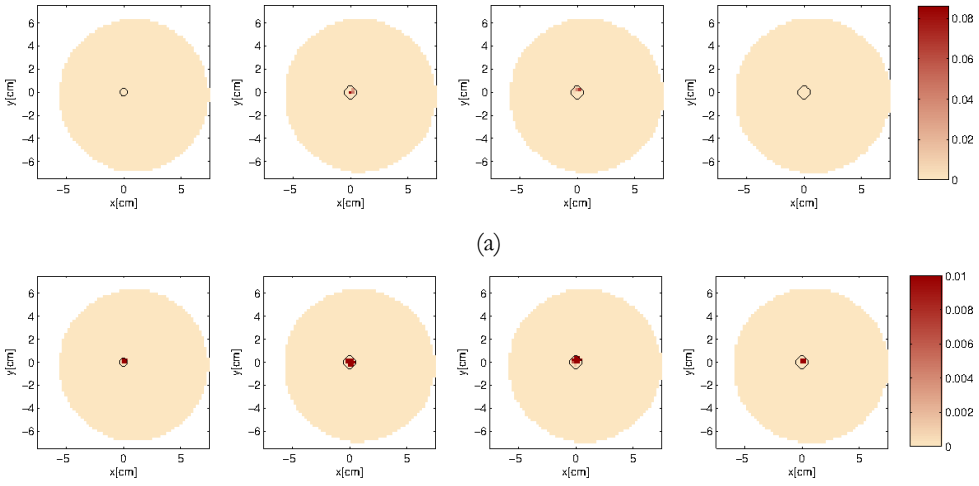

Figure 4.4. Numerical assessment of CS inspired approach for MNP enhanced MWI. Transversal slices of the retrieved absolute value of the induced magnetic contrast (*Ph1*): (a) via unconstrained implementation (b) by means of the constrained one. The black line indicates the actual contour of the tumor.

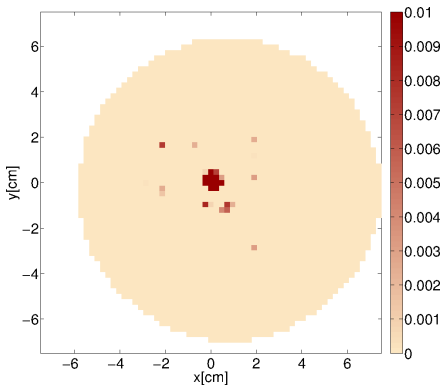

Figure 4.5 Numerical assessment of CS inspired approach for MNP enhanced MWI. Transversal slice of the reconstructed magnetic contrast in when setting $\delta < \delta_{optimal}$.

Accordingly, reference scenarios with different degrees of accuracy are usually considered [*Scapaticci et al.*, 2014]. In this Section the role played by *a priori* information on the breast under test on the constrained CS algorithm is evaluated. In particular, both *Ph*1 and *Ph*2 are taken into account and three reference scenarios are assumed, namely:

- exact breast, that is the ideal (not realistic) case in which the breast under test is completely characterized;
- accurate representation of the breast, in which the breast morphology is supposed exactly known, while the electric properties of the

adipose and fibro-glandular tissues are supposed to be constant and set according to the average values provided in [*Lazebnik et al.*, 2007].

- empty system filled by a medium having the same properties as the coupling liquid. In this case no a priori information on the breast is assumed.

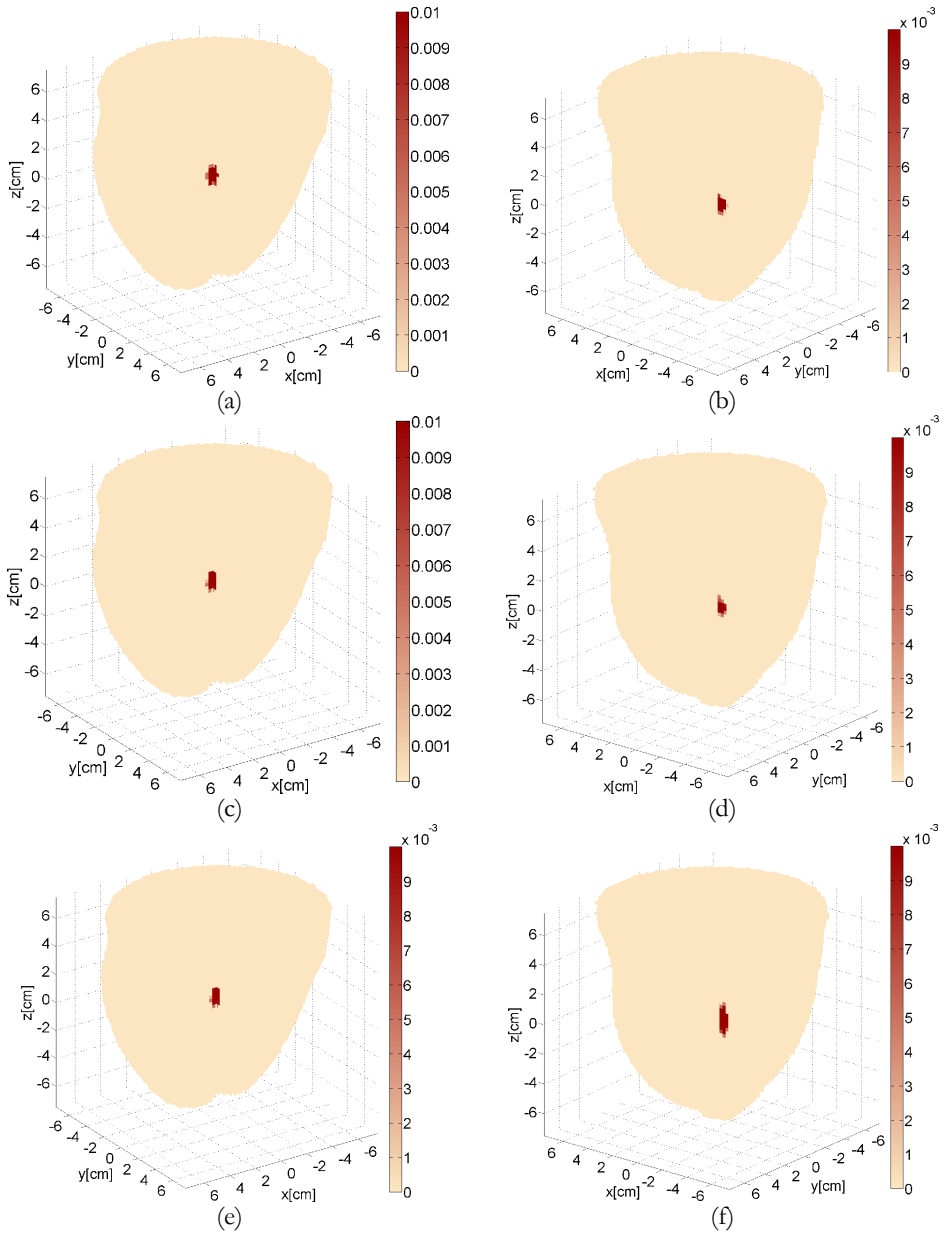

Figure 4.6. Numerical assessment of CS inspired approach for MNP enhanced MWI. 3D Reconstructions of the absolute value of the induced magnetic contrast. (a) *Ph1* and exact breast as reference scenario; (c) *Ph1* and accurate reference breast; (e) *Ph1* and empty system as reference profile; (b), (d) and (f) same as (a),(c) and (e) but for *Ph2*.

As mentioned in the Section 4.4.1.B, the fidelity of the reference scenario with the true one, affects the choice of δ. By following the above detailed rule, it is assumed $\delta = 0.1\|\Delta \boldsymbol{E_s}\|_{\ell_2}$, when the exact breast is considered, $\delta = 0.3\|\Delta \boldsymbol{E_s}\|_{\ell_2}$, when the approximated breast is taken into account and $\delta = 0.8\|\Delta \boldsymbol{E_s}\|_{\ell_2}$ when no a priori information is available. Corresponding reconstructions for both *Ph*1 and *Ph*2 are reported in Fig.4.6. As can be seen, also with no a priori information on the breast under test, constrained CS is able to provide accurate results, both in terms of detection and of quantitative imaging.

For the considered examples, the values of *P* and ϵ_Δ are reported in Table IX. As can be seen, in all cases the estimated values of the magnetic polarizability are close to the actual one (4.8 mm^3, obtained by multiplying the actual tumor's volume times the magnetic contrast $|\Delta \boldsymbol{\chi_\mu}| = 0.0094$ induced by the assumed MNP concentration). The dimensional error also assumes satisfactory values, and in most cases it is close to zero, confirming that the constrained CS is able to reconstruct with high accuracy the volume of the anomaly. By considering the results presented in this Section, in the following the analysis will be limited to the assumption of the empty system.

breast	***exact***		***accurate***		***Empty system***	
	P [mm^3]	ϵ_Δ	*P* [mm^3]	ϵ_Δ	*P* [mm^3]	ϵ_Δ
Ph2	5.27	0	3.81	0.25	4.08	0.2
Ph1	5.7	0.12	4.55	0.025	3.75	0.25

Table IX. Numerical assessment of CS inspired approach for MNP enhanced MWI: polarizability and volumetric errors

4.5 CS inspired imaging strategy vs TSVD

As previously discussed in the introduction, the use of CS theory also allows to significantly reduce the number of probe antennas and to retrieve 'high resolution' reconstructions with respect to alternative techniques.

To fix ideas, in this Section performances of the CS inspired algorithm will be compared to those obtained by means of a TSVD procedure [*Bertero*, 1989], previously considered in [*Scapaticci et al.*, 2014].

As a first comparison between the two techniques, it is worth recalling that in [*Scapaticci et al.*, 2014] the TSVD fails in retrieving the actual magnetic polarizability when no a priori information on the breast is assumed. On the contrary, from Table IX and figs. 4.6(e)-(f) one can observe that the constrained CS succeeds in the same conditions.

4.5.1 Reduction of the numbers of measurements

In microwave medical imaging, the minimization of the number of adopted probes plays a crucial role. As a matter of fact, this would allow to minimize costs and dimensions of the system, as well as measurement time. Moreover, reducing the system complexity has a particular relevance for MNP enhanced MWI, wherein data are acquired through a two-stage differential measurement procedure. In fact, the acquisition has to be performed quickly enough to avoid any variation of the electric scenario between the two stages and this is obviously a challenging goal when the number of probes is very large.

In the following, the possibility of reducing the number of probes while preserving the accuracy of the tumor reconstruction is assessed. In particular breast *Ph*2 is considered and a measurement configuration constituted by only 12 probes on 3 rings (4 probes per ring, arranged as depicted in fig. 4.7(a)) is adopted. In this way, the total number of independent data is equal to 78 [*Bucci and Isernia*, 1997].

Results reported in fig. 4.7 demonstrate that constrained CS (panel (b)) allows a reliable and accurate recovery also with very few antennas. On the contrary, the TSVD reconstruction (reported in panel (c)) appears less accurate. This is due to the low amount of available data, which causes the occurrence of grating lobes. These observations are corroborated by the values of retrieved polarizability and dimensional error, computed for both the CS reconstruction ($P = 3.82 mm^3$ and $\epsilon_\Delta = 0.22$) and the TSVD one ($P =$

$9.14mm^3$ and ϵ_Δ = 3.15). Note that for the computing of ϵ_Δ, the normalized TSVD images are thresholded at -3dB.

Finally, it is worth noting that, due to the fact that the TSVD provides the minimum energy solution, the presence of grating lobes causes a considerable underestimation of the maximum value of the magnetic contrast.

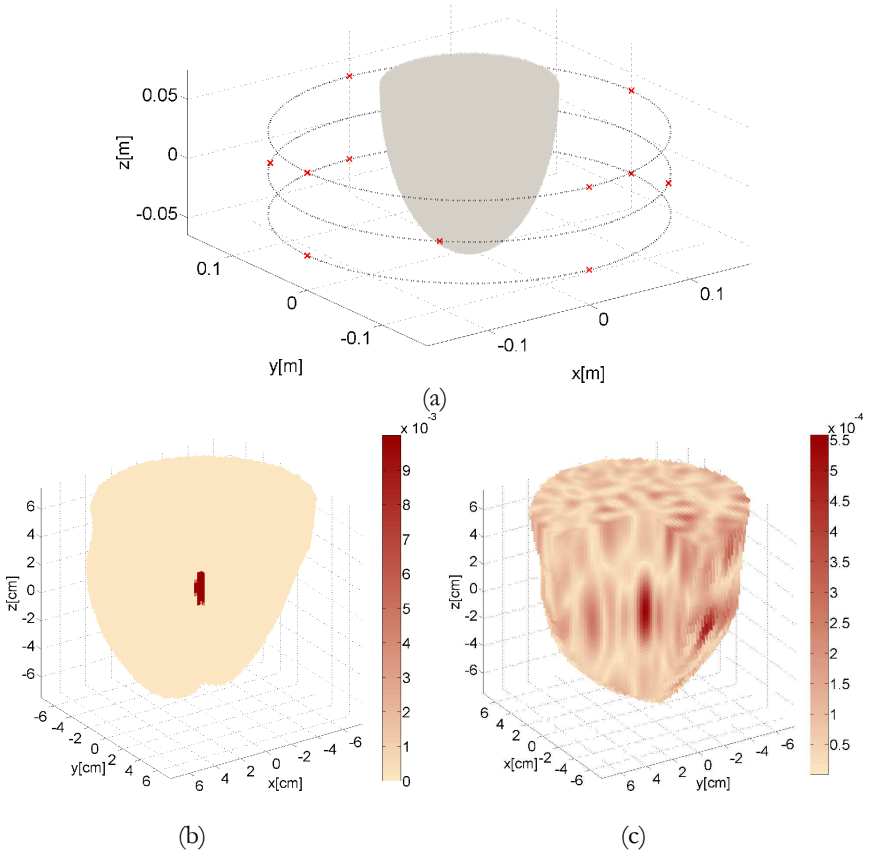

Figure 4.7. Numerical assessment of CS inspired approach for MNP enhanced MWI. 3D Reconstructions of the absolute value of the induced magnetic contrast exploiting 12 probing and receiving antennas and considering the background as reference profile. (a) New measurements configuration; (b) reconstruction via CS and (c) via TSVD.

4.5.2 Super-resolution imaging

In cancer imaging, the possibility of recovering with a high resolution the boundaries of the cancer is extremely important. As a matter of fact, the shape of the inclusion is associated to the degree of malignancy of the cancer, the more irregular the border the more aggressive the disease.

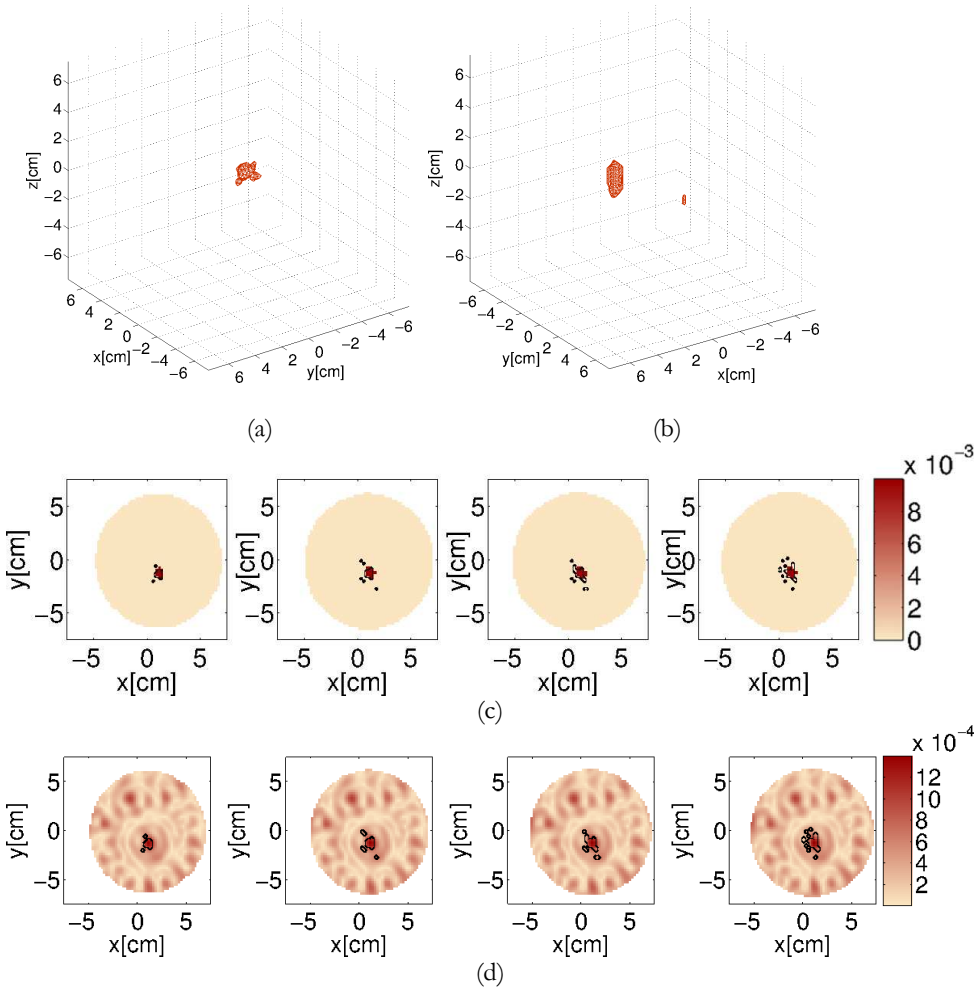

Figure 4.8. Numerical assessment of CS inspired approach for MNP enhanced MWI. 3D Reconstructions of the absolute value of the induced magnetic contrast via CS (a) and via TSVD (b) (thresholded at -3dB). Transversal slices of the reconstructed differential magnetic contrast obtained via CS (c) and via TSVD (d).

Accordingly, in order to appreciate the potential of the method in providing super resolution images, the case in which the tumor is modeled as an irregular structure (the actual magnetic polarizability P is equal to $8.69 mm^3$) is analyzed. In particular, phantom *Ph*1 and the measurement configuration reported in fig .4.2 are considered. Again, for the sake of comparison, TSVD inversion is also performed. Corresponding results are shown in fig. 4.8. Panels (a) and (b) report the 3D reconstructions obtained via CS and TSVD, respectively. Panels (c) and (d) show the transversal slices at $z = \{-0.35, -0.12, 0.12, 0.35\}\ cm$ in which the tumor is located, and the actual contour of the cancer, which is superimposed as a black line. Such

reconstructions clearly demonstrate that CS outperforms TSVD as far as resolution is concerned, as it allows to appreciate with a satisfactory accuracy the irregular shape of the cancer, which is not possible from TSVD images. Moreover, the better quality of CS reconstruction with respect to the TSVD one is also witnessed by value of P and ϵ_Δ equal respectively to $6.78 mm^3$ and 0.2 for the CS reconstruction, $11.2 mm^3$ and 0.26 for the TSVD reconstruction.

4.6 Conclusions and discussion

Magnetic nanoparticles have been recently proposed as contrast agent in breast cancer MWI. Once properly functionalized, MNP are able to concentrate in cancerous cells in a selective way, hence their adoption allows to face the cancer imaging as the reconstruction of a magnetic contrast into a purely electric scenario. In such a framework, the adoption of an effective and robust imaging algorithm represents a key-point for an accurate and specific breast cancer diagnosis.

By relying on the fact that in MNP enhanced breast cancer MWI the problem to be solved is linear, and the unknown magnetic contrast is intrinsically sparse, an *ad hoc* CS algorithm has been developed, by exploiting the knowledge of the maximum concentration of MNP that can be targeted in human tissues.

In particular, the potentiality of the CS approach is investigated in 3D geometry, as well as the robustness of the imaging procedure with respect to the lack of *a priori* information of the breast under test in order to assess its diagnostic performance in realistic conditions.

The numerical results have shown that, provided that the parameter δ is properly chosen, one can accurately image cancerous inclusions also in absence of any patient-specific information. On the other hand, an even rough knowledge of the electric properties of the breast can improve the CS results and this pushes towards a parallel line of research that is quantitative MWI techniques [*Winters et al.*, 2009, *Scapaticci et al.*, 2015], in order to retrieve the (approximate) distribution of the electric properties of patient's breast.

As far as the comparison between the proposed CS strategy and TSVD imaging procedure is concerned, the main results of the analysis carried out in this Chapter can be summarized as follows.

- As compared to the TSVD procedure, the CS inspired approach allows the achievement of reliable results with a smaller amount of data, involving a significant reduction of the number of antennas and the measurement apparatus complexity;
- CS allows a more accurate imaging of the cancer in term of achievable resolution. In particular, the possibility to obtain a sort of super-resolution is a crucial feature of the proposed imaging technique, as the shape of the inclusion is associated to the degree of malignancy of the cancer.

Besides these interesting advantages, it is worth mentioning that the proposed inversion technique involves the solution of a constrained optimization problem, which relies on an iterative procedure, and thus more computationally demanding than TSVD. To overcome such a drawback, one could develop a step-wise procedure, in which the TSVD is first adopted to detect and localize the tumor, while the CS is explored to refine the reconstruction and pursue a high resolution image. Note that the first step can be performed in quasi real time, since the computationally intensive part of the algorithm (which involves the building and the SVD computation of the scattering operator) can be moved offline [*Scapaticci et al.*, 2014]. Then, once the tumor is detected and localized, it is possible to reduce the imaging domain in the CS step and this allows a considerable reduction of the computational burden.

Finally, although the assessment carried so far has been based on the accurate full-wave modeling of the electromagnetic phenomena and the experimentally measured response of MNP at microwaves, future work needs to validate the proposed technique with experimental data. Unfortunately, due to the fact that magnetic nanoparticles enhanced microwave breast cancer imaging has been only recently proposed and numerically validated, there is not yet the availability of experimental data and first experimental proofs-of-concept are currently ongoing [*Helbig et al.*, 2014, *Bucci et al.*, 2014b]. Such first

experiments are mainly aimed at the simple detection of the differential signal due to magnetic nanoparticles and they have been not designed for imaging purposes.

5

A compressive sensing approach for subsurface microwave imaging of non-weak buried targets

5.1 Introduction

Nowadays, tomographic approaches represent some of the most promising candidates for accurate inspections and explorations of the underground [*Crocco and Soldovieri*, 2011, *Daniels*, 2004, *Pastorino*, 2010, *Persico*, 2014, *Soldovieri and Crocco*, 2011], thanks to the capability of quantitatively characterizing buried targets and scenarios that are not directly accessible with other sensing techniques. Moreover, microwave imaging allows to obtain reconstructions that are more reliable and readable than those achieved by using standard GPR data processing, which require human expertise and may show high probability of false alarms.

However, as discussed in the Introduction, such a goal requires to cope with several difficulties. First of all, the underlying inverse scattering problem is both nonlinear and ill-posed. As a consequence, when dealing with the problem in its full non linearity, both local and global optimization techniques cannot assure the convergence to the ground-truth.

On the other side, when a weak scattering approximation is adopted, one is usually unable to retrieve electromagnetic properties of the targets owing the impossibility to fulfill the model assumptions in any actual instance. As a result, linearized inversion strategies based on BA, so far exploited in GPR tomographic approaches, has been safely used just to perform target localization [*Crocco and Soldovieri*, 2003;*Cui et al.*, 2001, *Habashy et al.*, 1993, *Soldovieri et al., 2007*]. Moreover, neglected higher order interactions related to the adoption of weak scattering models may give raise to artifacts appearing

as false targets in the images. This limitation is more and more pronounced in the case of GPR surveys where data are collected just in reflection mode [*Bucci et al.*, 2001b; *Leone and Soldovieri*, 2003].

Moreover, even if the model assumptions (f.i. weak scatterers) are fulfilled, linearized models are unable to achieve quantitative reconstructions in the case of single frequency aspect limited measurement. Indeed, the relevant operator mapping the data-to-unknown relationship shows filtering properties which entail, among the other, a band-pass reconstruction (along the in-depth direction) of the actual targets' profile [*Di Donato and Crocco*, 2015, *Leone and Soldovieri*, 2003].

Concerning the ill-posedness of the problem, the regularization strategies usually adopted in least square optimization unfortunately allow to recover only an approximated, i.e. low-energy or smooth, version of the actual profile [*Bertero and Boccacci*, 1998, *Pastorino*, 2010, *Persico*, 2014, *Soldovieri and Crocco*, 2011].

In this respect, both the CS and VE, introduced in the previous Chapters, can come into play to counteract ill-posedness and non-linearity, respectively. In addition, as explained in Section 1.6, VE allows also to counteract the fact that both primary sources and measurement probes cannot be located inside the soil, so that just aspect limited data can be used.

In the following, the above mentioned frameworks are mainly applied with respect to surface GPR surveys for quantitative characterization of dielectric targets and structures, by considering data measurement under a multiview-multistatic configuration[6] and single-frequency data, which avoids the need of modelling frequency dispersivity of the soil.

[6] Although this is not the usual arrangement adopted in the conventional GPR systems, it is worth noting that several emerging facilities have been developed and exploited in the last years [*Bradford*, 2008; *Francese et al.*, 2009; *Gerhards et al.*, 2008];

5.2 Imaging non-weak and extended buried object

With respect to the geometry considered in Section 1.1, the presence of the air-soil interface has now to be taken into account. As shown in fig. 5.1, the investigation domain Ω is placed at a given depth below it and it is probed by means of antennas located on the curve Γ along the x-axis, placed above the air-soil interface at given height. The antennas are modelled as filamentary currents oriented along the invariance axis y and again a multiview-multistatic measurement configuration is assumed.

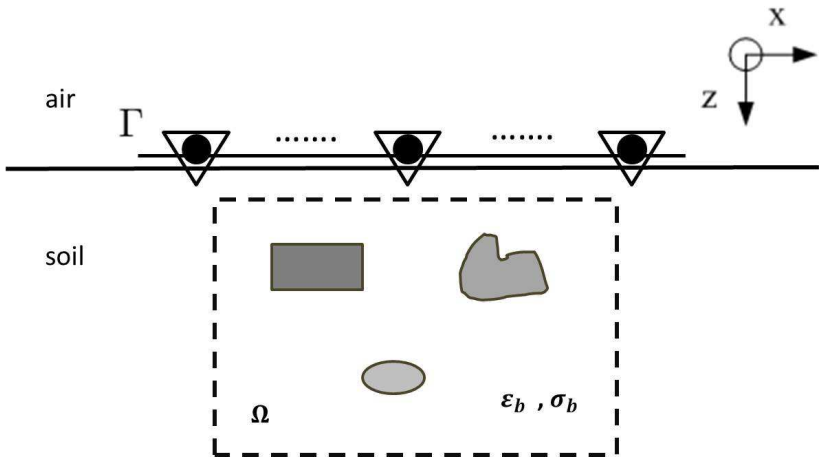

Figure 5.1. The geometry of the 2D subsurface problem and the adopted measurement configuration. The black circles and white triangles represent two or more transmitting and receiving antennas in a surface-GPR acquisition.

Under the above assumptions and assuming a 2D geometry and electric field polarized along y, the equations (1.2) and (1.3) governing the scattering phenomenon are rewritten by taking into account the presence of the interface, i.e.:

$$E_s^{(v)}(\boldsymbol{r}) = {k_b}^2 \int_{\Omega} G_{12}(\boldsymbol{r},\boldsymbol{r}')\,\chi(\boldsymbol{r}')E^{(v)}(\boldsymbol{r}')d\boldsymbol{r}' \qquad \boldsymbol{r} \in \Gamma \tag{5.1}$$

$$E^{(v)}(\boldsymbol{r}) = E_i^{(v)}(\boldsymbol{r}) + {k_b}^2 \int_{\Omega} G_{22}(\boldsymbol{r},\boldsymbol{r}')\,\chi(\boldsymbol{r}')E^{(v)}(\boldsymbol{r}')d\boldsymbol{r}' \qquad \boldsymbol{r} \in \Omega \tag{5.2}$$

where $G_{12}(\boldsymbol{r},\boldsymbol{r}')$ is the external Green's function for the half space case, i.e., the field radiated in the medium 1 (the air) by an elementary source placed in the medium 2 (the soil), while $G_{22}(\boldsymbol{r},\boldsymbol{r}')$ is the internal Green's function for the considered scenario, i.e., the field radiated in the medium 2 (the soil) by an elementary source placed in the same medium.

With respect to eqs. (1.2) and (1.3), in the above equations the half space Green's functions are now considered [*Chew*, 1995]. These latter can be computed by solving Green-Sommerfeld integrals by means of 1-D Fast Fourier transform [*Crocco and Soldovieri*, 2003].

A. A linear approach for quantitative subsurface imaging based on VE

As described in Section 1.6., the design of circular symmetric VE allows to introduce an effective field approximation and to linearize the scattering eq. (5.1). In case of subsurface survey both the design equation (1.8) and the field approximation (1.12) must be readapted by taking into account the presence of the interface between air and soil.

More in detail, the design equation for the VE is recast as:

$$\sum_{v=1}^{N} {\alpha_v}^p \, E_s(\vartheta_v, \boldsymbol{r}) = G_{12}(\boldsymbol{r}, \boldsymbol{r_p}) \tag{5.3}$$

In particular, its solution is exploited in order to image the support indicator (see eq. 1.10) and choose P evenly spaced pivot points with respect to build the multipivot experiments. Then, for each VE, the data equation is recast and the approximated total field is computed according to:

$$\mathcal{E}(\boldsymbol{r}, \boldsymbol{r_p}) \approx \mathcal{E}_i(\boldsymbol{r}, \boldsymbol{r_p}) + LP\left[G_{22}(\boldsymbol{r}, \boldsymbol{r_p})\right] \tag{5.4}$$

where $\mathcal{E}$ and $\mathcal{E}_i$ are the virtual total and incident field (see (1.6) and (1.7)).

Note that in the design equation (5.3) the original scattered field is recombined in order to fit at the measurements positions $\boldsymbol{r} \in \Gamma$, the field radiated in the air by an elementary source placed in the soil. On the contrary,

in the field approximation (5.4), the unknown $\mathcal{E}$ is approximated in each $\boldsymbol{r} \in \Omega$ considering the field radiated in the soil by an elementary source placed in the same medium.

B. A 'fictitious measurements' strategy for aspect limited data

As discussed in Section 1.6, the achieved field conditioning allows to predict the value of the field in locations other than the measurement points, so that one can exploit a number of additional equations corresponding to 'fictitious measurements' [*Di Donato and Crocco*, 2015].

Accordingly, let us consider a fictitious curve Γ^* (complementary to Γ) which surrounds the investigation domain and allows to locate measurement points into the soil. The value of the (virtually measured) scattered field at these fictitious locations would be given by $G_{22}(\boldsymbol{r_r}^*, \boldsymbol{r_p})$, where $\boldsymbol{r_r}$ and $\boldsymbol{r_r}^*$ denote the actual and the fictitious measurement points, respectively, as fictitious measurements are placed in the lower halfspace. According to the above, the virtual data equation can be suitably rewritten as:

$$k_b{}^2 \int_{\Omega} \tilde{G}_b(\boldsymbol{r}, \boldsymbol{r}')\, \chi(\boldsymbol{r}') \mathcal{E}(\boldsymbol{r}', \boldsymbol{r_p}) d\boldsymbol{r}' = \begin{cases} \mathcal{E}_s(\boldsymbol{r}, \boldsymbol{r_p}) \text{ if } \boldsymbol{r} = \boldsymbol{r_r} \in \Gamma \\ G_{22}(\boldsymbol{r}, \boldsymbol{r_p}) \text{ if } \boldsymbol{r} = \boldsymbol{r_r}^* \in \Gamma^* \end{cases} \tag{5.5}$$

To take into account the dependence of the kernel of (5.5) from the different kind of measurement (the actual ones on surface and the fictitious one in the underground), the Green's function is defined as:

$$\tilde{G}_b(\boldsymbol{r}, \boldsymbol{r}') = \begin{cases} G_{12}(\boldsymbol{r}, \boldsymbol{r_p}) \text{ if } \boldsymbol{r} = \boldsymbol{r_r} \in \Gamma \\ G_{22}(\boldsymbol{r}, \boldsymbol{r_p}) \text{ if } \boldsymbol{r} = \boldsymbol{r_r}^* \in \Gamma^* \end{cases} \tag{5.6}$$

that stands for the external or the internal Green's function depending on the measurement at hand. In fig. 5.2, a sketch of the fictitious receivers, placed over the fictitious curve denoted with Γ^*, is depicted.

More in detail, two vertical and one horizontal dummy arrays are added with a total of F receivers on Γ^*. For the horizontal one both its length L_x and number of antennas are set equal to the actual array and it is placed at depth z_d from the interface. The vertical virtual arrays with length z_d are placed perpendicular to the actual array and the number of antennas is set in such a way that the distance between the antennas is about $0.5\ \lambda$.

As discussed into Section 1.6.1, since the analytical prolongation (5.5) works fine outside the scatterers, a convenient choice of z_d amounts to place the fictitious probes approximately at the same distance of that between the investigated domain and the actual probes.

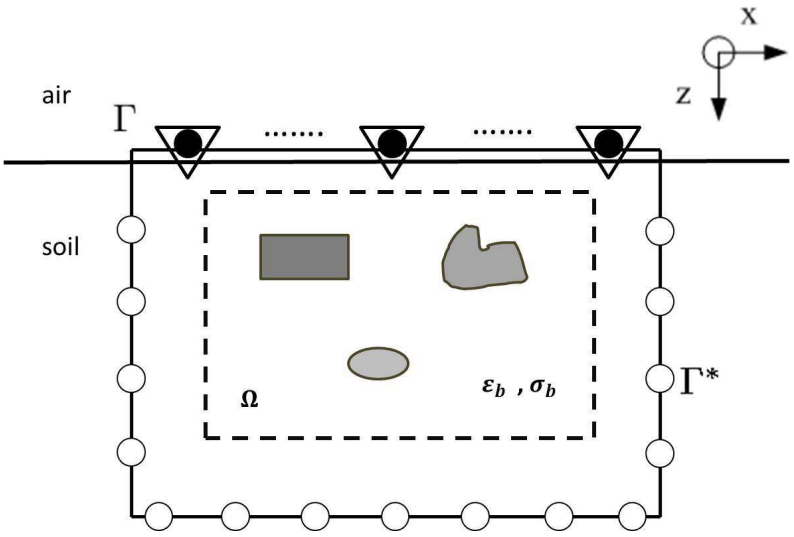

Figure 5.2. The virtual measurements setup. The black and white circles refer to actual and fictitious measurements, respectively, while the white triangles denote the transmitters.

C. A Compressive Sensing based approach

Once the problem is linearized and a number of additional equations corresponding to 'fictitious measurements' are added, the subsurface imaging can be carried out by considering the CS approach described in Section 3.2.1.C. In fact, in many cases dealing with real life application the unknown contrast profile can be assumed to be piecewise constant, which entails a sparse representation in terms of step functions.

According to eq. (5.5), the data vector with dimension $K = (M + F) \times P$ contains the M measured scattered fields and the F fictitious ones arising in the P virtual scattering experiments, while the matrix which relates the

unknown to data vector with dimension $K \times N_c$ is obtained by considering the linear approximation and additional fictitious measurements.

5.3 Numerical assessments

To give a proof of the performances achievable by means of the proposed method, three numerical examples concerned with GPR surveys are presented. In particular, it will be shown how field conditioning achieved by properly designed VE (including fictitious measurements) and CS regularized inversion (exploiting sparseness of the gradient of the unknown) allow to achieve quantitative imaging results.

The first example consists of a wet soil whose electromagnetic properties exhibit a 5% random variation around the average values ε_b = 9 and σ_b= 50 mS/m. It embeds two targets, the first one, having circular cross-section, is a stone (ε = 6) while the second one is a plank (ε = 3) with a square cross-section. The rectangular imaging domain is $0.9 \times 0.3\, m^2$ wide (which corresponds to $3.6\,\lambda \times 1.2\,\lambda$) and is discretized into 78×26 cells. The antennas ($N = M = 12$), located at the air-soil interface, are evenly spaced of about $\lambda/2$ and the working frequency is 400MHz.

In the second example, two rectangular lossy targets with permittivity values representative of glass (ε_1 = 8, σ_1 = 0) and porcelain (ε_2 = 6.5, σ_2 = 0 respectively) are considered. The two objects are embedded in a dry soil whose electromagnetic. properties exhibit a 5% random variation around the average values ε_b = 3 and σ_b = 20 mS/m. Even in this case, the working frequency is 400MHz. The rectangular imaging domain is $0.9 \times 0.3\, m^2$ wide (which corresponds to $2.1\,\lambda \times 0.7\,\lambda$) and it is discretized into 44×22 cells. The probing array is made of $N = M = 8$ evenly spaced antennas.

The third example consists of three rectangular targets having the same size and different electromagnetic characteristics, buried in a dry soil with relative permittivity ε_b = 4 and conductivity σ_b = 1 mS/m. The first target is a void (ε_1 = 1, σ_1 = 0), the second target is representative of a plastic mine

($\varepsilon_2 = 2.5, \sigma_2 = 0$) and the third has the dielectric properties of a stone ($\varepsilon_3 = 6, \sigma_3 = 1$m S/m). The working frequency is 400MHz. The imaging domain is a square region of side 1m (about 2.7 λ), discretized into 64×64 cells. The probing array is made of $N = M = 8$ evenly spaced antennas.

The scattered field data are two different signal-to-noise ratio levels, SNR=30dB and SNR=10dB.

To appraise the accuracy of the results, two error reconstruction metrics are used. The first one is the usual mean square error, which represent a global and synthetic parameter. In order to evaluate the fidelity of the reconstruction of the electromagnetic properties of a single object is defined the following error, i.e.:

$$err_{max} = \frac{\|\chi\|_\infty - \|\tilde{\chi}\|_\infty}{\|\chi\|_\infty} \tag{5.7}$$

where χ is the actual contrast profile, $\tilde{\chi}$ the estimated one and $\|\cdot\|_\infty$ the uniform norm.

As described in the previous section, the inversion procedure consists of three steps. In the first step, the solution of eq. (5.3) is exploited in order to image the support indicator that, in the case of SNR = 30dB, is shown in figs. 5.3(a), 5.4(a) and 5.5(a) for the three scenarios, respectively. Then, for each designed VE, the data equation is recast and the approximated total field is computed according to eq. (5.4).

The second step takes advantage of the achieved field conditioning by means of the fictitious measurements. For the three scenarios at hand, the resulting fictitious measurement configurations are shown in figs. 5.3(b), 5.4(b) and 5.5(b), respectively. In particular:

- for the first scenario $z_d = -0.5$m, $L_x = 1.5$m and F = 20;
- for the second scenario $z_d = -0.6$m, $L_x = 1.5$m and F = 12;
- while for the third one $z_d = -1.5$m, $L_x = 1.5$m and F = 20.

The last step is the optimization task via CS by means of eq.(3.7), in which the tolerance parameter δ is set following the guideline in Section 3.2.2.A.

To analyze the achievable performances of the method, in the second and third examples the obtained results are compared with the BA usually adopted in tomographic GPR imaging [*Ambrosanio and Pascazio*, 2015, *Soldovieri and Crocco*, 2011]. In particular, the simulated data are also processed by using a BA-CS approach, in particular eq. (3.7), but building the data-unknown matrix $\boldsymbol{A}$ using the original incident fields and noisy scattered ones instead of the proposed approach based on VE.

As it can be seen in figs. 5.3-5.5, the results confirm the extended validity range of the proposed linearization based on field conditioning, as well as the remarkable advantage of using this latter in conjunction with CS, especially in presence of a large amount of noise in the processed data. As a matter of fact, this allows obtaining reliable quantitative results both for permittivity and conductivity values (see Tables X and XI), outperforming the BA.

Finally, in the third example, a performance analysis reducing the overall numbers K = 644 of processed data is also carried out in the case of VE-CS. In particular, the data reduction is achieved with a routine that extract uniformly random samples of the initial data-set. Figure 5.5 (which show only the retrieved permittivity, being the retrieved conductivity negligible) summarizes the results obtained in this case, confirming the robustness of the CS-based procedures. Of course, for the larger noise level (SNR=10dB) and undersampling rate (RF = 10 and K = 64) results are slightly worse in particular for the deepest target.

In conclusion, these numerical results show the method is able to perform satisfactory characterization of buried targets having different dielectric properties in lossy soils, significantly outperforming the results achievable with the 'state of the art' standard approaches.

These preliminary results, meant to address the feasibility of the overall strategy in the subsurface imaging, encourage future work towards 3D tomographic imaging and for testing the reconstruction capability against experimental data-set.

	SNR=30dB		***SNR=10dB***	
	err	err_{max}	*err*	err_{max}
BA-CS	1.42	0.62	1.39	0.65
VE-CS	0.64	0.02	0.65	0.04

Table X. Numerical assessment of VE-CS approach for subsurface MWI: error metrics for the second example.

	SNR=30dB		***SNR=10dB***	
	err	err_{max}	*err*	err_{max}
BA-CS	0.82	0.7	0.83	0.55
VE-CS	0.70	0.24	0.82	0.25
VE-CS(RF=4)	0.69	0.35	0.84	0.38
VE-CS(RF=10)	0.71	0.40	0.85	0.48

Table XI. Numerical assessment of VE-CS approach for subsurface MWI: error metrics for the third example.

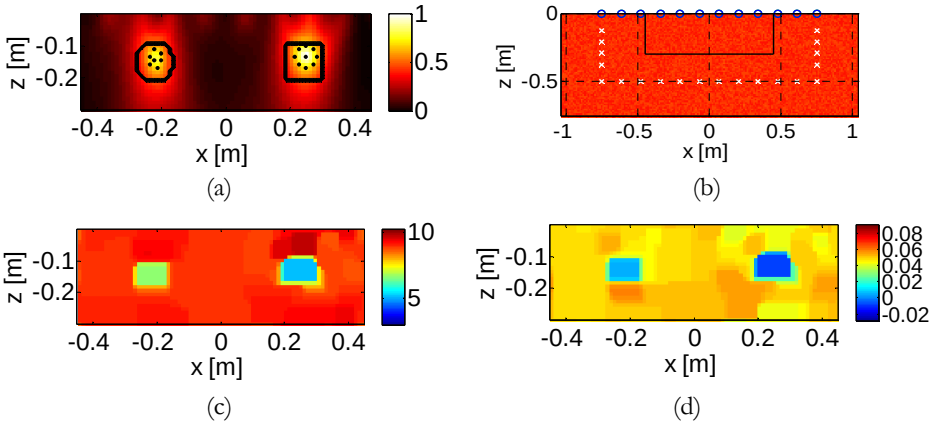

Figure 5.3 Numerical assessment of VE-CS approach for subsurface MWI. Example 1. (a) Logarithmic map of the LSM indicator with superimposed the pivot points and the contour of the reference profile, (b) virtual measurements setup. (c)-(d) Permittivity and conductivity of the retrieved profile by means of VE-CS ($\hat{\delta}$= 0.18) for SNR=30dB (*err* = 0.45, err_{max} = 0.29).

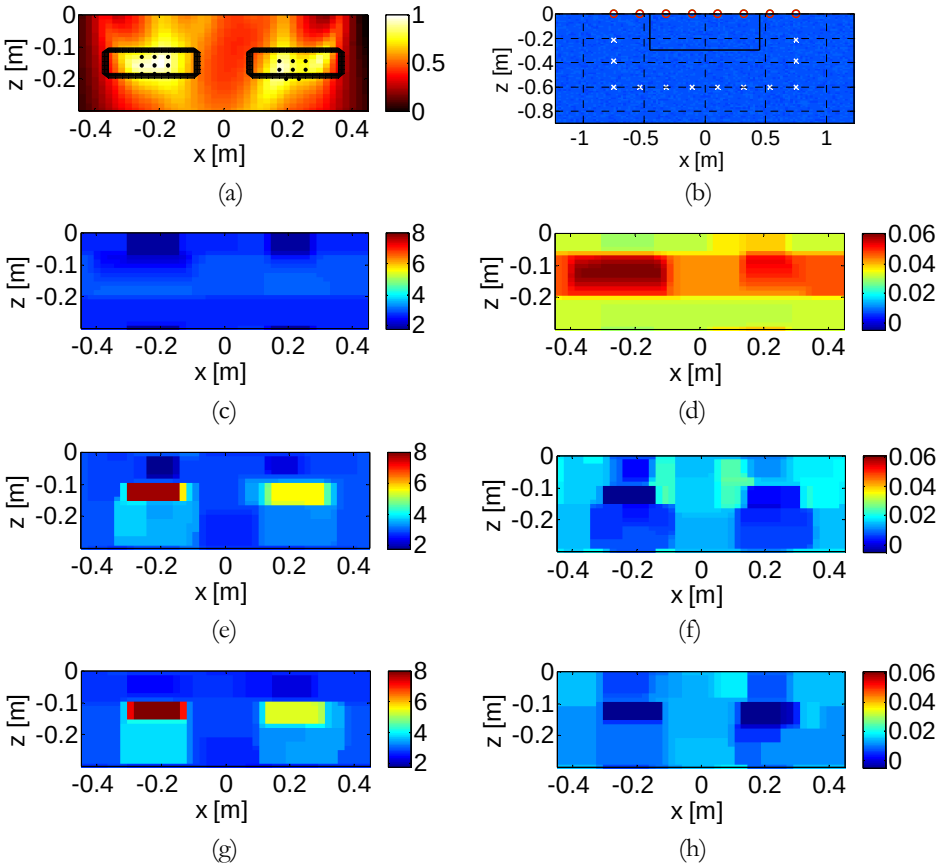

Figure 5.4 Numerical assessment of VE-CS approach for subsurface MWI. Example 2. (a) Logarithmic map of the LSM indicator with superimposed the pivot points and the contour of the reference profile, (b) virtual measurements setup. Permittivity and conductivity of the retrieved profile for SNR=30dB by means of (c)-(d) BA-CS ($\hat{\delta}$ = 0.3) and (e)-(f) VE-CS ($\hat{\delta}$ = 0.15). (g)-(h) the same as (e)-(f) for SNR=10dB with $\hat{\delta}$= 0.17.

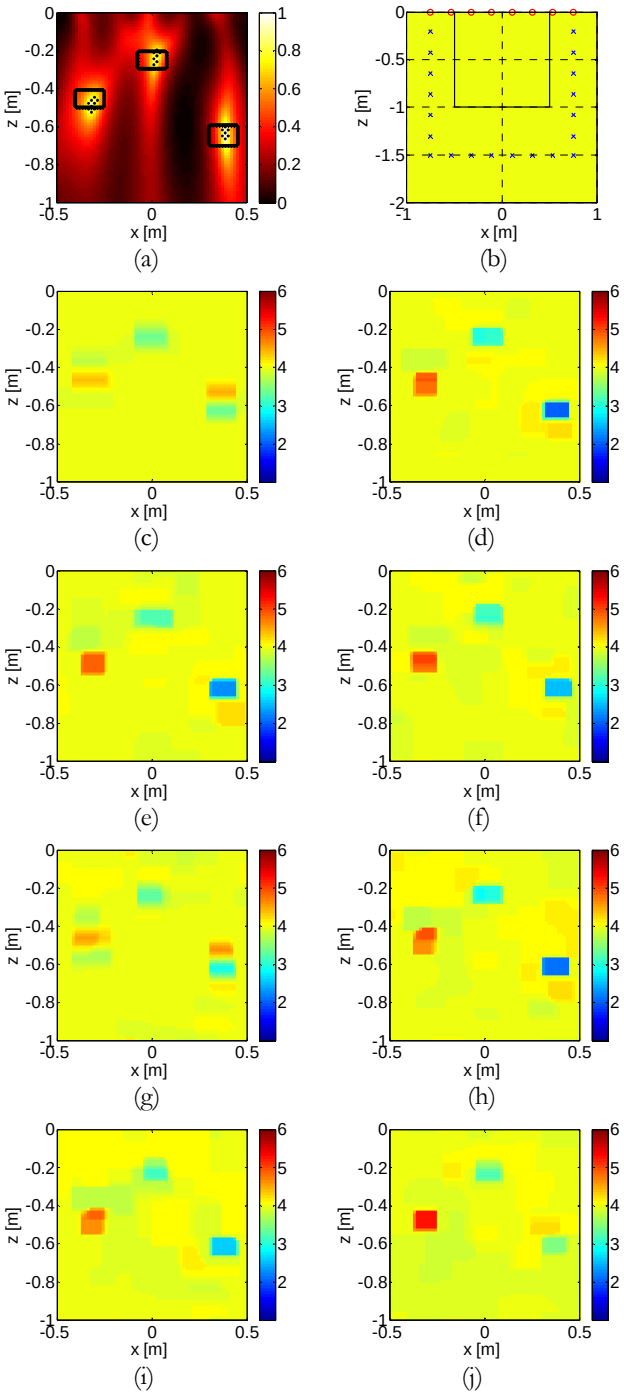

Figure 5.5 Numerical assessment of VE-CS approach for subsurface MWI. Example 2. (a) Logarithmic map of the LSM indicator with superimposed the pivot points and the contour of the reference profile, (b) virtual measurements setup. Permittivity of the retrieved profile by means of the CS with (c) BA ($\hat{\delta}$ = 0.04), (d) VE ($\hat{\delta}$= 0.32), (e)-(f) VE with RF=4 ($\hat{\delta}$= 0.28) and RF=10 ($\hat{\delta}$= 0.15), respectively for SNR=30dB. (g)-(j) the same as (c)-(f) for SNR=10dB with $\hat{\delta}$= 0.26 (BA-CS), $\hat{\delta}$= 0.33 (VE-CS), $\hat{\delta}$= 0.28 (RF=4) and $\hat{\delta}$= 0.24 (RF=10).

Conclusions

Summary of the contributions

In this thesis, new paradigms and tools have been introduced to address the difficulties and the challenges to be faced in the solution of inverse scattering problems. Moreover, it has been demonstrated that the resulting imaging methods are capable to provide accurate and reliable results, from both a morphologic and radiometric point of view.

More in detail, the contributions can be summarized as it follows.

In the first part of the thesis, a new and original strategy for solving inverse scattering problems has been proposed and developed. In particular, by taking into account the linearity of the scattering phenomena with respect to the primary sources (that is, the sources of the incident fields probing the unknown scenario), it has been introduced the idea of using the pre-processing of the collected data to design new experiments, which are referred to as Virtual Experiments, as they do not involve additional 'physical' measurements or experiments. In inverse scattering problems, the knowledge of internal fields (or contrast sources) plays a key role. The exact knowledge of these quantities would allow to consider a linear problem (rather than a non-linear one). On this line of reasoning, the VE have been designed in such a way to condition the total fields and the currents induced inside the targets, and this information has been exploited in the inversion procedure. Note the main difference with the existing solution strategies relies on the fact that this new kind of information does not descend, as usual, from some assumptions on the contrast function, but rather on some smart pre-processing. This represents a new way of thinking about inverse scattering solution which has led to effective and reliable methods, and could still lead to new ones.

In this thesis, three new inversions strategies, DARE, RCSI and DIVE methods, have been introduced and discussed based on proper designed VE, which have been built by means of the generalized solution of the FFE (the equation underlying the well-known LSM). Obviously, the methods turn out to give back reliable and effective results as long as the LSM is able to condition the scattering phenomenon. Nevertheless, it is important to highlight that, in order to go beyond the range of applicability of the LSM, different design tools could be applied to condition the total fields or the contrast sources.

More in detail, the core of the DARE method is an original approximation of the focused contrast sources arising in the designed VE. This introduced approximation, which exploits Bessel function's multiplication theorem and takes also into account part of the non-radiating contrast sources, has allowed to recast the inverse problem through a diagonal system of algebraic equations and, so, to estimate the contrast function by means of the solution of third degree equations. Note this algebraic solution method is non iterative and extremely fast, as the solutions of each equation is independently computed in a closed form. This is an interesting point to address in the view of the future extension to 3D problems.

In RCSI method has been considered an alternative way to enforce the circularly symmetric behavior on the contrast sources by simply adding an appropriate penalty term in usual CSI method. As such, the method is iterative and non-linear, as no approximation has been introduced and the scattering equations have been considered in their full non linearity. The paradigm underlying this method offers a different, possibly complementary, point of view to improve the inversion, as compared to more usual regularization methods that act on the contrast function, and opens the way to new methods to tackle the inverse scattering problem by acting on the auxiliary unknowns.

In DIVE approach, the scattering conditioning has been enforced within an iterative procedure, wherein the Green's functions, VE and corresponding linear approximations have been updated at each step, in order to provide an effective approach to inverse scattering. More in detail, the

method involves at each iteration the field approximation introduced in [*Crocco et al*, 2012a], which in this thesis has been recalled and reinterpreted in the light of the recent developments. This approach has been proved to outperform the DBIM, as it takes implicitly into account at each iteration the nature of the obstacles through the VE redesign step.

Second, in the thesis the CS theory has been exploited in order to obtain nearly optimal reconstruction and reduce the numbers of sensors involved in the measurements procedure, leading to a simpler and cheaper measurements set-up. In particular the CS theory, which up to now had been considered in the literature only within the usual Born or Rytov approximations, has been exploited in conjunction with VE. Moreover, for the first time, CS has been applied to inverse scattering problems by taking into account its full non-linearity.

In particular, three novel CS-inspired inversion methods have been introduced and discussed in the thesis. Note that the applicability of CS theory and, so, the proposed methods is strictly depending on the assumption of sparsity, i.e. by the possibility to characterize the unknown contrast function by a suitable representation basis.

The first one has exploited the field approximation, derived from the VE and introduced in [*Crocco et al.*, 2012a], and explored the possibility of enforcing sparsity in different ways, by considering different representation basis types of the unknown. As such, this approach has turned out more versatile as it could be applied also to the case of extended target, which are non-sparse in the classical pixel basis and belong to the range of applicability of the VE based linear approximation [*Di Donato et al.,* 2015a].

The second approach has a wider range of validity as compared to the previous one, as it takes advantage from the above results by considering the VE and field conditioning in an iterative perspective, i.e. in conjunction with DIVE method. The joined conditioning on both the actual and auxiliary unknowns, realized by CS and VE, respectively, has led to beneficial effects on the reachable performances.

The last method is an original revisiting in a non-linear framework of the CS theory, which up to now has been explored only in linear problems,

so, it could give the possibility to open the way to the application of the CS to general non-linear inverse problems. In particular, two innovative different strategies have been described and tested in conjunction with CSI scheme, wherein sparsity has been enforced by means of strict bounds on the space search while looking for a minimization of the involved cost functional, or by inserting an additional penalty term in the same functional.

Note, unlike the first ones, these last approaches do not involve any approximations. On the other hand, as they consider the problem in its full non linearity, they could suffer from a large computational burden, especially the penalized scheme. Furthermore, if the problem is too challenging and the unknown contrast is not represented in a suitable basis, they could be trapped in false solutions.

Finally, in the last part of the thesis, as a step for truly exploiting the potential of microwave imaging in real world applications, the outcomes reached in the first part, have been applied to two relevant applicative examples, i.e. breast cancer MWI enhanced by MNP, and subsurface imaging.

More in detail, for the breast cancer MWI enhanced by MNPs *ad hoc* CS algorithm has been developed for the reconstruction of the unknown magnetic contrast induced into the tumor, wherein the knowledge of the maximum concentration of MNPs that can be targeted in human tissues has also been exploited to counteract 'over-regularization' induced by CS. From the numerical analysis, performed in realistic conditions in 3D geometry, it is pointed out that the adoption of this new tool allows to improve resolution and accuracy of the reconstructions, as well as to reduce the complexity of the required measurements set-up.

For the subsurface MWI, both the results reached by means of VE and the CS have been conveniently adapted to the problem at hand. In particular, an effective strategy has been developed in order to obtain quantitative reconstructions of non-weak and extended targets and overcome the relevant information lack arising when data are gathered under aspect limited configuration [*Di Donato and Crocco,* 2015]. The numerical examples dealing with simulated data have shown that the proposed strategy significantly outperforms the results achievable with state of the art approaches.

Future developments

Additional possible developments besides the ones analyzed at the end of each Chapter, are worth being mentioned.

First, some interesting hybridizations are possible by suitably mixing the different introduced approaches. For instance, one could exploit the VE framework and, in particular the RCSI method, in conjunction with the CS-inspired non-linear inversion method introduced in Section 3.3, acting simultaneously both on the actual and auxiliary unknowns. Alternatively, one could use as convenient starting point for this latter the outcomes of the DARE method, in order to better fall into the right attraction basin.

Second, it is worth pointing out that all the introduced approaches have been discussed with reference to the canonical scalar electromagnetic TM case. Therefore, in order to progress towards real applications, all the devised approaches have to be extended to vectorial and tridimensional case.

Third, many possible applications of microwave imaging (both qualitative and quantitative), besides the ones considered in the second part, could take benefit from the methodologies presented in this thesis.

For instance, recently an emerging interest has been gained by the Electric Properties Tomography (EPT) [*Balidemaj et al.*, 2015, *Balidemaj et al.*, 2013, *Katscher et al.*, 2009]. EPT is an imaging modality to reconstruct the electric conductivity and permittivity inside the human body based on B_1^+ field maps acquired by a magnetic resonance imaging (MRI) system. The main difference with respect to the standard inverse scattering problem considered in this thesis lies in the fact that an MRI system offers the unique situation in which the magnetic fields within the object of interest can be measured. Hence, every measured voxel can be considered as a virtual receiving antenna, and consequently the ill-posedness of the inverse problem can be reduced. Hence, the method has the potential to achieve high-accuracy permittivity and conductivity tissue maps of interior parts of the human body [*Balidemaj et al.*, 2015, *Balidemaj et al.*, 2013]. In particular, in [*Balidemaj et al.*, 2015] a MR-CSI-EPT method (contrast source inversion-electric properties tomography) is introduced wherein the electric tissue properties are retrieved in an iterative

fashion based on a CSI approach. In this respect, the techniques presented in this thesis could be a valid alternative to the MR-CSI scheme and their applicability can be investigated in the near future.

Finally, due to the analogy between electromagnetic and acoustic scattering phenomena, the developed paradigms and tools can be applied in a relatively easy fashion also to this different area of the engineering and physics, as well as to other wavefields.

Appendices

Appendix A

The series in (2.4), which allows to express the zero order Bessel function as a superposition of Bessel functions, is a power series respect to the variable χ_p. By means of the Theorem of Cauchy-Hadamard [*Di Bari and Vetro*, 1998] it is possible to investigate on its convergence and compute the radius R which defines the convergence region by means of the following close formula:

$$R = \lim_{n\to\infty} \frac{|a_n|}{|a_{n+1}|} \tag{A.1}$$

wherein a_n is the generic coefficient of the power series, having the following mathematical expression:

$$a_n = \frac{(-1)^n}{n!}\left(\frac{k_b\rho}{2}\right)^n J_n(k_b\rho) \tag{A.2}$$

By following eq. (A.1) and considering the properties of Bessel functions for $n \to \infty$, the series (2.4) is proved to be convergent $\forall \chi_p \in \mathbb{C}$ as its radius R is equal to ∞ . In fact:

$$R = \lim_{n\to\infty} \frac{|J_n(k_b\rho)|}{|J_n(k_b\rho)|}\frac{2(n+1)}{|k_b\rho|} = \lim_{n\to\infty} \frac{2(n+1)}{e|k_b\rho|}\frac{2(n+1)}{|k_b\rho|} = \infty \tag{A.3}$$

Another important parameter is represented by the remainder of the series (2.4) when it is truncated to the third term and only the terms for $k = 0,1,2$ are considered, as in eq.(2.5). If a lossless background and lossless targets are considered, the series (2.4) has real coefficients and an alternating sign. Hence:

$$\left|\sum_{n=0}^{\infty} a_n {\chi_p}^n - \sum_{n=0}^{2} a_n {\chi_p}^n\right| < \left|a_3 {\chi_p}^3\right| = \frac{{\chi_p}^3}{3!}\left(\frac{k_b\rho}{2}\right)^3 J_3(k_b\rho) \tag{A.4}$$

wherein the right-hand side represents a possible estimation of the upper bound for the fourth term of the series. Hence, truncation of eq. (2.4) implies a negligible error for a sufficiently small radius ρ. Moreover, eq. (A.4) allows a smart choice of R_p.

Appendix B

An interesting question arises of how the three principal terms of the eq. (2.4) contribute to the radiated field. Starting to eq. (2.4), which relates the contrast source $\mathcal{W}$ to the local contrast function χ_p, it is possible to extract an analytical expression for the radiative part of the currents inside the circular neighborhood $\mathcal{I}_{R_p}(\boldsymbol{r}_p)$. In particular, as discussed in [*Marengo et al.*, 2000, *Marengo and Ziolkowski*, 2000, *Devaney and Wolf,* 1973], radiating (minimum energy) components of a source have to fulfill the Helmholtz equation in the background medium, so the radiating component $\mathcal{W}_{RAD}$ can be identified as the projection of the $\mathcal{W}$ respect to the $J_0(k_b\rho)$, where $\rho = |\boldsymbol{r} - \boldsymbol{r_p}|$. More in detail:

$$\mathcal{W}_{RAD}(\boldsymbol{r}, \boldsymbol{r}_p) \approx \langle \mathcal{W}(\boldsymbol{r}, \boldsymbol{r}_p), J_0(k_b\rho) \rangle J_0(k_b\rho) =$$

$$w_0{}^p \left\{\sum_{n=0}^{\infty} \frac{(-1)^n}{n!} \int_{\mathcal{I}_{R_p}} \left(\frac{\chi_p k_b}{2}\right)^n J_n(k_b\rho)\, J_0(k_b\rho)\, \rho^{n+1}\, d\rho \right\} J_0(k_b\rho) \tag{B.1}$$

Note, if the radius R_p of the circular neighborhood tend to infinity, the integrals in eq. (B.1) would be equal to zero but for $n = 0$ and, so, the only radiating component would be represented by $w_0{}^p J_0(k_b\rho)$. As R_p assumes a finite value, the integral are different from zero and are computable in closed form. In fact, being the local value of the contrast χ_p constant inside $\mathcal{I}_{R_p}$ and by changing the integral variable as $x = k_b\rho$, the eq. (B.1) can be rewritten as:

$$\mathcal{W}_{RAD}(\boldsymbol{r},\, \boldsymbol{r}_p)$$
$$\approx {w_0}^p \left\{ \sum_{n=0}^{\infty} \frac{(-1)^n}{n!} \left(\frac{\chi_p k_b}{2}\right)^n \frac{1}{{k_b}^{n+2}} \int_0^{k_b R_p} J_n(x)\, J_0(x)\, x^{n+1}\, dx \right\} J_0(k_b \rho)$$

(B.2)

By exploiting the well-known properties of the Bessel function [*Abramowitz and Stegun*, 1964], that is:

$$\int \mathcal{C}_\mu(x)\, \mathcal{D}_\nu(x) x^{\mu+\nu+1} dx =$$
$$\frac{x^{\mu+\nu+2}}{2(\mu+\nu+1)} \left(\mathcal{C}_\mu(x) \mathcal{D}_\nu(x) + \mathcal{C}_{\mu+1}(x) \mathcal{D}_{\nu+1}(x) \right)$$
$$\mathcal{C}_{\mu-1}(x) + \mathcal{C}_{\mu+1}(x) = \frac{2\mu}{x} \mathcal{C}_\mu(x)$$

(B.3)

where $\mathcal{C}_\mu(x)$ and $\mathcal{D}_\nu(x)$ are two generic cylindrical function or order μ and ν, then:

$$\mathcal{W}_{RAD}(\boldsymbol{r},\, \boldsymbol{r}_p) \approx {w_0}^p \left\{ \sum_{n=0}^{\infty} \frac{(-1)^n}{n!} \left(\frac{\chi_p k_b}{2}\right)^n \frac{{R_p}^{n+2}}{2(n+1)} \left[J_n(k_b R_p) J_0(k_b R_p) \right.\right.$$
$$\left.\left. + J_{n+1}(k_b R_p) J_1(k_b R_p) \right] \right\} J_0(k_b \rho)$$

(B.4)

As in DARE method only the first three terms of the series (2.4) are considered, the expression of the radiating part can be truncated to the first three terms, as it follows.

$$\mathcal{W}_{RAD}(\boldsymbol{r},\, \boldsymbol{r}_p) \approx$$
$${w_0}^p \left\{ \frac{{R_p}^2}{4} \left[{J_0}^2(k_b R_p) + {J_1}^2(k_b R_p) \right] - \frac{\chi_p}{4} {R_p}^2 {J_1}^2(k_b R_p) + \right.$$
$$\left. \frac{{\chi_p}^2}{48} {k_b}^2 {R_p}^4 \left[J_0(k_b R_p) J_2(k_b R_p) + J_1(k_b R_p) J_3(k_b R_p) \right] \right\} J_0(k\rho)$$

(B.5)

Note that in eq. (B.5) all the three terms contribute to the radiating part of the current. An analysis on the amplitude of the field radiated by each term has pointed out that the more significant part is constituted by the first term.

By considering the radiating part of the different contributions, one may separate the radiating and non-radiating components of the contrast sources. In fact, the non-radiating component is defined as by the difference between $\mathcal{W}(\boldsymbol{r}, \boldsymbol{r}_p)$ and $\mathcal{W}_{RAD}(\boldsymbol{r}, \boldsymbol{r}_p)$, that is:

$$\mathcal{W}_{NRAD}(\boldsymbol{r}, \boldsymbol{r}_p) \approx {w_0}^p \sum_{n=0}^{\infty} \frac{1}{n!}\left(\frac{-\chi_p k_b}{2}\right)^n \{\rho^n J_n(k_b\rho) - \mathcal{w}_{RAD}\, J_0(k_b\rho)\} \tag{B.6}$$

where:

$$\mathcal{w}_{RAD} = \frac{{R_p}^{n+2}}{2(n+1)}\left[J_n(k_b R_p)J_0(k_b R_p) + J_{n+1}(k_b R_p)J_1(k_b R_p)\right]$$

Appendix C

Let us substitute eq.(2.5) in eq.(2.8). By neglecting the integral over $\bar{\mathcal{I}}_{\mathrm{R_p}}$ one obtains:

$$\mathcal{E}_s(\boldsymbol{r}, \boldsymbol{r_p}) \approx {w_0}^p\{b^p + c^p\chi_p + d^p{\chi_p}^2\} \tag{C.1}$$

where:

$$b^p = \mathcal{A}_e[J_0(k_b\rho)]$$

$$c^p = \mathcal{A}_e\left[-\frac{1}{2}k_b\rho\, J_1(k_b\rho)\right]$$

$$d^p = \mathcal{A}_e\left[\frac{1}{8}{k_b}^2\rho^2\, J_2(k_b\rho)\right]$$

Note that in (C.1) $\boldsymbol{r}$ belongs to the measurement domain and the operator $\mathcal{A}_{\mathrm{e}}$ is defined over $\mathcal{I}_{R_p}(\boldsymbol{r_p})$. Moreover, since the contrast is assumed to be constant in $\mathcal{I}_{R_p}(\boldsymbol{r_p})$, it has been singled out from the integral operators.

For a given pivot point, the coefficient ${w_0}^p$ in (C.1) is constant, as it does not depend on the measurement position. As such, for each pivot point,

it is possible to obtain an explicit expression for it, by averaging eq. (C.1) with respect to the M different measurements. In particular, a very compact expression for the reciprocal of ${w_0}^p$ is obtained as:

$$\frac{1}{{w_0}^p} \approx \left\{\bar{b}^p + \bar{c}^p \chi_p + \bar{d}^p {\chi_p}^2\right\} \tag{C.2}$$

where:

$$\bar{b}^p = \frac{1}{M}\sum_{i=1}^{M} \frac{b^p(i)}{\mathcal{E}_s(\boldsymbol{r_{mi}}, \boldsymbol{r_p})}$$

$$\bar{c}^p = \frac{1}{M}\sum_{i=1}^{M} \frac{c^p(i)}{\mathcal{E}_s(\boldsymbol{r_{mi}}, \boldsymbol{r_p})}$$

$$\bar{d}^p = \frac{1}{M}\sum_{i=1}^{M} \frac{d^p(i)}{\mathcal{E}_s(\boldsymbol{r_{mi}}, \boldsymbol{r_p})}$$

where $r_{mi} \in \Gamma$ identifies the position of the different measurements.

Let us now substitute equation (2.5) in equation (2.7). Similarly, the algebraic equation obtained is the following one:

$$\eta^p {\chi_p}^3 + \beta^p {\chi_p}^2 + \gamma^p \chi_p + \delta^p = 0 \tag{C.3}$$

where:

$$\eta^p = \frac{1}{8} {a_0}^p \mathcal{A}_i \left[{k_b}^2 \left|\boldsymbol{r} - \boldsymbol{r_p}\right|^2 J_2(k_b \left|\boldsymbol{r} - \boldsymbol{r_p}\right|)\right]$$

$$\beta^p = -\frac{1}{2} {a_0}^p \mathcal{A}_i \left[k_b \left|\boldsymbol{r} - \boldsymbol{r_p}\right| J_1(k_b \left|\boldsymbol{r} - \boldsymbol{r_p}\right|)\right]$$

$$\gamma^p = \mathcal{E}_i(\boldsymbol{r}, \boldsymbol{r_p}) + {a_0}^p \mathcal{A}_i \left[J_0(k_b \left|\boldsymbol{r} - \boldsymbol{r_p}\right|)\right]$$

$$\delta^p = -{\omega_0}^p$$

Note in (C.3) $\boldsymbol{r}$ now belongs to the investigation domain.

If now one uses the equation (C.2) in equation (C.3), a final third degree polynomial expression can be obtained, where the only unknown is the contrast. In fact:

$$\bar{A}^p {\chi_p}^3 + \bar{B}^p {\chi_p}^2 + \bar{C}^p \chi_p + \bar{D}^p = 0 \tag{C.4}$$

where:

$$\bar{A}^p = \mathcal{E}_i(\boldsymbol{r}, \boldsymbol{r_p})\, \bar{d}^{(p)} + \frac{1}{8}\mathcal{A}_i\left[{k_b}^2 \rho^2 J_2(k_b\rho)\right]$$

$$\bar{B}^p = \mathcal{E}_i(\boldsymbol{r}, \boldsymbol{r_p})\, \bar{c}^p - \frac{1}{2}\mathcal{A}_i[k_b\rho\, J_1(k_b\rho)]$$

$$\bar{C}^p = \mathcal{E}_i(\boldsymbol{r}, \boldsymbol{r_p})\, \bar{b}^p + \mathcal{A}_i[\, J_0(k_b\rho)]$$

$$\bar{D}^p = -1$$

Equation (C.4) is a third degree polynomial equation in the only unknown χ_p. Therefore, its solution allows to obtain the local value of the contrast in each pivot point.

Appendix D

The Contrast Source Inversion scheme [*van den Berg et al.*,1997, *Isernia et al.*, 2004, *Isernia et al.*, 1997] does not involve any approximation and tackles the inverse scattering problem in its full non linearity by contemporary looking for both the unknown contrast χ and the auxiliary unknown W. In particular, the problem's solution is iteratively found by minimizing the following cost functional, which takes into account the data-unknowns relationship and the physical model, [*Isernia et al.*, 2004, *Isernia et al.*, 1997]:

$$\Phi\left(\chi, W^{(1)}, \dots, W^{(N)}\right) = \Phi_\Omega\left(\chi, W^{(1)}, \dots, W^{(N)}\right) + \Phi_\Gamma\left(W^{(1)}, \dots, W^{(N)}\right)$$

with

$$\Phi_\Omega\left(\chi, W^{(1)}, \dots, W^{(N)}\right) = \sum_{v=1}^{N} {\kappa^{(v)}}_\Omega \left\| W^{(v)} - \chi {E_i}^{(v)} - \chi\mathcal{A}_i\left[W^{(v)}\right]\right\|_\Omega^2$$

$$\Phi_{\Gamma}\left(W^{(1)},\dots,W^{(N)}\right)=\sum_{v=1}^{N}{\kappa^{(v)}}_{\Gamma}\left\|{E_s}^{(v)}-\mathcal{A}_e\left[W^{(v)}\right]\right\|_{\Gamma}^{2} \tag{D.1}$$

where $\|\cdot\|$ is the l_2 norm and ${\kappa^{(v)}}_{\Omega}$ and ${\kappa^{(v)}}_{\Gamma}$ are normalization coefficients.

Note the normalization term for the state equation ${\kappa^{(v)}}_{\Omega}$ is usually set equal to the norm of the product of the contrast function times the incident field [*van den Berg and Kleinman*, 1997]. Although this seems a natural choice, it has the drawback of changing, in an unpredictable way, the metric at each iteration of the minimization process. For this reason, different from the usual CSI scheme in [*van den Berg and Kleinman*, 1997], in the following just the norm of the incident field is used as a normalization factor. More in detail, ${\kappa^{(v)}}_{\Omega}=\left\|{E_i}^{(v)}\right\|_{\Omega}^{2}$ and ${\kappa^{(v)}}_{\Gamma}=\left\|{E_s}^{(v)}\right\|_{\Gamma}^{2}$.

As discussed in I.4, the functional (D.1) is a non-quadratic functional of the unknowns and usually depends on thousands of variables. For these reasons, globally effective minimization schemes do not exist for functions of so many variables and the gradient-based minimization scheme could be trapped in local minima. As a suitable compromise between convergence properties and computational as well as memory requirements, the problem of how to find the global minimum of (D.1) is pursued by following a quasi-Newton minimization procedure, whose scheme is:

$$\begin{aligned}\chi_{(k+1)}&=\chi_k+\mu_k\mathrm{H}_k\nabla\chi_k\\ W_{(k+1)}&=W_k+\mu_k\mathrm{H}_k\nabla\mathrm{W}_k\end{aligned} \tag{D.2}$$

where k and $(k+1)$ denote the k^{th} and the $(k+1)^{\text{th}}$ iteration, respectively, $\nabla\chi$ and ∇W are the gradient of the functional Φ with respect to χ and W respectively, μ_k is a scalar factor that has to be evaluated at each iteration in order to guarantee the maximum decrease of the functional along the direction given by $\mathrm{H}\nabla\mathrm{W}$. Finally, H is defined accordingly to the Polak–Ribiere scheme [*Isernia et al.*, 1997].

The minimization of the cost function (D.1) does not involve an alternating optimization of the contrast function and the contrast source, but instead a joint updating of the two quantities by using the scheme (D.2) [*Isernia et al.*, 1997]. This is a fundamental difference respect to [*van den Berg et al.*,1997]. Accordingly, the line minimization step μ_k is performed in a very efficient and precise manner as:

$$\mu_k = \operatorname{argmin} \Phi\left(\chi_k + \mu_k \Delta\chi_k, W_k^{(1)} + \mu_k \Delta W_k^{(1)}, \ldots, W_k^{(N)} + \mu_k \Delta W_k^{(N)}\right) \tag{D.3}$$

where $\Delta\chi_k$ and ΔW_k represent the descent research directions considered at the k^{th} iteration. Accordingly, the computation of μ_k is based on the minimization of a non quadratic functional, different from [*van den Berg and Kleinman*, 1997] which alternatively updates currents and contrast function and, so, considers the minimization of a parabolic functional, which admits only a minimum. This represents an important advantage of using approach (D.3), as it could open the way to possible 'tunneling', i.e. path from an attraction basin to a more convenient one.

However, Equation (D.3) due to the nature of the involved operators implies the solution of a third degree algebraic equation which is available in a closed form [*Isernia et al.*, 1997].

For more detail about the general structure of the optimization procedure and computation of the gradient of the functional Φ with respect to χ and W, the reader is referred to [*Isernia et al.*, 1997].

Appendix E

Many tutorials have been written on the essentials of CS, and some of them have been written from scientists originating [*Donoho*, 2006, *Candès et al.*, 2006] or anyway contributing to the theory of CS [*Baraniuk*, 2007]. Nevertheless, a contribution can still be given to a possibly simple understanding of the basic tools and results, as well as to the introduction of

further point of views to the problem. To this end, by taking inspiration from (but modifying substantially) the geometrical point of view suggested in [*Baraniuk*, 2007], in this appendix a framework for simple understanding is developed on the basis on the properties of the sets determined from the data equation and the sparsity assumption.

Such an approach allows to understand in a relatively easy fashion the rationale of the more widespread approaches to the recovery of sparse signals from compressed data. In fact, they can be interpreted as the search for an intersection amongst the sets determined from the data equation and from the sparsity assumption, respectively.

E.1 Recovery of sparse signals: an intersection amongst (non) convex sets approach

By the sake of simplicity, the problem is approached in a basis wherein the unknown signal is sparse, real signals and measurements are assumed, and the measurements are also supposed to be error-free. Let us separately discuss the geometrical information separately carried by the data equation $\boldsymbol{y} = \boldsymbol{A}\boldsymbol{x}$ and by the sparsity assumption. In general case $\boldsymbol{x}$ belongs to $\mathbb{R}^{N_x}$, and $\boldsymbol{y}$ belongs instead to $\mathbb{R}^{N_y}$.

About the geometrical meaning of the data equation, in those cases where $N_y = N_x$ and $\boldsymbol{A}$ has a full rank, the data equation identifies a single point in the space where the signal is sparse. On the other hand, in those cases wherein $N_y < N_x$ (or, more simply, when the rank N_y' of $\mathbf{A}$ is less than N_y) it can be instead interpreted as a set of linear constraints in the same space. More precisely, these constraints will define a line if $N_y' = N_x - 1$, a plane if $N_y' = N_x - 2$, and an hyperplane if $N_y' = 1$. Whatever is the case, a convex set (or more precisely, a linear manifold) is defined in the space of the unknowns.

In fig. E.1 the kind of possible solutions of the data equation is reported in the cases where $N_x = 3$ and N_y' is equal to 3, 2 and 1 respectively ((a), (b) and (c) respectively).

Concerning the geometrical meaning of the sparsity assumption, assuming that the signal is sparse simply means that it cannot be a whatever point of the space spanned by $x_1, \ldots, x_{N_x}$, but it will be located along the axes of such a space (when $S = 1$), or on the different coordinate planes of such a space (when $S = 2$), or on the different subspaces of order three (when $S = 3$) and so on and so forth. Figure E.2 reports the allowed set of solutions for the cases where $N_x = 3$ and S is equal to 1 and 2 respectively.

Understanding of the kind of problems one will deal with can be acquired by intersecting the sets determined by the data equation and the sparsity assumption respectively. In order to take profit from geometrical intuition, one can develop the case $N_x = 3$. Similar but less intuitive situations will occur in other cases. Leaving aside the trivial case $N_y' = 3$, where one of the two sets is a single point, one is left with four cases, namely:

i. one independent measurement ($N_y' = 1$) and $S = 2$;
ii. one independent measurement ($N_y' = 1$) and $S = 1$;
iii. two independent measurements ($N_y' = 2$) and $S = 2$;
iv. two independent measurements ($N_y' = 2$) and $S = 1$.

In the first case, the solution is ambiguous amongst infinitely many possible solutions. In fact, (see fig. E.3 (a)) the solution may be any point along the lines determined from the intersection amongst the data plane (i.e. the green plane) and the three coordinate planes. The result is indeed obvious, as one cannot pretend to recover a signal characterized by at least two real numbers from a single real number. As a matter of fact, one expects in fact things will work when N_y' is at least as large as S, or preferably higher.

In the second case, one has to intersect the plane determined from the data equation with the set constituted by the three coordinate axes (see fig. E.3(b)). As a consequence, three different solutions will be eventually found for a generic orientation of the plane, so that $\boldsymbol{x}$ is not univocally determined. However, the ambiguity is limited amongst just three possible solutions.

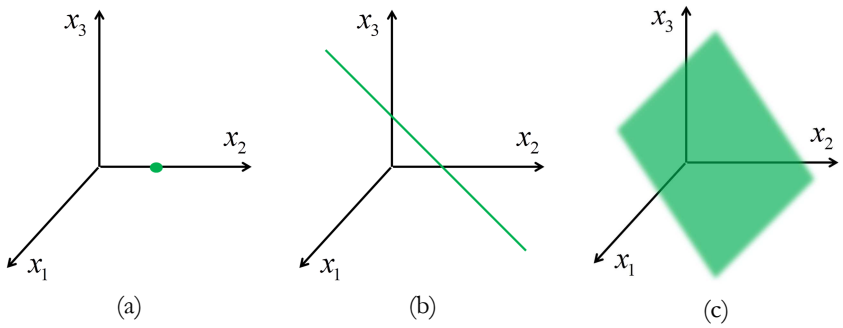

Figure E.1 CS 'for dummies'. Sets defined by data equation for $N_x = 3$ and $N'_y = 3$ (a), 2 (b) and 1(c).

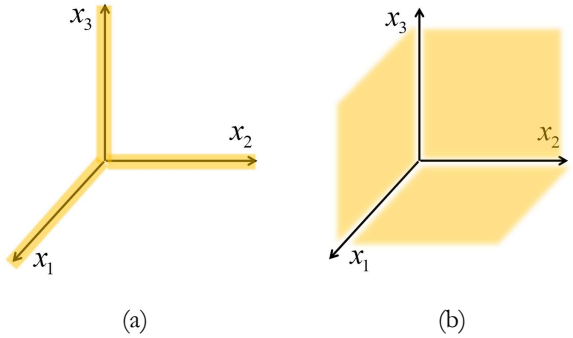

Figure E.2 CS 'for dummies'. Sets defined by sparsity assumption for $N_x = 3$ and $S = 2$(a) and 1(b).

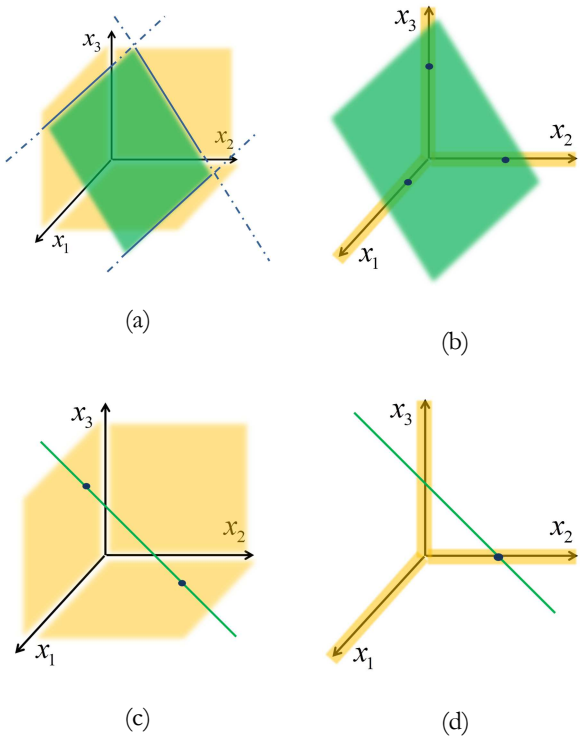

Figure E.3 CS 'for dummies'. Intersections the sets determined by the data equation and the sparsity assumption.

In the third case, one has to intersect the data line with the set constituted by the three planes $x_3 = 0$, $x_2 = 0$, and $x_1 = 0$. As a consequence (see fig. E.3(c)), two different solutions will be generally found, so that $\boldsymbol{x}$ is not univocally defined.

Cases (ii) and (iii) above indicate that a number of (independent) measurements as large as the degree of sparsity S is not sufficient to recover the unknown signal. Such a circumstance is indeed always true, as the S real measurements will allow to determine S real numbers, but then some additional information (besides data and sparsity) is needed to determine which S-ple of numbers (amongst the $\binom{N_x}{S}$ possibilities) is the actual ground truth. Approximate arguments suggest that besides the S initial measurements, additional information equivalent at least to S integers (identifying locations) should be somehow collected or provided. As a consequence, one expects that a number of measurements in the order of $2S$ or larger is actually needed.

Examination of the fourth case above confirms indeed the above expectations. In such a case, one has to intersect the line determined by the data equation with the (non convex) set determined by the three coordinate axis (see fig. E.3(d)). Then, unless one is so unlucky that the data line belongs to one of the coordinate planes, the solution is univocally determined.

Notably the orientation of the data line depends of the kind of measurements which one is performing, which emphasizes once more that besides N_y or $N_y{}'$ the kind of measurements which is being collected also plays a role.

E.2 Looking for sparse signals: ℓ_p balls and a possible approach

As sparse signals are of interest, it makes sense to introduce and exploit quantities able to emphasize the occurrence of sparse signals. To this end, it

makes sense to recall the definition of the ℓ_p norm of the vector $\boldsymbol{x}$, which is given by:

$$\|\boldsymbol{x}\|_{\ell_p} = \left[\sum_{i=1}^{N_x} |x_i|^p\right]^{1/p} \tag{E.1}$$

which makes sense provided $p > 0$. Then, one can define an 'ℓ_p ball' of radius R as:

$$\|\boldsymbol{x}\|_{\ell_p} \leq R \tag{E.2}$$

Notably, as long as the usual Euclidean norm ($p = 2$) is adopted, the boundary of the set defined by (E.2) is the usual sphere in case $N_x = 3$, and a so-called hypersphere in case $N_x > 3$. When different values of p are used, different domains are defined, which are depicted in case $N_x = 3$ in fig. E.4. These domains are usually referred to as ℓ_p balls of radius R.

It is interesting to note that the set defined from (E.2) is a convex one as long as $p \geq 1$, while it becomes non convex as soon as $p < 1$. In addition to that when $p = 0.5$, the set defined from (E.2) is constituted essentially by (a part of) the coordinate axes, and (a part of) the coordinate planes. Saying it in other words, balls of the kind (E.2) are constituted by just sparse signals when $p \to 0$.[7] A better understanding can be gained by re-arranging eq. (E.2) into:

$$\sum_{i=1}^{N} |x_i|^p \leq R^p \tag{E.3}$$

which for $p \to 0$, identifies 1-sparse signal for any finite value of R. If, however, R is allowed to tend to infinity, condition (E.3) can also be reformulated as:

$$\sum_{i=1}^{N_x} |x_i|^p \leq \hat{R}$$

[7] Although our figures concern the case $N_x = 3$, such a statements holds indeed true for any value of N_x.

(E.4)

Notably, depending on the value of $\hat{R}$, eq. (E.4) will include (for $p \to 0$) signals which are at most S-sparse when $\hat{R} = S$. [8]

Therefore, by taking inspiration from [*Gubin et al.*, 1967], a possible way to formulate the recovery problem is that of looking for the intersection amongst the convex set (linear manifold) defined from the data equation and the set defined by (E.4).

If the unknown signal is sparse and $\hat{R}$ is sufficiently large, an intersection amongst the two sets will certainly exist. However, two relevant questions are left still open, i.e.,

- Is such an intersection unique or not?
- How is it possible to find such an intersection?

Both these issues are relevant, as a reliable (univocal) solution is looked for, but the computational complexity of the retrieval procedure is also of interest.

It can be understood by very simple geometrical arguments that, as expected, the uniqueness of the intersection depends on three basic circumstances, which are

i. the number of independent measurements;
ii. the kind of measurements which is performed;
iii. the expected sparsity properties of the solution.

In fact, the larger the number of measurements, the smaller the convex set associated to the data equation, and hence the smaller the number of possible intersections. Analogously, the smaller S, the smaller the set associated to the sparse signal, and the smaller the number of intersections with the set determined from the data equation.

[8] Note it is assumed $|0|^p = 0$ when p→ 0

E.3 Finding sparse solutions: a formulation in terms of Convex Programming

By further elaborating the point of view above, an effective approach to find the intersection, and hence sparse solutions for the initial problem $\boldsymbol{Ax} = \boldsymbol{y}$, is that of progressively enlarging the set determined from eq. (E.4) (i.e., enlarging $\hat{R}$) until an intersection exists with the data set. In a mathematical fashion, the problem is equivalent to:

$$\min \sum_{i=1}^{N_x} |x_i|^p \quad subject\ to \quad \boldsymbol{\Theta x} = \boldsymbol{y} \tag{E.5}$$

In order to deal just with sparse signals, p should be as small as possible. Notably, besides looking for an intersection amongst ℓ_p balls and data equation, formulation (E.5) also looks for the sparsest possible solution. On the other side, the set defined from eq. (E.4) is not convex as long as $p <$1, so that the optimization problem (E.5) is a hard one to deal with. In fact, the problem of finding the intersection amongst a number of non convex sets is known to be subject to 'trapping' problems [*Gubin et al.*, 1967]. Also, it can be argued that the smaller p, the harder the problem. Then, a suitable compromise, which implies some small price to be paid, is to consider the case where $p = 1$, i.e.,:

$$\min \ \|\boldsymbol{x}\|_{\ell_1} \ subject\ to \ \boldsymbol{\Theta x} = \boldsymbol{y} \tag{E.6}$$

In fact, such an optimization problem, which is commonly referred to a Basis Pursuit problem, is relatively easy to be solved, and it still allows to enforce sparsity assumptions. In fact, problem (E.6) is in the class of Convex Programming problems. Moreover, by paying some extra price in terms of the kind of measurements to be performed with respect to the case $p \to 0$, uniqueness (and correctness) of intersections can still be granted (see fig. E.5 for an intuitive explanation).

On the other side, the number of measurements which are needed keeps in the same order, so that the approach is considered to be 'nearly optimal' for sparse signal recovery (see [*Candès et al.*, 2006] and [*Donoho,* 2006]).

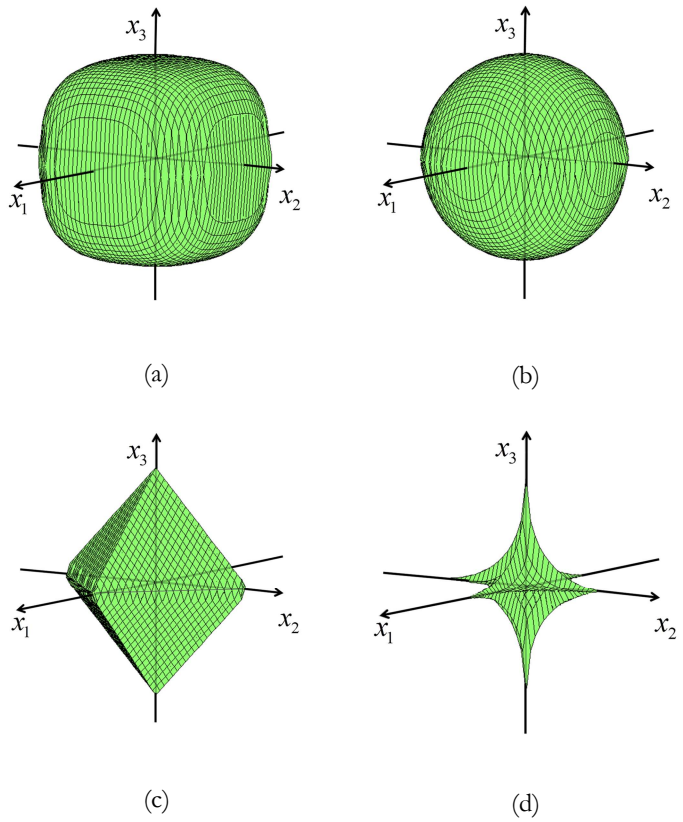

Figure E.4: CS 'for dummies'. ℓ_p-balls for the cases p=3 (a), p=2 (b), p=1 (c) and p=0.5 (d)

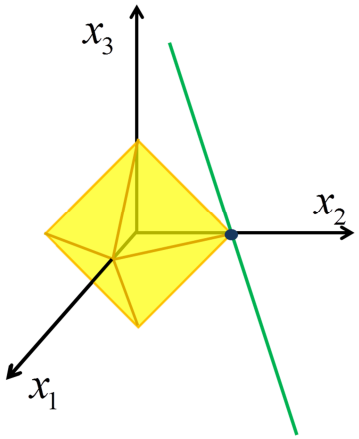

Figure E.5: CS 'for dummies'. Intersection between ℓ_1 - ball and data set. As long as the data set is not parallel to any face or edge of the ℓ_1 - ball solution to (C.6) is unique, and corresponds to the solution of the original intersection problem.

References

[*Abramowitz and Stegun*, 1964] M. Abramowitz, and I. A. Stegun, Handbook of Mathematical Functions with Formulas, Graphs, and Mathematical Tables, *New York*, *Dover Publications*, 1964.

[*Abubakar et al.*, 2005] A. Abubakar, P. M. van den Berg, and T. M. Habashy, Application of the multiplicative regularized contrast source inversion method on TM and TE polarized experimental Fresnel data, *Inverse Probl.*., vol. 21, n. 6, pp. S5-S13, 2005.

[*Ahmad and Amin*, 2013] F. Ahmad, and M. G. Amin, Through-the-wall human motion indication using sparsity-driven change detection, *IEEE Trans. on Geosci. Remote Sens.*, vol. 51, no. 2, pp. 881-890, 2013.

[*Ambrosanio and Pascazio*, 2015] M. Ambrosanio, and V. Pascazio, A compressive-sensing-based approach for the detection and characterization of buried objects, *IEEE Journal of Selected Topics in Applied Earth Observations and Remote Sensing*, vol. 8, no. 7, pp. 3386–3395, 2015.

[*Antonini et al.*, 1992] M. Antonini, M. Barlaud, P. Mathieu, and I. Daubechies, Image coding using wavelet transform, *IEEE Trans. Image Process.*, vol. 1, no. 2, pp. 205–220, Apr. 1992.

[*Azghani et al.*, 2015] M. Azghani, P. Kosmas, F. Marvasti, Microwave Medical Imaging Based on Sparsity and an Iterative Method With Adaptive Thresholding, *IEEE Trans. Medical Imaging*, vol. 34, no. 2, pp. 357-365, 2015.

[*Balidemaj et al.*, 2013] E. Balidemaj et al., CSI-EPT: A novel contrast source approach to MRI based electric properties tomography and patient-specific SAR, *IEEE Int. Conf. Electromagn. Adv. Appl.*, pp. 668–671, 2013.

[*Balidemaj et al.*, 2015] E. Balidemaj et al., CSI-EPT: A Contrast Source Inversion Approach for Improved MRI-Based Electric Properties Tomography, *IEEE Trans. Medical Imaging*, vol. 34, no. 9, pp. 1788-1796, Sept. 2015.

[*Baraniuk*, 2007] R. G. Baraniuk, Compressive sampling, *IEEE Signal Process. Mag.*, vol. 24, no. 4, pp. 118-124, Jul. 2007.

[*Baussard*, 2005] A. Baussard, Inversion of multi-frequency experimental data using an adaptive multiscale approach, *Inverse Probl.*, vol. 21, pp. S15-S31, Dec. 2005.

[*Belkebir and Saillard*, 2001] K. Belkebir and M. Saillard, Special section: Testing inversion algorithms against experimental data, *Inverse Probl.*, vol. 17, pp. 1565–1571, 2001.

[*Belkebir and Saillard*, 2005] K. Belkebir and M. Saillard, Special section: Testing inversion algorithms against real data: Inhomogeneous targets, *Inverse Probl.*, vol. 21, 2005.

[*Bellizzi et al.*, 2011] G. Bellizzi, O. M. Bucci, and I. Catapano, Microwave Cancer Imaging Exploiting Magnetic Nanoparticles as Contrast Agent, *IEEE Trans. On Biomed.Eng.*, vol. 58, no. 9, pp. 2528-2536, Sept. 2011.

[*Bellizzi and Bucci*, 2013] G. Bellizzi, and O.M. Bucci, A novel measurement technique for the broad characterization of diluted water ferrofluids for biomedical applications, *IEEE Trans. on Magnetics*, vol. 49, no 6, pp. 2903-2912, 2013.

[*van den Berg and Kleinman*, 1995] P. M. van den Berg and R. E. Kleinman, A total variation enhanced modified gradient algorithm for profile reconstruction, *Inverse Probl.*, vol. 11, no. 3, pp. L5–L10, 1995.

[*van den Berg and Kleinman*, 1997] P. M. van den Berg, and R. E. Kleinman, A contrast source inversion method, *Inverse Probl.*, vol. 13, no. 6, pp. 1607–1620, 1997.

[*van den Berg et al.*, 2003] P. M. van den Berg, A. Abubakar, and J. T. Fokkema, Multiplicative regularization for contrast profile inversion, *Radio Science*, vol. 38, no. 2, 2003.

[*Bertero*, 1989] M. Bertero, Linear inverse and ill-posed problems, *Adv. Electron. Phys.*, vol. 75, pp. 1-120, 1989.

[*Bertero and Boccacci*, 1998] M. Bertero, and P. Boccacci, Introduction to Inverse Problems in Imaging. Bristol, *UK: Institute of Physics*, 1998.

[*Bevacqua et al.*, 2014a] M. Bevacqua, L. Di Donato, L. Crocco, T. Isernia, Conditioning inverse scattering problems by means of suitably designed synthetic experiments, *Antennas and Propagation (EuCAP), 8th European Conference on*, vol., no., pp. 1336-1339, 6-11 April 2014.

[*Bevacqua et al.*, 2014b] M. Bevacqua, T. Isernia, L. Crocco, L. Di Donato, A $(CS)^2$ approach to inverse scattering, *Antenna Measurements & Applications (CAMA), 2014 IEEE Conference on* , vol., no., pp. 1-3, 16-19 Nov. 2014.

[*Bevacqua et al.*, 2015a] M. Bevacqua, L. Crocco, L. Di Donato, T. Isernia, The virtual experiments: An emerging framework for the effective solution of inverse scattering problems, in *Antennas and Propagation (EuCAP), 9th European Conference on*, vol., no., pp.1-4, 13-17 April 2015.

[*Bevacqua et al.*, 2015b] M. Bevacqua, L. Crocco, L. Di Donato, T. Isernia, A 'virtual experiments' framework for inverse scattering, in *Radio Science Conference (URSI AT-RASC), 1st URSI Atlantic*, vol., no., pp. 1-1, 16-24 May 2015.

[*Bevacqua et al.*, 2015c] M. Bevacqua, L. Crocco, L. Di Donato, T. Isernia, R. Palmeri, Exploiting virtual experiments for the solution of inverse scattering problem, in *Electromagnetics in Advanced Applications (ICEAA), 2015 International Conference on* , vol., no., pp. 836-838, 7-11 Sept. 2015.

[*Bevacqua et al.*, 2015d] M. Bevacqua, L. Crocco, L. Di Donato, T. Isernia, Virtual Experiments for the Solution of Inverse Scattering Problems, *Progress In Electromagnetics Research Symposium (PIERS), Session 1P3 Focus Session. SC5: Imaging, Inverse Scattering and Remote Sensing 2,* vol., no., pp 305, 6-9 July 2015.

[*Bevacqua et al.*, 2015e] M. Bevacqua, L. Crocco, L. Di Donato, T. Isernia, Exploiting compressive sensing for non-linear inverse scattering, in *Radio Science Conference (URSI AT-RASC), 1st URSI Atlantic*, vol., no., pp. 1-1, 16-24 May 2015.

[*Bevacqua et al.*, 2015f] M. Bevacqua, L. Crocco, L. Di Donato, T. Isernia, Exploiting a Sparsity Enhanced Microwave Imaging Approach for Non-Destructive Evaluation, *Progress In Electromagnetics Research Symposium (PIERS), Session 3A10 SC5: Inverse Scattering Methods and Applications for NDE,* vol., no., pp 1382, 6-9 July 2015.

[*Bevacqua et al.*, 2015g] M. Bevacqua, L. Crocco, L. Di Donato, T. Isernia, An algebraic solution method for nonlinear inverse scattering, *IEEE Trans. Antennas Propag*, vol. 63, no. 2, pp. 601-610, Feb. 2015.

[*Bevacqua et al.*, 2015h] M. Bevacqua, L. Crocco, L. Di Donato, T. Isernia, Microwave imaging of non-weak targets via compressive sensing and virtual experiments, *IEEE Antennas and Wireless Propagat. Lett*, vol. 14, pp. 1035-1038, 2015.

[*Bevacqua and Scapaticci*, 2015] M. Bevacqua, and R. Scapaticci, Magnetic nanoparticles enhanced breast cancer microwave imaging via compressive sensing, in *Antennas and Propagation (EuCAP), 9th European Conference on* , vol., no., pp. 1-4, 13-17 April 2015.

[*Bevacqua and Di Donato*, 2015] M. Bevacqua, and L. Di Donato, Improved TV-CS approaches for inverse scattering problem, *on The Scientific World Journal, Hindawi*, 2015.

[*Bevacqua et al.*, 2016a] M. Bevacqua, R. Palmeri, L. Di Donato, L. Crocco, T. Isernia, Microwave Imaging via Iterated Virtual Experiments, in *Antennas and Propagation (EuCAP), 10th European Conference on,* vol., no., pp.1-5, 10-15 April 2016.

[*Bevacqua et al.*, 2016b] M. Bevacqua, L. Crocco, L. Di Donato, T. Isernia, R. Palmeri, Exploiting field conditioning and sparsity for microwave imaging of non-weak buried targets, *Radio Science* (in print).

[*Bevacqua and Scapaticci*, 2016] M. Bevacqua, and R. Scapaticci, A compressive sensing approach for 3D breast cancer microwave imaging with magnetic nanoparticles as contrast agent, *IEEE Trans. on Medical Imaging*, vol. 35, no. 2, pp. 665-673, Feb. 2016.

[*Boufounos et al.*, 2007] P. Boufounos, M. F. Duarte, and R. G. Baraniuk, Sparse signal reconstruction from noisy compressive measurements using cross validation, *IEEE 14th Workshop on Statistical Signal Processing,* 2007.

[*Bourqui et al.*, 2012] J. Bourqui, J. M. Sill, and E. C. Fear, A prototype system for measuring microwave frequency reflections from the breast, *Int. J. Biomed. Imag.*, vol. 12, pp. 1-12, 2012.

[*Bradford*, 2008] J. H Bradford, Measuring water content heterogeneity using multifold GPR with reflection tomography, *Vadose Zone J.*, vol. 7, pp. 184–193, 2008.

[*Brancaccio et al.*, 1995] A. Brancaccio, V. Pascazio, and R. Pierri, A quadratic model for inverse profiling: the one dimensional case, *J. Electromagn. Waves Appl.*, vol. 9, pp. 673-696, 1995.

[*Brignone et al.*, 2007] M. Brignone, J. Coyle, and M. Piana, The use of the linear sampling method for obtaining super-resolution effects in Born approximation, *J. Comput. Appl. Math.*, vol. 203, pp. 145-158, 2007.

[*Bucci and Franceschetti*, 1989] Bucci,O .M., and G. Franceschetti, On the degrees of freedom of scattered fields, *IEEE Trans. Antennas Propag.*, vol. 37, no. 7, pp. 918-926, 1989.

[*Bucci and Isernia*, 1997] O. M. Bucci, and T. Isernia, Electromagnetic inverse scattering: retrievable information and measurement strategies, *Radio Sci.*, vol. 32, pp. 2123-2138, 1997.

[*Bucci et al.*, 2000] O. M. Bucci, L. Crocco, T. Isernia, V. Pascazio, Inverse scattering problems with multifrequency data: reconstruction capabilities and solution strategies, *IEEE Trans. Geoscience Rem. Sensing*, vol. 38, no. 4, pp. 1749-1756, July 2000.

[*Bucci et al.*, 2001a] O. M. Bucci, N. Cardace, L. Crocco, T. Isernia, Degree of nonlinearity and a new solution procedure in scalar two-dimensional inverse scattering problems, *J. Opt. Soc. Am. A*, vol. 18, no. 8, pp. 1832-1843, 2001.

[*Bucci et al.*, 2001b] O. M. Bucci, L. Crocco, T. Isernia, and V. Pascazio, Subsurface inverse scattering problems: quantifying, qualifying, and achieving the available information, *IEEE Trans. Geoscience Rem. Sensing*, vol. 39, no. 11, pp. 2527–2538, Nov 2001.

[*Bucci et al.*, 2005] O. M. Bucci, I. Catapano, L. Crocco, and T. Isernia. Synthesis of new variable dielectric profile antennas via inverse scattering techniques: a feasibility study. *IEEE Trans. Antennas Propag.*, vol. 53, no. 4, pp. 1287-1297, 2005.

[*Bucci et al.*, 2014a] O. M. Bucci, G. Bellizzi, I. Catapano, L. Crocco, and R. Scapaticci, Corrections to "MNP Enhanced Microwave Breast Cancer Imaging: Measurement Constraints and Achievable Performances" [2012, pp. 1630- 1633], *IEEE Antennas and Wireless Propagat. Lett*, vol. 13, pp. 1818-1818, 2014.

[*Bucci et al.*, 2014b] O. M. Bucci, G. Bellizzi, L. Crocco, R. Scapaticci, G. Di Massa, S. Costanzo, A. Borgia, Magnetic Nanoparticle Enhanced Microwave Imaging: Towards an Experimental Feasibility Assessment, *Antennas and Propagation (EuCAP), 8th European Conference on*, pp. 696-698, The Hague, Holland, April 2014.

[*Cakoni and Colton*, 2006] F. Cakoni and D. Colton. Qualitative methods in inverse scattering theory, *Springer-Verlag*, Berlin, Germany, 2006.

[*Candès et al.*, 2006] E. J. Candès, J. K. Romberg, and T. Tao, Robust uncertainty principles: exact signal reconstruction from highly incomplete frequency information, *IEEE Trans. Inf. Theory*, vol. 52, n. 2, pp. 489-509, 2006.

[*Candès et al.*, 2008] E. J. Candès, M. Wakin, and S. Boyd, Enhancing sparsity by reweighted l_1 minimization, *J. Fourier Anal. Appl.*, 2008.

[*Candès et al.*, 2011] E. J Candes., Y. C Eldar, D. Needell, and P. Randall, Compressed sensing with coherent and redundant dictionaries, *Applied and Computational Harmonic Analysis*, vol. 31, no. 1, pp. 59-73, 2011.

[*Cardano*, 1545] G. Cardano, *Artis magnae sivede regulis algebraicis, liber unus,* 1545 (translated in *ArsMagna or the Rules of Algebra,* New York, NY, USA: Dover, 1993).

[*Catapano et al.*, 2004] I. Catapano, L. Crocco, and T. Isernia, A simple two-dimensional inversion technique for imaging homogeneous targets in stratified media. *Radio Science*, vol 39, no. 1, 2004.

[*Catapano et al.* 2007a] I. Catapano, L. Crocco, M. D'Urso, T. Isernia, On the Effect of Support Estimation and of a New Model in 2-D Inverse Scattering Problems, *IEEE Trans. Antennas Propag.*, vol. 55, no. 6, pp.1895-1899, June 2007.

[*Catapano et al.*, 2007b] I. Catapano, L. Crocco, and T. Isernia, On simple methods for shape reconstruction of unknown scatterers, *IEEE Trans. Antennas Propag.*, vol. 55, no. 5, pp. 1431-1436, 2007.

[*Catapano et al.*, 2009a] I. Catapano, L. Di Donato, L. Crocco, O. M. Bucci, A. F. Morabito, T. Isernia, and R. Massa, On quantitative microwave tomography of female breast, *Prog. Electromagn. Res.*, vol. 97, pp. 75–93, 2009.

[*Catapano et al.*, 2009b] I. Catapano, L. Crocco, M. D' Urso, and T. Isernia, 3D microwave imaging via preliminary support reconstruction: testing on the Fresnel 2008 database, *Inverse Probl.*, vol. 25, no. 2, pp. 1–23, 2009.

[*Catapano and Crocco*, 2009] I. Catapano and L. Crocco, An imaging method for concealed targets, *IEEE Trans. Geosci. Remote Sens.*, vol. 47, no. 5, pp. 1301–1309, 2009.

[*Chang et al.*, 2000] S. G. Chang, Y. Bin, and M. Vetterli, Adaptive wavelet thresholding for image denoising and compression, *IEEE Trans. Image Process.* ,vol.9, no. 9, pp. 1532–1546, Sep. 2000.

[*Chen.*, 2010] X Chen., Subspace-Based Optimization Method for Solving Inverse-Scattering Problems, *IEEE Trans. Geosci. Remote Sens.*, vol. 48, no. 1, pp. 42-49, Jan. 2010.

[*Chen et al.*, 2010] Y. Chen, I. J. Craddock, and P. Kosmas, Feasibility study of lesion classification via contrast-agent-aided UWB breast imaging, *IEEE Trans. Biomed. Eng.*, vol. 57, no. 5, pp. 1003-1007, May 2010.

[*Chew and Wang.*, 1990] W. C. Chew and Y. M. Wang, Reconstruction of two-dimensional permittivity distribution using the distorted Born iterative method, *IEEE Trans. Med. Imaging*, vol. 9, no. 2, pp. 218–225, 1990.

[*Chew*, 1995] W. C Chew, Waves and fields in inhomogeneous media, *The Institute of Electrical and Electronics Engineers, Inc.*, 1995.

[*Chiappinelli et al.*, 1999] P. Chiappinelli, L. Crocco, T. Isernia, V. Pascazio, Multiresolution techniques in microwave tomography and subsurface sensing, *Geoscience and Remote Sensing Symposium, IEEE IGARSS*, vol. 5, no., pp. 2516-2518, 1999.

[*Colton and Paivarinta*, 1992] D. Colton, and L. Paivarinta, The uniqueness of a solution to an inverse scattering problem for electromagnetic waves, *Arch. Ration, Mech. Anal.*, vol. 119, pp. 59-70, 1992.

[*Colton and Kress*, 1998] D. Colton, and R. Kress, Inverse Acoustic and Electromagnetic Scattering Theory*, Springer-Verlag, Berlin, Germany*, 1998.

[*Colton et al.*, 2003] D. Colton, H. Haddar, and M. Piana, The linear sampling method in inverse electromagnetic scattering theory. *Inverse Probl.*, vol. 19, pp. 105–137, 2003.

[*Crocco and Isernia*, 2001] L. Crocco, and T. Isernia, Inverse scattering with real data: detecting and imaging homogeneous dielectric objects. *Inverse Probl.*, vol. 17, no. 6, pp. 1573 - 1583, 2001.

[*Crocco and Soldovieri*, 2003] L. Crocco, and F. Soldovieri, GPR prospecting in a layered medium via microwave tomography, *Annals of Geophysics*, vol. 46, no. 3, pp. 559–572, Jun 2003.

[*Crocco et al.*, 2005] L. Crocco, M. D'Urso, and T. Isernia, Testing the contrast source extended Born inversion method against real data: the TM case, *Inverse Probl.*, vol. 21, pp. S33 -S50, 2005.

[*Crocco and Soldovieri*, 2011] L. Crocco, and F. Soldovieri, Nonlinear inversion algorithms, *in Subsurface Sensing, A. S. Turk, K. A. Hocaoglu, A. A. Vertiy,* John Wiley and Sons, NY, 2011.

[*Crocco et al.*, 2011] L. Crocco, I. Catapano, M. Bevacqua, L. Di Donato, T. Isernia, The Linear Sampling Method as a focusing strategy: available implicit information and hybrid inversion approaches, *In Proc. of the of PIER Symposium*, *Session 1P4a Theoretical Issues and Experimental Constraints in Active Microwave Imaging,* 20-23 March 2011.

[*Crocco et al.*, 2012a] L. Crocco, I. Catapano, L. Di Donato, and T. Isernia, The linear sampling method as a way for quantitative inverse scattering, *IEEE Trans. Antennas Propag.*, vol. 4, no. 60, pp. 1844–1853, 2012.

[*Crocco et al.*, 2012b] L. Crocco, L. Di Donato, D. A. M. Iero, and T. Isernia, An adaptive method to focusing in unknown scenario, *Progress in Electromagnetic Research*, vol. 130, pp. 563-579, 2012.

[*Crocco et al.*, 2012c] L. Crocco, L. Di Donato, D. A. M. Iero, T. Isernia, A New Strategy for Constrained Focusing in Unknown Scenarios, *IEEE Antenn. and Wirel. Pr.*, vol. 11, pp. 1450-1453, 2012.

[*Crocco et al.*, 2013] L. Crocco, L. Di Donato, I. Catapano, T. Isernia, An Improved Simple Method for Imaging the Shape of Complex Targets, *IEEE Trans. Antennas Propag*, vol. 61, n. 2, pp. 843-851, 2013.

[*Cui et al.*, 2001] T. J. Cui, W. C. Chew, A. A. Aydiner, and S. Chen, Inverse scattering of two-dimensional dielectric objects buried in a lossy earth using the distorted Born iterative method, *IEEE Trans. Geosci. Remote Sens.*, vol. 39, no. 2, pp. 339–346, 2001.

[*Daniels*, 2004] D. J. Daniels, Ground Penetrating Radar, 2-nd edition, *London, UK, The Institution of Electrical Engineers*, 2004.

[*Daniels*, 2006] D. J. Daniels., A review of GPR for landmine detection, *Sensing and Imaging: An International Journal*, vol. 7, no. 3, pp. 90-123, 2006.

[*De Rosny et al.*, 2010] J. De Rosny, G. Lerosey, and M. Fink, Theory of electromagnetic time-reversal mirrors, *IEEE Trans. Antennas Propag.*, vol. 58, no. 10, pp. 3139-3149, 2010.

[*Desmal and Bagci*, 2014] A. Desmal, and H. Bagci, Shrinkage-Thresholding Enhanced Born Iterative Method for Solving 2D Inverse Electromagnetic Scattering Problem, *IEEE Trans. Antennas Propag*, vol. 62, no. 7, pp. 3878-3884, 2014.

[*Devaney and Wolf,* 1973] A. J. Devaney, and E. Wolf, Radiating and Non radiating Classical Current Distributions and the Fields They Generate, *Phys. Rev. D*, vol. 8, no. 4, pp. 1044-1047, 1973.

[*Devaney*, 1981] A. J. Devaney, Inverse-scattering theory within the Rytov approximation, *Optics letters,* vol. 6, no. 8, pp. 374-376, 1981.

[*Devaney and Oristaglio,* 1983] A.J. Devaney, and M. L. Oristaglio, Inversion procedure for inverse scattering within the distorted-wave Born approximation, *Phys. Rev. Lett*, vol. 51, pp. 237-240, Jul 1983.

[*Devaney*, 1984] A. J. Devaney, Geophysical diffraction tomography, *IEEE Trans. Geosci. Remote Sensing,* vol. GE-22, no. 1, pp. 3-13, Jan. 1984.

[*Devaney et al.*, 2005] A.J. Devaney, E.A. Marengo and F.K. Gruber, Time-reversal-based imaging and inverse scattering of multiply scattering point targets, *J. Acoust. Soc. Am.*, vol. 118, pp. 3129-3138, 2005.

[*Di Bari and Vetro*, 1998] Di Bari C., P. Vetro, Analisi matematica, teoria ed esercizi, vol. II, 1998.

[*Di Donato et al.*, 2011] L. Di Donato, M. Bevacqua, T. Isernia, I. Catapano, L. Crocco, Improved quantitative microwave tomography by exploiting the physical meaning of the Linear Sampling Method, *Antennas and Propagation (EUCAP), Proceedings of the 5th European Conference on* , vol., no., pp. 3828-3831, 11-15 April 2011.

[*Di Donato,* 2013] L. Di Donato, New paradigms and simple methods for Inverse scattering problems, *PhD Thesis*, Universitμa Mediterranea of Rggio Calabria, ISBN: 978-88-89367-70-4, 2013.

[*Di Donato et al.*, 2014a] L. Di Donato, L. Crocco, M. Bevacqua, T. Isernia, Quasi-Invisibility via inverse scattering techniques, in *Antenna Measurements and Applications (CAMA), 2014 IEEE Conference on*, vol., no., pp. 1-2, 16-19 Nov. 2014.

[*Di Donato et al.*, 2014b] L. Di Donato, M. Bevacqua, L. Crocco, T. Isernia, Exploiting compressive sensing in microwave tomography and inverse scattering, *Antennas and Propagation (EuCAP), 8th European Conference on*, vol., no., pp. 1247-1249, 6-11 April 2014.

[*Di Donato et al.,* 2015a] L. Di Donato, R. Palmeri, G. Sorbello, T. Isernia, and L. Crocco, Assessing the capabilities of a new linear inversion method for quantitative microwave imaging, *International Journal of Antennas and Propagation*, 2015.

[*Di Donato et al.*, 2015b] L. Di Donato, M. Bevacqua, L. Crocco, T. Isernia, Inverse scattering via virtual experiments and contrast source regularization, *IEEE Trans. Antennas Propag,* vol. 63, no. 4, pp. 1669-1677, April 2015.

[*Di Donato and Crocco*, 2015] L. Di Donato, and L. Crocco, Model based quantitative cross-borehole GPR imaging via virtual experiments, *IEEE Trans. Geosci. Remote Sens.*, vol. 53, no. 8, pp. 4178–4185, Aug 2015.

[*Di Donato et al.,* 2016] L. Di Donato, R. Palmeri, G. Sorbello, T. Isernia, and L. Crocco, A new linear distorted wave inversion method fot microwave imaging via virtual experiments, *Microwave Theory and Techniques* (submitted).

[*Donoho*, 2006] D. Donoho, Compressed sensing, *IEEE Trans. Inf. Theory*, vol. 52, no. 4, pp. 1289–1306, 2006.

[*Donelli et al.*, 2006] M. Donelli, G. Franceschini, A. Martini, and A. Massa, An integrated multiscaling strategy based on a particle swarm algorithm for inverse scattering problems, *IEEE Trans. Geosci. Remote Sens* , vol. 44, no. 2, pp. 298-312, Feb. 2006.

[*D'Urso et al.*, 2010] M. D'Urso, T. Isernia, and A. Morabito, On the solution of 2-d inverse scattering problems via source-type integral equations, *IEEE Trans. Geosci. Remote Sens.*, vol. 48, no. 3, pp. 1186–1198, 2010.

[*Fear et al.*, 2002] E. Fear, S. Hagness, P. Meaney, M. Okoniewski, and M. Stuchly, Enhancing breast tumor detection with near-field imaging, *IEEE Microwave Magazine*, vol. 3, pp. 48-56, Mar 2002.

[*Fink and Prada*, 2001] M. Fink, and C. Prada, Acoustic time-reversal mirrors, *Inverse Probl.*, vol. 17, no. 1, pp. R1–R38, 2001.

[*Francese et al.*, 2009] R. Francese, E. Finzi, and G. Morelli, 3D high-resolution multi-channel radar investigation of a roman village in northern italy, *Journal of Applied Geophysics*, vol. 67, no. 1, pp. 44 – 51, 2009.

[*Gerhards et al.*, 2008] H. Gerhards, U. Wollschlager, Q. Yu, P. Schiwek, X. Pan, and K. Roth, Continuous and simultaneous measurement of reflector depth and average soil-water content with multichannel ground penetrating radar, *Geophysics*, vol. 73, pp. J15 – J23, 2008.

[*Gilmore et al.*, 2009] C. Gilmore, P. Mojabi, and J. LoVetri, Comparison of an enhanced distorted born iterative method and the multiplicative-regularized contrast source inversion method, *IEEE Trans. Antennas Propag.*, vol. 57, no. 8, pp. 2341–2351, 2009.

[*Gubin et al.*, 1967] L. G. Gubin, B. T. Polyak, E. V. Raik, The method of projections for finding the common point of convex sets, *USSR Comput. Math. and Math. Phys.*, vol. 7, no. 6, pp. 1-24, 1967.

[*Gurbuz et al.*, 2009] A. C. Gurbuz, J. H. McClellan, and W. R. Scott, Compressive sensing for subsurface imaging using ground penetrating radar, *Signal Process.*, vol. 89, no. 10, pp. 1959-1972, Oct. 2009.

[*Habashy et al.*, 1993] T. M. Habashy, R. V. Groom, and B. R. Spies, Beyond the Born and Rytov approximations: a non linear approach to electromagnetic scattering, *J. Geophys. Res.*, vol. 98, no. B2, pp. 1759–1775, 1993.

[*Haddadin and Ebbini*, 1998] O. S. Haddadin and E. S. Ebbini, Imaging Strongly scattering media using a multiple frequency distorted Born Iterative method, *IEEE Trans. Ultrason. Ferroelect. Freq. Contr.*, vol. 45, pp. 1485-1496, Nov. 1998.

[*Hakansson*, 2007] A. Hakansson, Cloaking of objects from electromagnetic fields by inverse design of scattering optical elements, *Opt. Express*, vol. 15, no. 7, pp. 4328-4334, 2007.

[*Hansen*, 1990] P. C. Hansen, The discrete picard condition for discrete ill-posed problems, *BIT*, vol. 30, pp. 658–672, 1990.

[*Hansen and O'Leary*, 1993] P. C. Hansen, and D. P. O'Leary, The use of L-curve in the regularization of discrete ill-posed problem, *SIAM J. Sci. Comput.*, vol. 14, no. 6, pp. 1487–1503, Nov. 1993.

[*Hassan and El-Shenawee*, 2011] A. M. Hassan, and M. El-Shenawee. Review of electromagnetic techniques for breast cancer detection. *IEEE Reviews in Biomedical Engineering*, vol. 4, pp. 103-118, 2011.

[*Haupt*, 1995] R. L. Haupt, An introduction to genetic algorithms for electromagnetics, *IEEE Antennas Propag. Mag.*, vol. 37, no. 2, pp. 7-15, 1995.

[*Helbig et al.*, 2014] M. Helbig, J. Sachs, F. Tansi, and I. Hilger, Experimental feasibility study of contrast agent enhanced UWB breast imaging by means of M-sequence sensor systems, *Proc. 8th Eur. Conf. Antennas Propag*, pp. 311-315, 6-11 April 2014.

[*Hopcraft and Smith*, 1992] K. I. Hopcraft, and P. R. Smith, An Introduction to Electromagnetic Inverse Scattering, *Kluwer Academic Pubblishers*, 1992.

[*Isernia et al.*, 1997] T. Isernia, V. Pascazio, and R. Pierri, A nonlinear estimation method in tomographic imaging, *IEEE Trans. Geosci. Remote Sens.*, vol. 35, no. 4, pp. 910–923, 1997.

[*Isernia et al.,* 2000] T. Isernia, P. Di Iorio, and F. Soldovieri, An effective approach for the optimal focusing of array fields subject to arbitrary upper bounds, *IEEE Trans. Antennas Propag.*, vol. 48, no. 12, pp. 1837-1847.

[*Isernia et al.,* 2001] T. Isernia, V. Pascazio, and R. Pierri, On the local minima in a tomographic imaging technique, *IEEE Trans. Geosci. Remote Sens.*, vol. 39, pp. 1596–1607, 2001.

[*Isernia et al.*, 2004] T. Isernia, L. Crocco, and M. D' Urso, New tools and series for forward and inverse scattering problems in lossy media, *IEEE Trans. Geosci. Remote Sens. Lett.*, vol. 1, no. 4, pp. 327–331, 2004.

[*Jin and Yarovoy*, 2015] T. Jin, and A. Yarovoy, A Through-the-Wall Radar Imaging Method Based on a Realistic Model, *International Journal of Antennas and Propagation*, 2015.

[*Joachimowicz et al.,* 1998] N. Joachimowicz, J. J. Mallorqui, J. C. Bolomey, and A. Broquetas, Convergence and stability assessment of Newton Kantorovich reconstruction algorithms for microwave tomography, *IEEE Trans. Med. Imag.*, vol. 17, no 4, pp. 562-569, 1998.

[*Jones*, 1986] D. S. Jones, Acoustic and Electromagnetic Waves, *Oxford, England, Clarendon Press*, 1986.

[*Josephson et al.*, 1999] L. Josephson, C. H. Tung, A. Moore, and R. Weissleder, High efficiency intracellular magnetic labeling with novel superparamagnetic-Tat peptide conjugates, *Bioconjug. Chem.*, vol. 10, pp. 186-191, 1999.

[*Kantorovich and Alkilov*, 1977] L. V. Kantorovich, and G. P. Alkilov. Functional Analysis. Nauka, Moskow, 1977.

[*Katscher et al.*, 2009] U. Katscher et al., Determination of electric conductivity and local SAR via B1 mapping, *IEEE Trans. Med. Imag.*, vol. 28, no. 9, pp. 1365-1374, 2009.

[*Kirsch*, 1998] A. Kirsch, Characterization of the shape of a scattering obstacle using the spectral data of the far field operator, *Inverse Probl.*, vol. 14, pp. 1489–1512, 1998.

[*Kirsch*, 1999] A. Kirsch., Factorization of the far-field operator for the inhomogeneous medium case and an application in inverse scattering theory, *Inverse Probl.*, vol. 15, no. 413-429, 1999.

[*Kleinman and van den Berg*, 1993] R. E. Kleinman, and P. M. van den Berg, An extended modified gradient technique for profile inversion, *J. Geophys. Res.*, vol. 28, no. 2, pp. 877–884, 1993.

[*Kolmogorov and Fomine*, 1973] A. Kolmogorov, and S .V. Fomine, Elements de la Theorie des Fonctions et de l'Analyse Fonctionelle, *Editions MIR, Moscow*, 1973.

[*Lazebnik et al.*, 2007] M. Lazebnik et al., A large-scale study of the ultra wideband microwave dielectric properties of normal, benign and malignant breast tissue obtained from cancer surgeries, *Phys. Med. Biol.*, vol. 52, pp. 6093-6115, 2007.

[*Lencrerot et al.*, 2009] R. Lencrerot, A. Litman, H. Tortel, and J.-M. Geffrin, Imposing Zernike representation for imaging two-dimensional targets, *Inverse Prob.*, vol. 25, no. 3, p. 21, 2009.

[*Leone and Soldovieri*, 2003] G. Leone, and F. Soldovieri, Analysis of the distorted Born approximation for subsurface reconstruction: truncation and uncertainties effects, *IEEE Trans. Geosci. Remote Sens.*, vol. 41, no. 1, pp. 66–74, Jan 2003.

[*Leuschner et al.*, 2006] C. Leuschner, C. Kumar, W. Hansel, W. Soboyejo, J. Zhou, and J. Hormes, LHRH-conjugated magnetic iron oxide nanoparticles for detection of breast cancer metastases, *Breast Cancer Res. Treatment*, vol. 99, pp. 163-176, 2006.

[*Li et al.,* 2013] M. Li, O. Semerci, and A. Abubakar, A contrast source inversion method in the wavelet domain, *Inverse Prob.*, vol. 29, no. 2, pp. 1–19, 2013.

[*Lustig et al.*, 2008] M. Lustig, D.L. Donoho, J.M. Santos, and J.M. Pauly, Compressed Sensing MRI, *IEEE Signal Process. Mag*, vol. 25, no. 2, pp. 72- 82, March 2008.

[*Ma et al.*, 2000] Jianglei Ma, Weng Cho Chew, Cai-Cheng Lu, Jiming Song, Image reconstruction from TE scattering data using equation of strong permittivity fluctuation, *IEEE Trans. Antennas Propag* , vol.48, no.6, pp. 860-867, Jun 2000.

[*Mallat*, 1989] S. G. Mallat, A theory for multiresolution signal decomposition: The wavelet representation, *IEEE Trans. Pattern Anal. Mach. Intell.* , vol. 11, no. 7, pp. 674–693, Jul. 1989.

[*Mallat*, 2008] S. G. Mallat, A Wavelet Tour of Signal Processing, 3rd ed, *New York, NY, USA, Academic*, 2008.

[*Marengo et al.*, 2000] E. A. Marengo, A. J. Devaney, R. W. Ziolkowsk, Inverse source problem and minimum-energy sources, *J. Opt. Soc. Am*, vol. 17, no. 1, pp. 34-45, 2000.

[*Marengo and Ziolkowski*, 2000] E. A. Marengo, and R. W. Ziolkowski, Nonradiating and minimum energy sources and their fields: Generalized source inversion theory and applications, *IEEE Trans. Antennas Propag.*, vol. 48, no. 6, pp. 1553-1562, 2000.

[*Mashal et al.*, 2010] A. Mashal, B. Sitharaman, X. Li, P. Avti, A. Sahakian, J. Booske, and S. Hagness, Toward carbon-nanotube-based theranostic agents for microwave detection and treatment of breast cancer: Enhanced dielectric and heating response of tissues-mimicking materials, *IEEE Trans. Biomed. Eng.*, vol. 57, no. 8, pp. 1831-1834, Aug. 2010.

[*Meaney et al.*, 2012] P. M. Meaney et al., Clinical microwave tomographic imaging of the calcaneus: a first-in-human case study of two subjects, in *Biomedical Engineering, IEEE Transactions on* , vol. 59, no. 12, pp.3304-3313, Dec. 2012.

[*Millot and Casadebaig*, 2015] P. Millot, and L. Casadebaig, Ultra wide X-band microwave imaging of concealed weapons and explosives using 3D-SAR technique, *International Journal of Antennas and Propagation*, 2015.

[*Nachman*, 1993] A. I. Nachman, Global uniqueness for a 2-D inverse boundary value problem, Preprint Ser. 19, *Dep. of Math., Univ. of Rochester, Rochester, N.Y.*, 1993.

[*Oliveri et al.*, 2012] G. Oliveri, L. Poli, P. Rocca, and A. Massa, Bayesian compressive optical imaging within the Rytov approximation, *Opt. Lett.*, vol. 37, no. 10, pp. 1760–1762, 2012.

[*Oliveri et al.*, 2014] G. Oliveri, N. Anselmi, A. Massa, Compressive sensing imaging of non-sparse 2D scatterers by a total-variation approach within the Born approximation, *IEEE Trans. Antennas Propag.*, vol. 62, no. 10, pp. 5157-5170, Oct. 2014.

[*Park et al.*, 2009] J.Park et al., Systematic surface engineering of magnetic nanoworms for in vivo tumor targeting, *Small*, vol. 5, no. 6, pp. 694-700, 2009.

[*Pastorino et al.*, 2000] M. Pastorino, A. Massa, and S. Caorsi, A microwave inverse scattering technique for image reconstruction based on a genetic algorithm, in *Instrumentation and Measurement, IEEE Transactions on*, vol. 49, no. 3, pp. 573-578, Jun 2000.

[*Pastorino*, 2004] M. Pastorino, Recent inversion procedures for microwave imaging in biomedical, subsurface detection and nondestructive evaluation, *Measurement—Special Issue Imaging Measurement Systems* , vol. 36, no. 3/4, pp. 257-269, 2004.

[*Pastorino*, 2010] M. Pastorino, Microwave Imaging, *Wiley Online Library*, 2010.

[*Persico*, 2014] R. Persico, Introduction to Ground Penetrating Radar: Inverse Scattering and Data Processing, *Wiley*, 2014.

[*Pierri et al.,* 2002] R. Pierri, F. Soldovieri, A. Liseno, and F. De Blasio, Dielectric profiles reconstruction via the quadratic approach in 2D geometry from multifrequency and multifrequency/multiview data, *IEEE Trans. Geosci. Remote Sens.*, vol. 40, no. 12, pp. 2709-2718, 2002.

[*Pierri et al.*, 2013] R. Pierri, J. Bolomey, Q. H. Liu, and F. Soldovieri, "Inverse Scattering and Microwave Tomography in Safety, Security, and Health," International Journal of Antennas and Propagation, vol. 2013, Article ID 589598, 2 pages, 2013.

[*Poli et al.*, 2012] L. Poli, G. Oliveri, and A. Massa, Microwave imaging within the first-order Born approximation by means of the contrast-field Bayesian compressive sensing, *IEEE Trans. Antennas Propag.*, vol. 60, no. 6, pp. 2865–2879, Jun. 2012.

[*Richmond*, 1965] J. Richmond, Scattering by a dielectric cylinder of arbitrary cross section shape, *IEEE Trans. Antennas Propag.*, vol. 13, no. 3, pp. 334-341, Mar. 1965.

[*Roger*, 1981] A. Roger, Newton-Kantorovitch algorithm applied to an electromagnetic inverse problem, *IEEE Trans. Antennas Propag* , vol. 29, no. 2, pp. 232-238, Mar 1981.

[*Roberts*, 1995] P. P. Roberts, Design of microwave filters by inverse scattering. *IEEE Trans. Microwave Theory Tech.*, vol. 43, no. 4, pp. 739-743, 1995.

[*Scapaticci et al.*, 2012a] R. Scapaticci, L. Di Donato, I. Catapano, and L. Crocco, A feasibility study on microwave imaging for brain stroke monitoring, *Prog. Electromagn. Res. B*, vol. 40, pp. 305-324, 2012.

[*Scapaticci et al.*, 2012b] R. Scapaticci, I. Catapano, and L. Crocco, Wavelet-Based Adaptive Multiresolution Inversion for Quantitative Microwave Imaging of Breast Tissues, *IEEE Trans. Antennas Propag*, vol. 60, no. 8, pp. 3717-3726, Aug. 2012.

[*Scapaticci et al.*, 2014] R. Scapaticci, G. Bellizzi, I. Catapano, L. Crocco, and O.M. Bucci, An effective procedure for MNP-enhanced breast cancer microwave imaging, *IEEE Trans. on Biomed. Eng.*, vol. 61, no. 4, pp. 1071-1079, 2014.

[*Scapaticci et al.*, 2015] R. Scapaticci, P. Kosmas, L. Crocco, Wavelet-based regularization for robust microwave imaging in medical applications, *IEEE Trans. on Biomed. Eng.*, vol. 62, no. 4, pp. 1195-1202, April 2015.

[*Selesnick and Bayram*, 2014] I. W. Selesnick, and I. Bayram, Sparse signal estimation by maximally sparse convex optimization, *IEEE Trans. Signal Processing*, vol. 62, no. 5, pp. 1078-1092, March1, 2014.

[*Selesnick et al.*, 2015] I. W. Selesnick, A. Parekh, and I. Bayram, Convex 1-D total variation denoising with non-convex regularization, *IEEE Signal Processing Letters,* vol. 22, no. 2, pp. 141-144, Feb. 2015.

[*Semenov et al.*, 2007] S. Semenov et al., Microwave tomography for functional imaging of extremity soft tissues: feasibility assessment. *Physics in Med. and Bio.*, vol. 52, no. 18, p. 5705, 2007.

[*Semenov and Corfield*, 2008] S. Y. Semenov, and D. R. Corfield, Microwave tomography for brain imaging: feasibility assessment for stroke detection, *International Journal of Antennas and Propagation*, no ID 254830, 2008.

[*Shea et al.*, 2010] J. Shea, P. Kosmas, B. V. Veen, and S. Hagness, Contrast enhanced microwave imaging of breast tumors: A computational study using 3D realistic numerical phantoms, *Inverse Probl.*, vol. 26, no. 7, pp. 1-22, 2010.

[*Soldovieri and Crocco*, 2011] F. Soldovieri, and L. Crocco, Electromagnetic tomography, in Subsurface Sensing, *A. S. Turk, K. A. Hocaoglu, A. A. Vertiy*, John Wiley and Sons, NY, 2011.

[*Soldovieri et al.,* 2007] F. Soldovieri, J. Hugenschmidt, R. Persico, and G. Leone, A linear inverse scattering algorithm for realistic GPR applications, *Near Surf. Geophys.*, vol. 5, no. 1, pp. 29-41, 2007.

[*Song and Shin*, 1985] G. H. Song, and S. Y. Shin, Design of corrugated waveguide filters by the Gel'fand-Levitan-Marchenko inverse scattering method, *J. Opt. Soc. Am. A*, vol. 2, no. 11, pp. 1905-1915, 1985.

[*Song et al.*, 2015] R. Song, X. Chen, K. Xu, Y. Zhong, and L. Ran, Multiplicative-regularized FFT twofold subspace-based optimization method for inverse scattering problems, *IEEE Trans. Geosci. Remote Sens.*, vol. 53, no. 2, pp. 841–850, 2015.

[*Souriau et al.*, 1996] L. Souriau, B. Duchene, D. Lesselier, and R. E. Kleinman, Modified gradient approach to inverse scattering for binary objects in stratified media, *Inv. Probl.*, vol. 12, pp. 463–481, 1996.

[*Tikhonov et al.*, 1995] A. N.Tikhonov, A. Goncharsky, V. Stepanov, and A. Yagola, Numerical Methods for the Solution of Ill-Posed Problems, *Kluwer, Dordrecht*, 1995.

[*Tibshirani*, 1996] R. Tibshirani, Regression shrinkage and selection via the lasso, *J. Roy.Stat. Soc. Ser.*, vol 58, no. 1, pp. 267-288, 1996.

[*Wang and Chew,* 1989] Y. M. Wang, and W. C. Chew, An iterative solution of two-dimensional electromagnetic inverse scattering problem, *Int. J. Syst. Technol*, vol. 1, no. 1, pp. 100-108. 1989.

[*Winters et al.*, 2009] D.W. Winters, J.D. Shea, P. Kosmas, B.D. Van Veen, and S. C. Hagness, Three-dimensional microwave breast imaging: dispersive dielectric properties estimation using patient-specific basis functions, *IEEE Trans. on Medical Imaging*, vol. 28, no. 7, pp. 969-981, 2009.

[*Xu K. et al.*, 2015] K. Xu, Y. Zhong, R. Song, X. Chen, L. Ran, Multiplicative regularized FFT twofold subspace-based optimization method for inverse scattering problems, *IEEE Trans. Geosci. Remote Sens*, vol. 53, no. 2, pp. 841-850, 2015.

[*Zastrow et al.*, 2008] E. Zastrow, S.K. Davis, M. Lazebnik, F. Kelcz, B.D. Van Veen, and S.C. Hagness, Development of anatomically realistic numerical breast phantoms with accurate dielectric properties for modeling microwave interactions with the human breast, *IEEE Trans. Biomed. Eng.*,vol. 55, no. 12, pp. 2792-2800, Dec. 2008.

[*Zhang et al.*, 2012a] X. Y. Zhang, H. Tortel, A. Litman, and J-M. Geffrin, An extended-DORT method and its application in a cavity configuration, *Inverse Probl.*, vol. 28, no. 11, 2012.

[*Zhang et al.*, 2012b] W. Zhang, M. G. Amin, F. Ahmad, A. Hoorfar, and G. E. Smith, Ultra wide band Impulse Radar Through-the-Wall Imaging with Compressive Sensing, *International Journal of Antennas and Propagation*, vol. 2012, 11 pages, 2012.

[*Zhong and Chen*, 2007] Y. Zhong, and X. Chen, Music imaging and electromagnetic inverse scattering of multiple-scattering small anisotropic spheres, *IEEE Trans. Antennas Propagat.*, vol. 55, no. 12, pp. 3542–3549, 2007.

[*Zhou et al.*, 2010] T. Zhou, P.M. Meaney, M.J. Pallone, S. Geimer, K.D. Paulsen, Microwave tomographic imaging for osteoporosis screening: a pilot clinical study, *Engineering in Medicine and Biology Society (EMBC), 2010 Annual International Conference of the IEEE* , vol., no., pp. 1218-1221, 2010.

[*Zoughi*, 2000] R. Zoughi, Microwave Nondestructive Testing and Evaluation, *Kluwer Academic Publishers, The Netherlands*, 2000.